From observations and measurements to realistic modeling of cometary nuclei

Von der Fakultät für Elektrotechnik, Informationstechnik, Physik
der Technischen Universität Carolo-Wilhelmina
zu Braunschweig
zur Erlangung des Grades eines
Doktors der Naturwissenschaften
(Dr.rer.nat.)
genehmigte
Dissertation

von Jean-Baptiste Vincent
aus Toulouse, France

Contents

Summary

Studying the surface of a comet is challenging because either the nucleus is too far to be resolved in details, or it is close enough but its own activity hides all the features we would like to investigate. One of the topic of interest is the localization of active regions on the surface. Although this can be done quite easily from a spacecraft, the jets of gas and dust represent also a hazard for any probe passing at close distance from the nucleus. Therefore any hint on the local activity should be taken into consideration to constrain the approach.

We believe that this can be achieved through the analysis of the so called dust coma structures. At first the dust coma of an active comet as seen in ground-based observations look rather homogeneous and featureless. However, after enhancing the images details through several image processing techniques, one can realize that the coma is not uniform and sometimes displays a great variety of structures shaped as fans, jets, circles, or spirals. These patterns are generally considered as indicators of the presence of active dust emitting regions at the surface of the rotating nucleus.

The goal of this PhD project was first to study and compare different image processing methods one can use in order to reveal the coma structures in the exposures, and then to develop a scientific software package that would allow determining a more realistic physical model of cometary nuclei from the same observations, obtained from Earth or from spacecraft platforms close to the comet. For this purpose, a flexible 3-dimensional model of the nucleus and a physical description of the dust acceleration processes in the nucleus neighborhood were developed. By using realistic shape assumptions for the nucleus we performed a forward modeling of the dust coma structures around the comet, emphasizing the retrieval of typical parameters at different scale: determination of the spin axis orientation of the nucleus, characterization of dust properties (grain size, initial velocity, sensitivity to the radiation pressure), and localization of the active regions at the surface of the nucleus.

This approach provided interesting results on several comets. Among them we determined first the spin axis orientation of various nuclei: 73P/Schwassmann-Wachmann 3 components B & C, and 9P/Tempel 1. We performed then a full analysis of the coma structures for 9P/Tempel 1. From there we were able to localize active regions and constrain the dust parameters as well as the activity profile, with excellent agreement between our results and in-situ measurements for all the parameters.

Such a modeling attempt including a realistic shape of the nucleus is a challenging "first" worldwide and we believe it has the prospect to path the way into a new era of modeling interpretation of comets that will be needed in the context of ESA's ROSETTA mission to comet 67P/Churyumov-Gerasimenko.

1 General introduction to comets

If everybody understands quite clearly the concepts of planets and stars, it is somehow different for comets. When asked about these objects most of the people, scientists included, give different descriptions. A majority refers to what specialists would call *active comets*, a bright object covering a large portion of the sky, whereas others describe a small, dark, and frozen body, lost at the borders of our Solar System. These two visions of the same object are both correct and understanding the link between them is the basis of cometary science. One can study comets from different points of view, considering them as frozen witnesses of the origin of planetary formation, as well as living laboratory for complex physics and chemistry. The work described in this thesis investigates a specific field of cometary research, but it will be easier to understand for the reader if we first summarize the main concepts of cometary science, from early observations to advanced theories.

1.1 Early observations

Comets have been observed from the early ages of humanity and the oldest descriptions which survived until now date back to the Mesopotamians of the Bronze Age and the book *"The Epic of Gilgamesh"*, one of the earliest literary writings (around 2500 BCE). In this tale, a comet is described as a falling star bringing disasters to Earth as it passes by.

Comets have been considered as bad omens by all civilizations until very recent time. As often in human history these objects were feared due to a lack of understanding of their nature. With respect to the other celestial bodies, comets display a completely different behavior. Unlike planets and stars, they show a rather changing appearance, and seem to come from random directions, therefore breaking the ancient belief that the sky, as the domain of gods, is organized with perfect rules and all events occurring there must be predictable. Thus around 340 BCE, the Greek philosopher Aristotle concluded that comets cannot belong to the *celestial spheres* and must be meteorological phenomena. At the same epoch, Chinese astronomers were also observing comets and compiling their results in catalogues where comets were associated with disasters that might have occurred at the same time (see Fig. 1.1). All these documents are still of a great value for modern astronomers, as they allow us to track back the appearance of some of the most famous comets. For example it is believed that the first observation of comet 1P/Halley has been reported in one of the Chinese observation logs.

Comets remained feared and misunderstood until the sixteenth century, when the Danish astronomer Tycho Brahe measured the parallax of the Great Comet of 1577 (modern designation: C/1577 V1). By comparing this value with the parallax of the Moon mea-
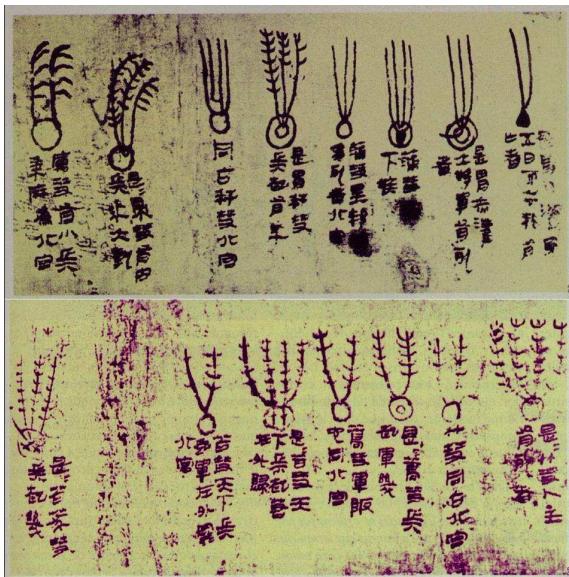
Figure 1.1: Mawangdui silk (China, 300 BCE), a catalogue of cometary observations along with the various disasters associated with them. It describes events going back to 1500 BCE. Source: NASA/JPL.

sured at the same time, he concluded that the distance of the comet was larger than the Earth-Moon distance. Therefore comets had to be celestial objects, and could be studied as any other cosmic bodies. This was the beginning of the understanding of the true nature of comets. In 1701 Sir Edmund Halley estimated from different observations that three observed comets might be the same object coming back to the inner Solar System every 76 years. He predicted the return of this comet in 1758. Sadly, Halley died in 1742, but his prediction was correct and started the age of modern cometary science.

1.2   Origin of comets

1.2.1   Orbits

If comets are not meteorological phenomena, where do they come from ? In other words, how to combine what we know of celestial mechanics and formation of the Solar System with this apparent randomness in the cometary orbits ?

In the absence of perturbations, comets follow a Keplerian orbit, i.e. they orbit on a path that is a conic section with the Sun at one focus. This kind of orbit can be fully parametrized by a set of values called orbital elements. They can be obtained from a few observations of a celestial body and describe completely its orbit. Appendix A summarizes the main equations needed for this calculation.

The 20th century saw a lot of measurements of cometary orbits and a classification started based on the orbital elements. Comets were divided in two main groups: short period and long period comets, with their parameters summarized in Table 1.2.1

Based on this classification it is noticed than generally comets with a period shorter than 200 years orbit mainly within 100 AU from the Sun and with a low inclination on the

	Short period	Long period
Period	< 200 years	> 200 years
a	< 100 AU	< 10^5 AU
i	< 30°	all values

Table 1.1: Main parameters for the classification of comets.

ecliptic whereas comets with a longer period can reach very far distances and approach the Sun more or less isotropically with a random inclination. Based on the total number of comets observed, the ratio between long period and short period comets is $\simeq 5 : 1$.

This classification can be refined by considering the Tisserand criterion which describes the changes of orbital elements of an object encountering a planet. For example if we consider the interaction with Jupiter, we can write the Tisserand parameter as:

$$T_J = \frac{a_J}{a} + 2 \cdot \sqrt{\frac{a}{a_J}(1 - e^2)} \cdot cos(i) = constant \tag{1.1}$$

whith a the semi-major axis of the comet orbit, a_J Jupiter's one, e and i the eccentricity and inclination of the comet orbit.

This parameter is conserved during the encounter, therefore we can establish groups of comets with similar Tisserand values as shown in figure 1.2
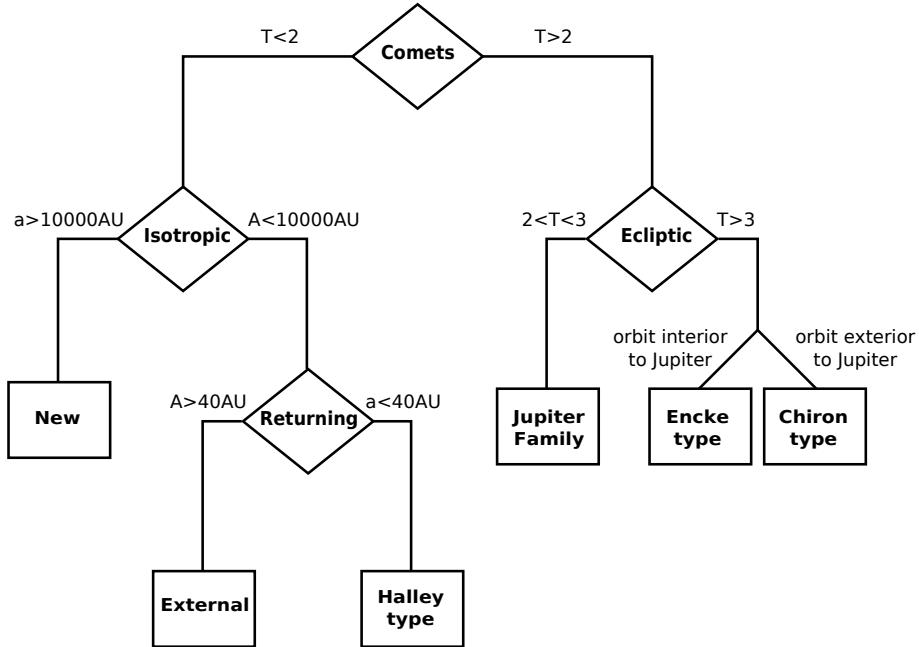
Figure 1.2: Cometary classification scheme based on Tisserand parameter. Adapted from Levison and Dones (2007)

1.2.2   Reservoirs

Until 1950, no theory was able to explain the existence of these different groups of comets, in particular the strong differences in inclination and semi-major axis for the short and

long period comets. However Oort (1950) showed that a plot of the number of comets versus the inverse of their semi-major axis gave a very strong peak around zero (Fig. 1.3). The observed dispersion in $1/a$ was much smaller than it was expected if comets would have been in the inner solar system several times, the gravitational interactions with the giant planets leading usually to a broadening of this dispersion. Hence all these comets must have entered the solar system for the first time when observed, and therefore the measured values of a and i indicate their original location. Oort finally concluded on the existence of spherical cloud orbiting the Sun at $\simeq$ 50 000 AU. It is interesting to notice that Oort did the whole study with a set of only 19 long-periods comets but his results are still valid now that we have much more statistics.
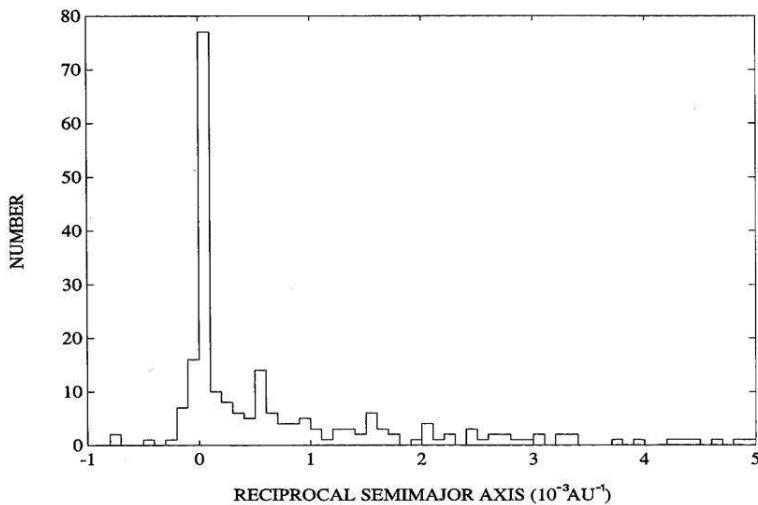
Figure 1.3: Distribution of $1/a$ shows a peak around 5.10^{-3}, typical of orbits which have not been affected by interactions with the giant planets. Adapted from Marsden et al. (1978).

Similar considerations led Kuiper (1951) to postulate that short period comets must come from a flattened disk orbiting between 30 and 55 AU, considered as a remnant of the accretion disk of planetesimals in the solar nebula. This reservoir is named after him the Kuiper belt. See Fig. 1.4 for a schematic representation.

1.2.3   Origins

We have seen that the Oort cloud and the Kuiper belt are satisfying theories to explain the observed orbits of the comets. However if the position of the Kuiper belt can be easily understood from models of the original accretion disk, it is more difficult to justify the origin of the Oort cloud. Several theories have been proposed, some of them are still debated. As it is not the subject of this thesis we will only introduce the most commonly accepted one: the Nice model (Gomes et al. (2005), Morbidelli (2005)). This theory suggests the following scenario (see also Fig. 1.5):

- We consider an original solar system much more compact than now, with the four giant planets orbiting between 5.45 and 14.2 AU, surrounded by a disk of planetesimals at 15-35 AU.
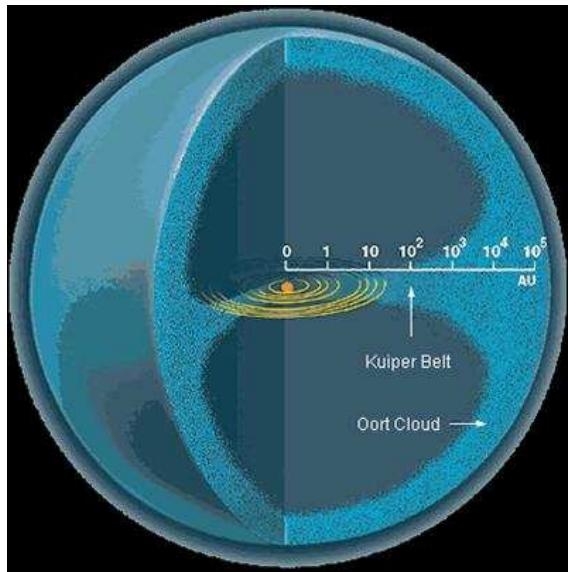
Figure 1.4: Schematic representation of the Kuiper belt and the Oort cloud with respect to the Solar System. Credit: Southwest Research Institute.

- Due to gravitational perturbations from the closest giant planets, planetesimals are dragged inwards. In order to conserve the angular momentum of the Solar System, Saturn, Uranus, and Neptune migrate slowly outwards.

- The situation is different for Jupiter. As its gravitational force is much stronger, most of the small bodies are accelerated and ejected out of the inner solar system, which causes Jupiter to move inwards to balance the loss of angular momentum.

- This slow migration goes on for ≃800 Myrs, until Jupiter and Saturn cross their 1:2 mean-motion resonance orbit. The gravitational interaction between the two bodies causes an increase in Saturn eccentricity, which affects the two other giant planets, eventually switching their orbits.

- In 4 Myrs, planets move from their original position to the current one. As Neptune moves closer to the planetesimals, 97% of the mass present in this region is ejected inwards (Late Heavy Bombardment), and outwards (Oort Cloud) the solar system.

This model is very interesting as it solves not only the problem of the origins of comets, but it fits also with observations showing a lack of mass in the Kuiper belt, or evidences of a late heavy bombardment at ≃800 Myrs after the formation of the Solar System (as seen from craters impact on the Moon and Mercury, see Fig. 1.6). However it relies on assumptions on the initial position of the planets that are difficult to verify. Nevertheless it is the best theory so far to justify the existence of cometary reservoirs.

1.2.4   Lifetime of comets

We have seen that most of the comets are observed while they enter the inner Solar System for the first time. Whatever is the process that placed the comets where they are now, the
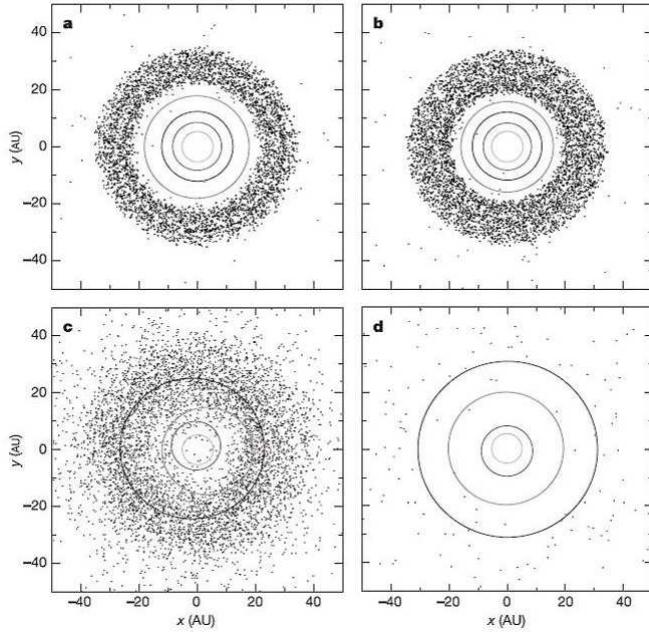
Figure 1.5: Numerical calculation for the Nice model. Planets are initially at orbits be-tween 5.45 and 14.2 AU. The disk of planetesimals is located between 15.5 and 34 AU. The four panels represent the orbital configuration at four different epochs. a) 100 Myr, beginning of planetary migration. b) 879 Myr, situation just before reaching reaching the 1:2 mean motion resonance (MMR) between Jupiter and Saturn. c) 882 Myr, situation just after reaching the 1:2 MMR. d) 1082 Myr, final state, only 3% of initial disk mass remains in the Kuiper belt. Source: Gomes et al. (2005)

.

important point to notice is that they stayed there almost since their formation, i.e. the early ages of the Solar System. As they approach the Sun, their surface sublimates (see section 1.3.1), abrading the nucleus. This process goes on until all the volatiles have disappeared, or until a disruptive event (outburst, tidal forces from giant planets, impact), achieves the complete destruction of the nucleus.

1.3   Nucleus, coma, tails, and trail

1.3.1   Nucleus

Comets were firstly known as very bright objects displaying a changing appearance with a main coma and several tails expanding up to hundred millions kilometers or more. How-ever, modern observations with large telescopes and spacecraft have shown that far from the Sun, comets look completely different. There, only their nucleus is visible, a dark and small object, with a diameter of only a few kilometers.

The fact that a small body can produce such extended structures might seem surprising but can be explained quite simply. According to the modern vision of comets, the nucleus is a discrete rotating body which consists mainly of water ice ($\simeq 80\%$), complex volatiles
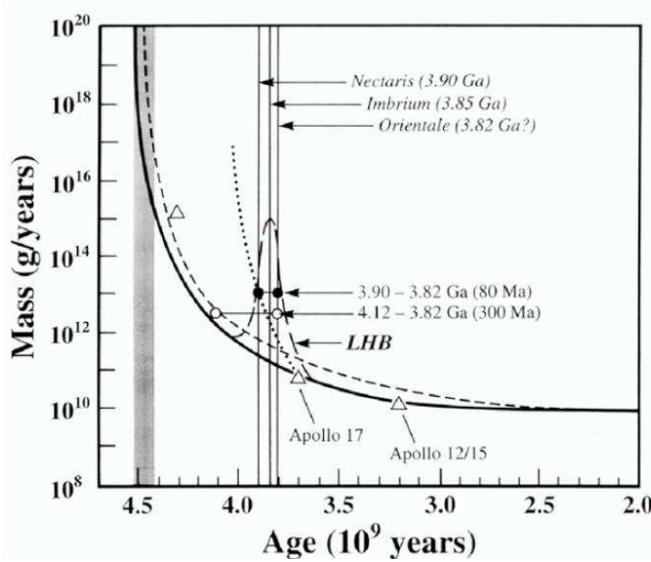
Figure 1.6: Plot of the amount of mass impacting the Moon versus the age of the Solar System. There is a clear indication for a huge bombardment around 4.1 Gyrs. Source Morbidelli (2005)

formed out of abundant elements (H, C, N and O), and dust (mostly Si). Far away from the Sun, the body is frozen and only the the nucleus is present. As the comet approaches the Sun, the solar heating increases the surface temperature, the ice sublimates producing gas which drags along dust, creating a coma of mixed material around the nucleus. Solar wind, gravitational forces, and radiation pressure expand the gas and dust in the vacuum giving rise to the tails.

The heliocentric distance at which sublimation starts gives valuable information as it depends on the composition of ices present at the nucleus surface. Figure 1.8 details the behavior of various ices. It is generally observed that the vaporization rate of water ice becomes negligible after 3 AU, therefore any activity observed at larger heliocentric distance must be driven by another material (for example CO ice) or another process such as the exothermal H_2O amorphous crystalline transition.

A question that is still puzzling scientist is to know how the ice is distributed at the surface of the nucleus, and more generally what is the structure of a cometary nucleus.

So far only six comets have been visited by a spacecraft, with images of the nucleus for four of them (Fig. 1.9). Observations revealed very dark objects, i.e. albedo lower than 3-4% for 1P/Halley (Keller et al. 2004), and about 5% for 9P/Tempel1 (Li et al. 2007)). Furthermore, their surface is covered with dust and the active regions where sublimation takes place represents only a portion of the whole area. This is quite representative of comets which have experienced already several perihelion passages. "Fresh" comets entering the inner Solar System for the first time are usually more active. Estimations of the bulk density revealed a very low value (for instance about $400 kg.m^{-3}$ for 9P/Tempel 1 according to Richardson et al. (2007)). This indicates that cometary nuclei are not made of solid rock but have a rather fluffy or rubble-pile structure with different materials loosely packed together. Thus the sublimation might not happen only at the surface but can also take place beneath as the heat wave penetrates into the nucleus, with the vaporized gas

15

Figure 1.7: The coma and tails of comet C/1995 O1 Hale-Bopp, April 1997
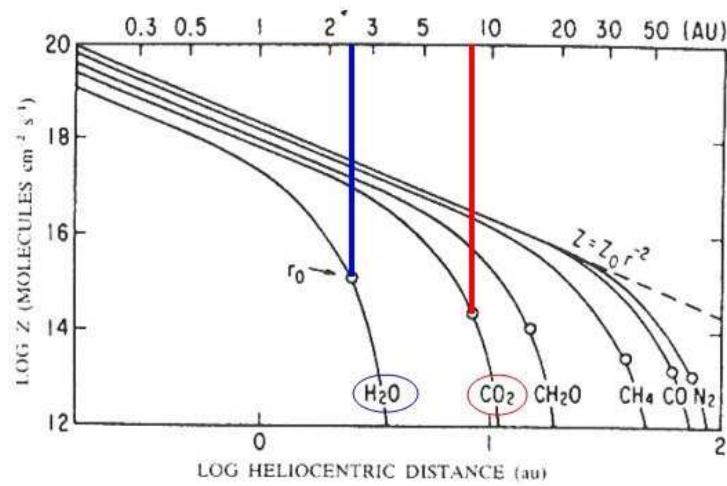
Figure 1.8: Chart displaying the sublimation rate of various ices with respect to the helio-centric distance. The dots labeled r_0 indicate the distance beyond which the sublimation becomes negligible. Source: Delsemme (1982).
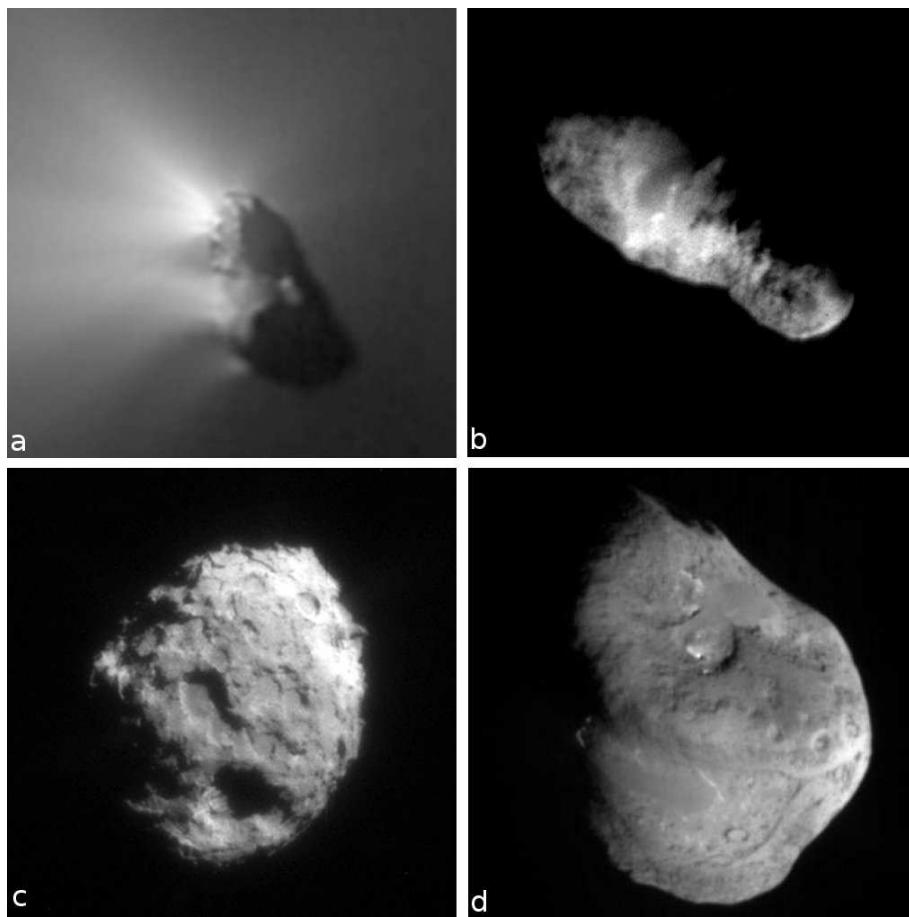
Figure 1.9: Close views of the four cometary nuclei imaged by spacecrafts: (a) 1P/Halley, mission Giotto, March 86; (b) 19P/Borelly, mission Deep Space 1, September 2001; (c) 81P/Wild 2, mission Stardust, January 2004; (d) 9P/Tempel 1, mission Deep Impact, July 2005.

carried outside through vents or holes in the structure.

1.3.2   Gas coma and ion tails

As the ice sublimates, the pressure difference forces the gas to expand around the nucleus, creating a coma. It is composed of neutral gas molecules and dust particles distributed in a more or less spherical volume centered on the nucleus, extending up to $10^6 km$. Parents molecules are broken and ionized by incident UV radiation and the ionized gas is accelerated away from the coma by the solar wind, giving rise to the ion or plasma tail which expand up to $10^8 km$ or more. The interaction between the solar wind and the coma is quite complex but it can be summarized as the following. The solar wind carries along the solar magnetic field. As a cometary nucleus is not magnetized, it is totally transparent for the solar wind. However the ionized coma presents a serious obstacle for the magnetic field and forces the magnetic field lines to bend over the coma in the anti-sunward direction (see Fig. 1.10). Ionized molecules are then accelerated along the magnetic field lines. It is interesting to notice that it is the observation of cometary ion tails which led Biermann

17
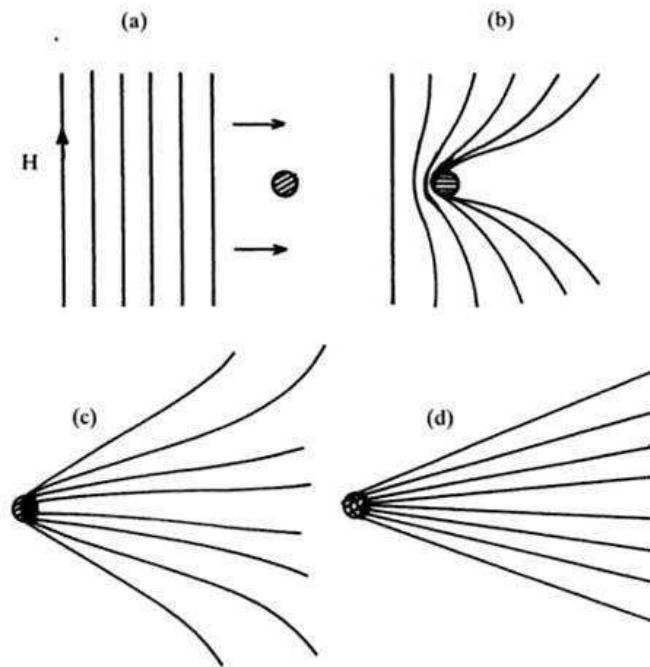
Figure 1.10: Representation of the distortion of the solar magnetic field lines by the ionized gas coma. The solar magnetic field cannot penetrate inside the ionized coma, leading to a bending of its field lines towards the anti solar direction. Adapted from Alfvèn (1957)

(1951) to postulate the existence of the solar wind, the basic theory of comet-solar wind interaction proposed by Alfvèn (1957) a few years later.

1.3.3   Dust coma, tail, and trail

The situation is different for the dust particles and will be described with more details in Chapter 3. The grains experience different forces which are mainly negligible, except for the solar gravity and radiation pressure. These two forces vary in a similar way, with the square of the heliocentric distance, but have an opposite direction. Therefore the dust grains feel a force acting like a reduced gravity field (sometimes even repulsive) and their trajectories are Keplerian orbits slowly drifting away from the original cometary orbit, creating a dust tail which can extend up to $10^7 km$ (see Fig.1.11 for an example).

Some of the particles are big(i.e. *mm*-sized or larger) such that they are hardly affected by the radiation pressure and therefore follow the comet on a very similar orbit, forming a *trail*. They are responsible for the meteor showers which occur when the orbit of the Earth crosses their path. It has also been observed for some comets a long and narrow dust structure called *neckline* (Kimura and Liu (1977), Fulle and Sedmak (1988)). For an observer close to the orbital plane of the comet, it appears as a thin linear structure slightly inclined on the projected orbit and is composed of large grains (but on average smaller than in the trail) emitted in an ellipsoidal shell at 180°of true anomaly in the orbital plane of the dust grain before the observation, and collapsing again in the orbital plane. Particles in the neckline are younger than in the trail where one can find dust grains from previous orbits.
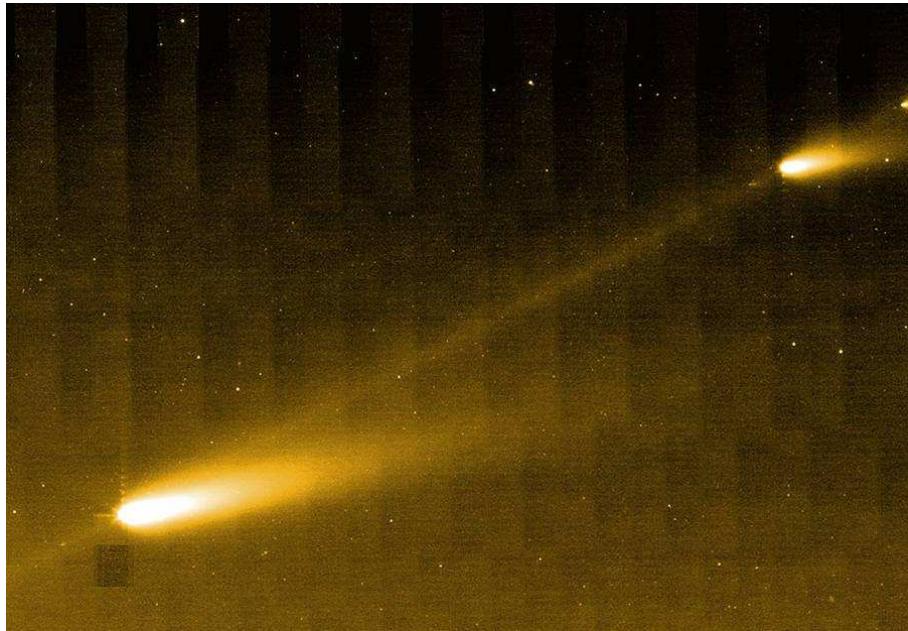
Figure 1.11: Dust tails and trail of the fragments of comet Schwassmann-Wachmann 3 in 2006. The trail appears as a thin line along the orbit of the fragments while the dust tails are bended towards the anti-sunward direction. Notice that the ion tail is not visible in this image due to the filters used. Source: NASA/JPL-Caltech/W. Reach (SSC/Caltech)

1.3.4   Neutral gas tail

Ion and dust tails are the most common tails observed in comets and are often referred to as type I and type II tails. In the last decade it has been observed what could be a new type of tail. While observing comet Hale-Bopp (C/1995 O1), Cremonese et al. (1997) reported a long and narrow gas tail dominated by sodium. Other observers (Wilson et al. 1998) reported also the presence of a second sodium tail, more diffuse than the one observed by Cremonese et al. As the morphology of this diffuse tail is consistent with the dust one, Wilson et al. (1998) proposed dust grains as the source for the sodium through evaporation. A sodium tail as also been observed in comet Hyakutake (C/1996 B2) (Mendillo et al. 1998) and it is now assumed that it could be a common feature of comets (Cremonese et al. 2002).

1.4   Dust coma structures

If tails and trails are the most obvious features of an active comet, visible even by naked eyes, they are not the only ones. The work of this PhD thesis focuses on a different kind of dust structures, embedded in the coma.

High resolution images of the inner coma, show structures of various kinds (Fig. 1.12). Theses features are believed to be the signatures of active dust-emitting regions at the surface of a rotating nucleus (Sekanina (1987), see figures 1.13 & 1.14 for schematics of the structures formation). When released, the particles are dragged into the vacuum by the gas flows and have their trajectories affected by the solar gravity and radiation pressure.
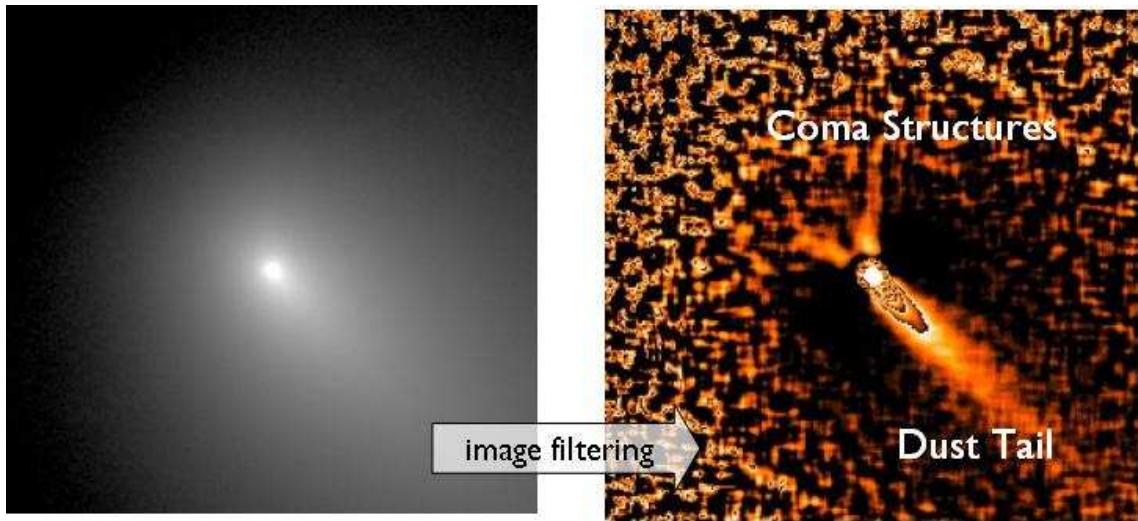
Figure 1.12: Illustration of coma structures (right panel) revealed in an image of the coma of comet 73P/Schwassmann-Wachmann 3-C (left panel) through image processing techniques (see chapter 2 for details).

Depending on their original size, velocity, or composition, dust grains will have a different reaction to these forces and with respect to the Sun they will follow different Keplerian orbits as they move away from the nucleus. However because of the viewing geometry and the projection effects when observed from Earth or a spacecraft, the dust trajectories seem to create straight or bended jets, spirals, or shells as it has been observed in many cases (for example Sekanina (1987), Sekanina et al. (2004), Boehnhardt and Birkle (1994), Boehnhardt et al. (1997), Vasundhara et al. (2007)). Figure 1.13 summarizes situations that might occur.

If we consider for example an ideal case where particles are emitted continuously along a straight line from a region at high latitude on the nucleus. It is easy to visualize that the rotation of the nucleus will shape the emission as a cone, its surface formed by the emitted particles. This emission cone could be seen if we were at close distance from the nucleus and could measure the three-dimensional position of the particles. However we are usually observing these structures from far away and we only measure their projected positions in our two-dimensional exposures. For simple geometric considerations the edges of the cone look brighter. This is due to the fact that we integrate the contribution of all particles along the line of sight, therefore we "see" in the edges as much particles as in the rest of the cone, but confined in a narrow line, hence the increase in brightness.

As seen from Earth, the spin axis of the comet can have any orientation, and active regions can be placed anywhere at the surface leading to a great variety of patterns. An emission cone looked side-on will appear as a fan, the borders curvature depending on the trajectory of the particles (based on their properties). However if for the same cone the line of sight is aligned with the spin axis, dust patterns will resemble spirals or shells depending on the activity profile. A continuous activity creating a spiral pattern, whereas an activity modulated by the illumination will create patterns resembling concentric circle arcs (or spiral arcs) in the sunward direction. Figures 1.14 and 1.15 shows more examples of the diversity of structures observed for several comets.
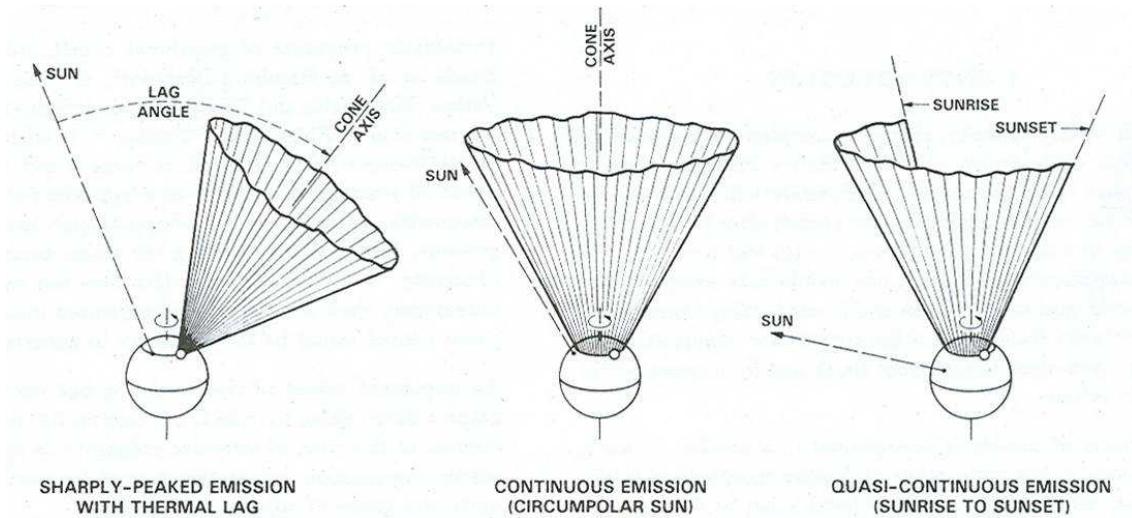
Figure 1.13: Schematic of the creation of a dust structure, from a dust-emitting source at the surface of a rotating nucleus. Sekanina (1987).

1.5   Motivation of this thesis

1.5.1   General motivation for cometary research

We have seen that dynamical studies of comets forced us to reexamine our concept of solar system formation and consider planetary migration as a possible phenomenon which occurred at the early ages of the Solar System.

Comets do not teach us only dynamics. It is important to understand that comets are active for only a very short period of their life. During that time, the nucleus is resurfaced by the activity but only a few meters of the upper surface layers warm up every perihelion passage and the interior of the nucleus remains unaffected at cold temperature. Therefore, the inner core of a comet may still represent the composition of the original material at the time of its formation. Hence comets can be seen as frozen witnesses of our origins.

And not only comets help us to understand the dynamical and chemical processes of the young Solar System, they might also be related to our direct origin, i.e. the apparition of life on Earth. One of the key question to answer for exobiologists is the presence of water on Earth. So far this problem has not been solved but one of the main theories, in relation with the Nice model, is that water could have been brought to Earth by comets or Kuiper belt objects at the time of the Late Heavy Bombardment. This question is highly debated as the ratio of isotopes Deuterium/Hydrogen seems much higher in comets than in the Earth's oceans but several processes might have happened on Earth to change this ratio, and the measurement done on comets might not be representative of the whole situation (see (Laufer et al. 1999)).

1.5.2   About this specific work

We discussed the fact that investigating coma structures reveals information on some dynamical parameters of the comet. The fan shape of a pattern can give clues about the

orientation of the spin axis, while the time delay between layers of a shell can be used to retrieve the rotation period.

This is already quite interesting and is typical of what has been done before (see all articles cited in section 1.4). However we wanted to bring the analysis further in order to get information not only about the dust grains but also about the nucleus surface itself. Studying the surface of a comet is usually very challenging because either the nucleus is too far to be resolved in detail, or it is close enough but its own activity hides all the features we would like to investigate especially the location of active regions. Different modeling methods have been applied to several comets (e.g. Sekanina (1987), Vasundhara (2002)) to simulate ground-based observations of cometary dust activity. These techniques are mainly based on the assumption of point sources of dust emission on the surface of a rotating spherical nucleus. However, from the different cometary flybys, we know that the cometary dust activity is more complex. Active regions can be extended and the nucleus shape is often far from a spherical one. Therefore we wanted to develop a new model, taking in consideration a realistic shape for the nucleus.

Besides the scientific interest leading us to always investigate further to understand the physical processes involved, there is also a more practical motivation for this work: providing support for space missions. In the last two decades, several spacecrafts have been sent to comets, performing various experiments from imaging the nucleus of 1P/Halley to the crash of a probe on 9P/Tempel 1, through the collection of dust grains from 81P/Wild 2. More missions are planned and the following years should see the EPOXI mission (Deep Impact retargeted) visit comet 103P/Hartley 2 in October 2010, NExT (Stardust retargeted) fly by 9P/Tempel 1 in February 2011, and ROSETTA drop a lander on 67P/ Churyumov-Gerasimenko in 2014, while orbiting around the nucleus for several months. This missions are of great value for cometary science, however the environment of an active comet is quite hostile for a spacecraft and the jets of gas and dust represent a hazard for any probe passing at close distance from the nucleus as it happened already to the mission GIOTTO which had several instruments damaged during the flyby of 1P/Halley. Therefore any hint on the local activity, and on the properties of the dust grains, as it could be obtained from a model of dust structures should be taken into consideration to constrain the approach, especially in the case of ROSETTA which will spent the longest time ever in the vicinity of an active nucleus.

The following chapters of this thesis will describe our approach of this problem, from the observation of the coma structures, and the various image processing techniques needed, to the modeling of a realistic dust coma structures around an active nucleus. Finally we will present the results obtained for various targets and discuss how our model will be used in the future to understand better cometary activity.
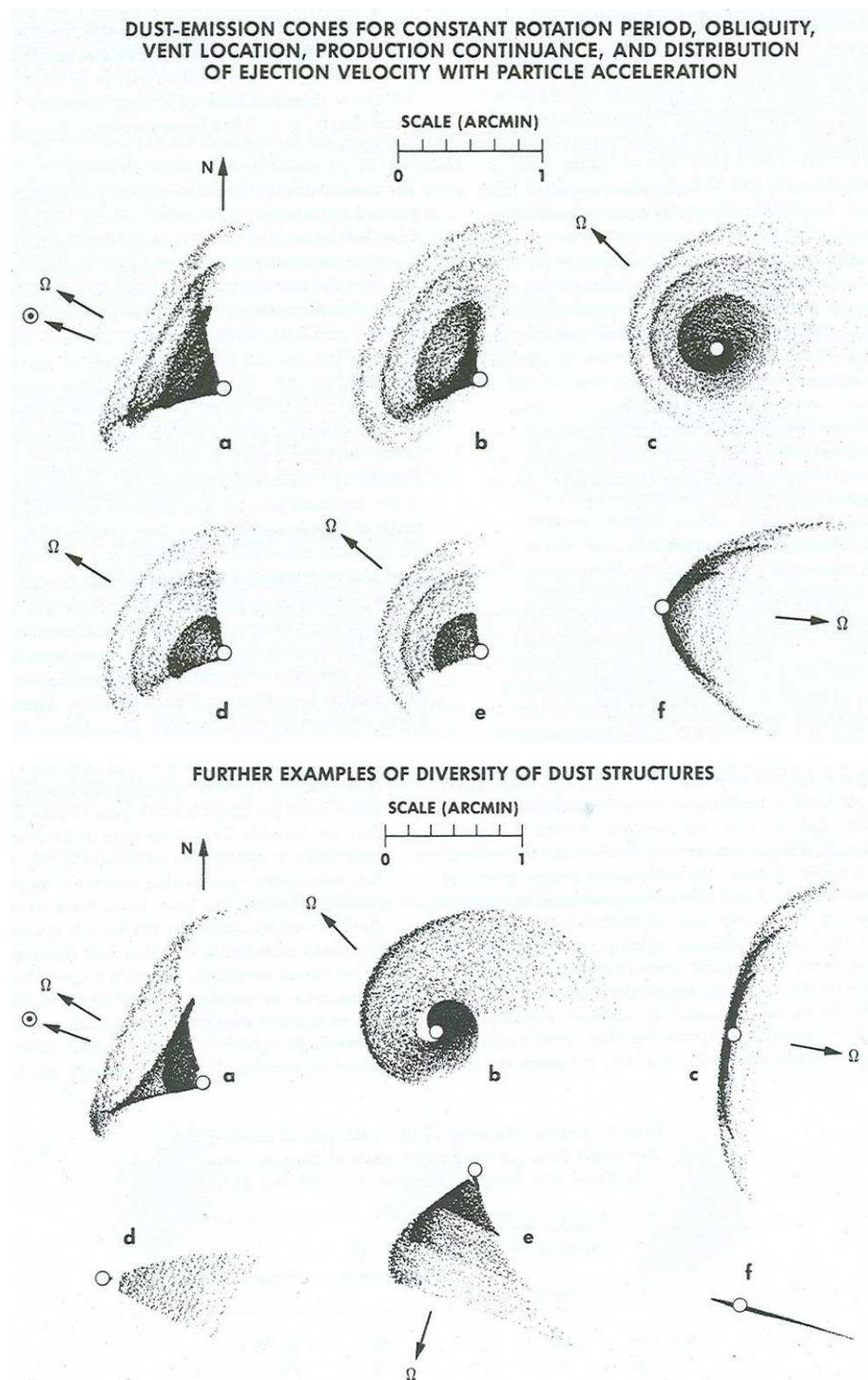
Figure 1.14: Simulations of coma structures showing the great variety of patters one can encounter. Sekanina (1987).
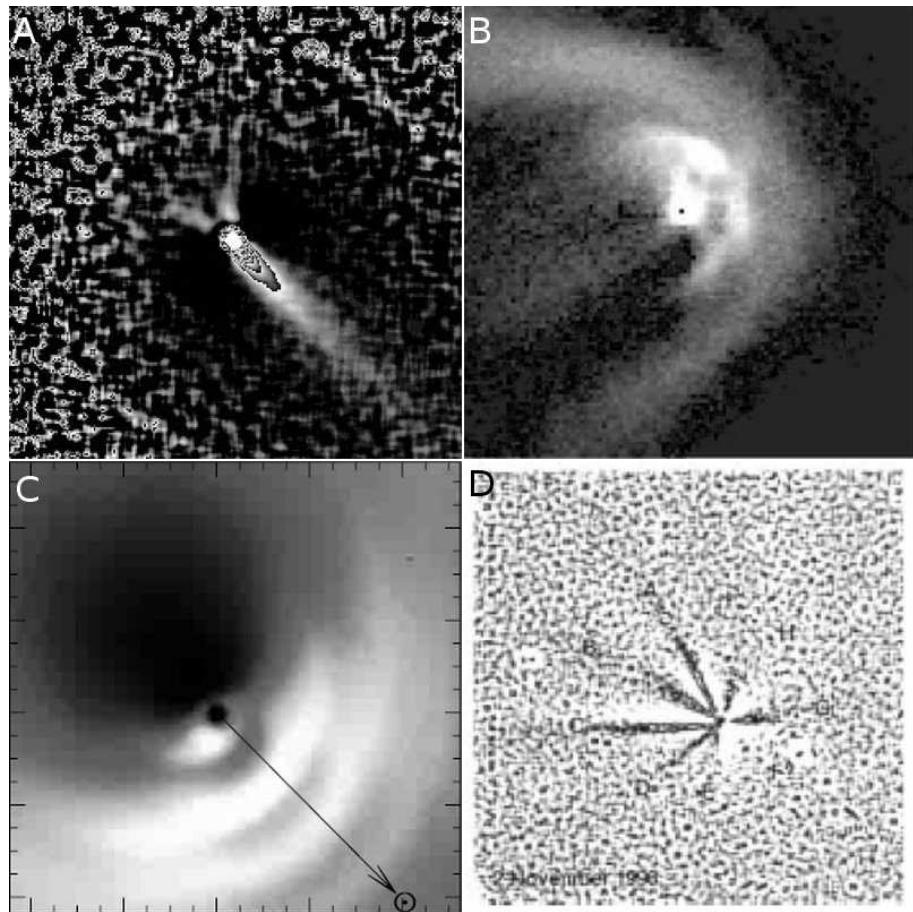
Figure 1.15: Real observations of coma structures for different comets:
A) 73P/Schwassmann-Wachmann 3-C, observed in April 2006 (Vincent et al. 2010a),
B) C/2001 Q4 Neat, observed in May 2004 (Vasundhara et al. 2007),
C) C/1995 O1 Hale-Bopp, observed in April 1997 (Vasundhara 2002),
D) C/1995 O1 Hale-Bopp, observed in November 1998 (Boehnhardt et al. 1997)

2 Image processing goals and steps

At first, one might think that the dust coma of any comet looks boring. Any image you can find shows a spherical or ellipsoidal structure around the nucleus, with no particular features visible apart from an elongation towards the tail direction. This is because the contribution of the dust present in the structures is significantly less than the overall coma background, making any pattern embedded in the coma very difficult to observe.

We have seen in the previous chapter (Figure 1.12) an example of an unprocessed image and an enhanced one. This chapter will present in details the principles of the image processing techniques we use in order to detect and investigate dust structures in ground-based observations. As we will see in the following, several methods can be applied and one has to be aware of the strength and flaws of each method in order to interpret correctly the results.

The work described in this thesis is based on images already reduced by the ground-based observers, and no data reduction was involved form our side. However it might be useful for the reader to get an overview of the data acquisition and reduction. This will be discussed shortly in the first section, then we will continue with the processing techniques.

2.1 From acquisition to reduced images

Not all kind of images are suitable for studying the dust environment of a comet. As explained in Chapter 1, a cometary coma is a very complex environment where different gas and dust material interact. Nonetheless, the dust contribution can be easily resolved from the gas by choosing carefully the wavelength range of the exposures.

2.1.1 Acquisition

Ground based observations of dust consist mostly of broadband images taken in the visible wavelength range with a R Johnson filter (maximum transmission at $\lambda = 630nm$, full width at half-maximum $= 120nm$) or in the near and mid infrared where the contribution of the light scattered by the dust is the most important. One of the key parameters of the observations is the ratio signal/over noise. As stated before, coma structures are very faint when compared to the background, thus we must ensure a good signal over noise ratio (S/N) for the global image in order to increase the chance to detect structures in the coma. For this reason we prefer to use broadband instead of narrowband filters. A narrow band would allow us to choose more precisely the dust we want to observe but it would cost a lot in integration time to achieve a good S/N.

In order not to smear image details due to the motion of the comet, and to avoid saturation of the central coma part, we use exposure series of short integration time (a couple of minutes). These images have then to be reduced to remove the systematic noise from the CCD, which can be divided in two kind of contributions: an additive (bias and dark current) and a multiplicative (flat field) noise.

2.1.2   Reduction steps

Bias: To ensure that each detector of the CCD is working correctly, a test current is applied which has the side effect that a count of electrons is recorded in all pixels. These values may differ from pixel to pixel but remain constant for the observation time. Therefore this noise can be easily measured by taking a few exposures with the instrument shutter closed, and averaging the results.

Dark current: The "dark current" is the thermal noise of the CCD. As the CCDs used are generally operating at very low temperature, it can be completely neglected for exposure times up to few 10 minutes.

Flat field: The sensitivity of the CCD and the optical system is not uniform and can introduce pixel-to-pixels variations and/or a gradient in the image. This effect depends on the wavelength so flat field measurements must be acquired for each filter before the science observation, usually by imaging a neutral surface (illuminated screen inside the dome or the empty sky at twilight).
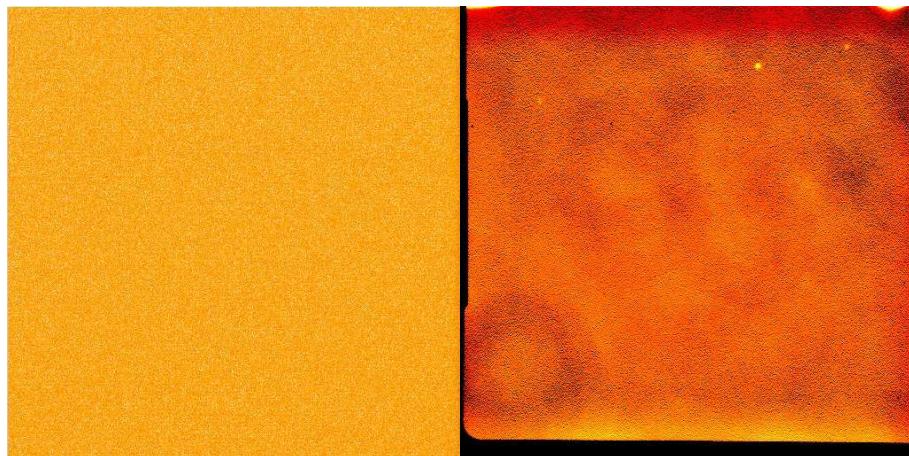
Figure 2.1: Example of a bias image (left panel) and a flat field image (right panel). The bias noise looks like a "salt and pepper" noise evenly distributed in the image. The flat field structure has a lower frequency and appears at random places. Note that the bias noise is also present in the flat field image.

For each pixel (i, j) of the image this signal retrieved by the CCD will be corrected by the following formula:

$$I_{i,j}(\lambda) = \frac{S_{i,j}(\lambda) - b_{i,j}}{F_{i,j}(\lambda) - b_{i,j}} \tag{2.1}$$

where S is the signal, b the bias, and F the flat field.

Finally, the exposures are centered to the comet, combined to improve the S/N ratio, and median averaged to remove the background stars. This assumes that the series of images were of equal exposure times.
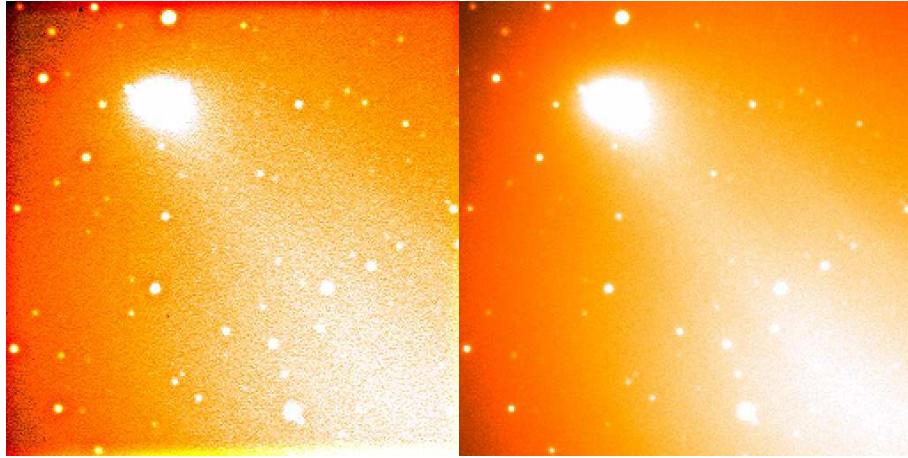
Figure 2.2: Picture of comet 17P/Holmes acquired on 13/11/2007 in Rozhen (National Observatory of Bulgaria), before (left) and after reduction (right).

2.2   Numerical filters

After reduction of the images, it is usually still not possible to distinguish the dust patterns, apart from the tail, because of their low intensity with respect to the coma background.

Different techniques can be applied to enhance the inherent coma structures and will be discussed in the following.

2.2.1   Basic introduction to numerical filtering

With respect to a Cartesian system of coordinates, a digital image can be represented with a bi-dimensional function $f(x, y)$ where the pixel (0,0) is usually in the top-left corner. Images are stored as arrays where each cell contains the information (for instance gray intensity for a monochrome image, or Red-Green-Blue triplets for color images). A spatial filter is a transformation which affects directly the pixels of the original image. The operation can be applied to the whole image at once or only to the neighborhood of a point (x,y), the neighborhood being a sub-array of pixels around the point of interest.

Filters are usually defined with the expression:

$$g(x, y) = T[f(x, y)] \tag{2.2}$$

where g is the new image, calculated by applying an operator T to the original image f.

For most of the filters the operator is not directly applied to the whole image but to a neighborhood of point (x,y). This region is usually square or rectangular in size and centered on (x,y). The process of filtering consists of moving sequentially the origin of the neighborhood from pixel to pixel and applying the operator until all points in the

original image have been processed. Fig. 2.3 shows a schematic of this process. As the neighborhood of a point at an edge of the image contains less pixels than in an other area, the filters have to be slightly modified when processing the edges but the principle remains exactly the same.

Operators (also called *spatial masks* or *kernels*) are often represented by a matrix which summarize the transformation. For a filter of size $m \times n$ the operator can be written:

$$
T = \begin{array}{|c|c|c|c|}
\hline
T_{(-a,-b)} & T_{(-a+1,-b)} & \cdots & T_{(a,-b)} \\
\hline
T_{(-a,-b+1)} & T_{(-a+1,-b+1)} & \cdots & T_{(a,-b+1)} \\
\hline
\cdots & \cdots & T_{(0,0)} & \cdots \\
\hline
T_{(-a,b)} & T_{(-a+1,b)} & \cdots & T_{(a,-b)} \\
\hline
\end{array}
$$

with $a = (m - 1)/2$ and $b = (n - 1)/2$.

The final image can then be calculated as the convolution of T(x,y) with f(x,y):

$$
g(x, y) = T(x, y) \star f(x, y) = \sum_{i=-a}^{+a} \sum_{j=-b}^{+b} T(i, j) f(x + i, y + j) \tag{2.3}
$$

For example the following matrix is a representation of a size 3x3 median filter.

$$
\frac{1}{9} \times \begin{array}{|c|c|c|}
\hline
1 & 1 & 1 \\
\hline
1 & 1 & 1 \\
\hline
1 & 1 & 1 \\
\hline
\end{array}
$$

$$
\Rightarrow \quad g(x, y) = \frac{1}{9} \sum_{i=-1}^{+1} f(x + i, y + i) \tag{2.4}
$$

Each pixel in the filtered image will take the average value of the 3x3 neighborhood of the same pixel in the original image.

From this simple definition, one can build a myriad of filters. Some act on a very general scale, smoothing or averaging the image, while others are specifically designed to remove a certain type of noise or detect particular features in the original images. In the following we will discuss a selection of techniques used specifically for enhancing cometary dust coma structures and how to check whether the structures observed are real or are artifacts created by the filtering process.

2.2.2 Difference filters

These filters are the simplest to implement, yet they are fast and efficient to process images. They usually consist in taking the difference between the original image and the same image slightly processed with a geometric modification (rotation or scaling) or a basic filtering (median or gaussian for example).
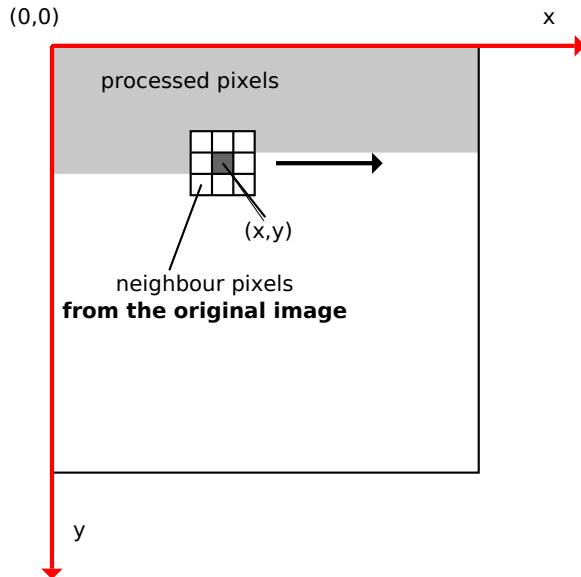
Figure 2.3: Schematic of a 3x3 spatial operator filtering an image.

2.2.2.1   Larson-Sekanina's filter

Among these filters, the Larson-Sekanina one (also called RSD for Rotational-Shift-Difference) is the most widely used for enhancing dust coma structures. Following the description in Larson and Sekanina (1984) one calculates the difference between the original image and a new version which has been rotated and/or radially shifted with respect to a reference point. This allows the detection of small scale variations in all directions in the original image.

In a system with polar coordinates, the image can be described with the function $f(r,\alpha)$ where r is the distance from the origin and α the angle between the point and the x axis. The origin (x_0, y_0) of this new system of coordinates is assigned to the nucleus of the comet.

The algorithm of Larson-Sekanina can be written as:

$$g(r, \alpha, \Delta r, \Delta \alpha) = 2f(r, \alpha) - f(r - \Delta r, \alpha - \Delta \alpha) - f(r - \Delta r, \alpha + \Delta \alpha) \qquad (2.5)$$

We subtract from the original image the same one shifted by Δr and/or rotated by $\pm\Delta\alpha$. Δr and $\Delta\alpha$ are chosen by the user. Typically Δr = a few pixels and $\Delta\alpha \leq 15°$.

Figure 2.4 shows different combination of the parameters for the RSD filter applied to an image of comet C/1996 B2 Hyakutake. We usually distinguish two special cases:

$\Delta r = 0$: We compare the original image with rotated versions of itself. This is useful when the dust structures are more or less radial. The angle of rotation must be chosen carefully to ensure that all structures are detected correctly. If the angle is too small, the structure in the original image and in the rotated ones can overlap, leading to a final structure narrower than it should be. If the angle is too large, we might introduce artifacts as the coma background is usually not isotropic.

$\Delta\alpha = 0°$: We compare the original image with a radially shifted version. This allows the detection of circular structures such as shells or spirals in the coma. For similar reasons as for the rotated image, one must choose a Δr which does not affect the results.
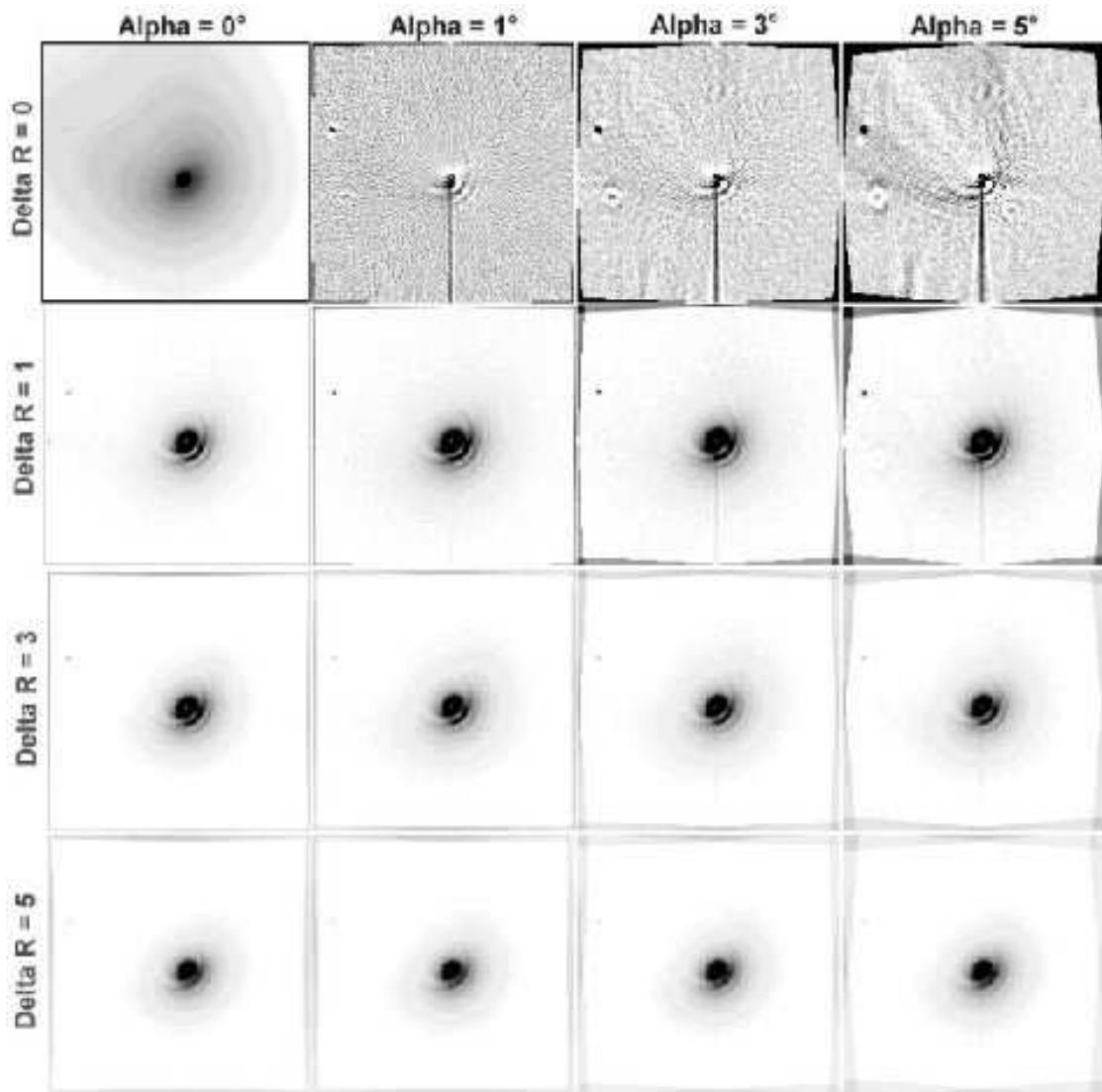
Figure 2.4: different parameters of the Larson-Sekanina filter applied to comet C/1996 B2 Hyakutake on April 28 1996, source: Observatory of Cavezzo
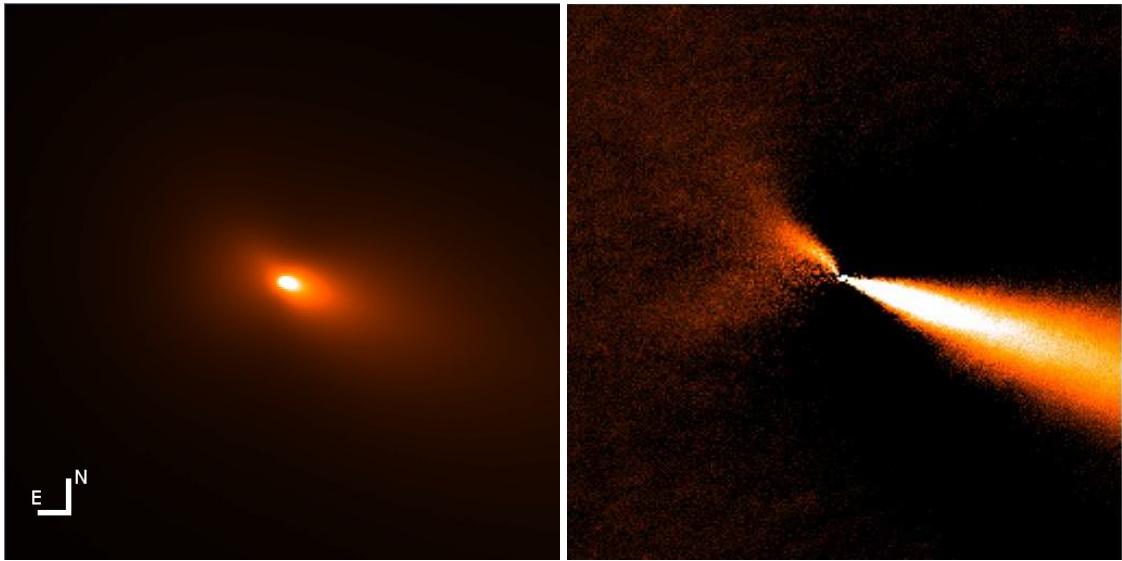
Figure 2.5: Example of the Larson-Sekanina filter applied to an image of comet 73P/Schwassmann-Wachmann 3, component C on 12 May 2006. The left panel shows the original image, the right panel is the filtered one. Parameters: $\Delta r = 0px$, $\Delta \alpha = 7°$ to 15°. Orientation is given in the figure, field of view 135 arcsec × 135 arcsec. Note that the orientation and resolution are the same for all the following images in this chapter.

One common practice is to filter the original image with different parameters and average the results. An example is shown fig. 2.5.

This filter is very powerful to detect structures. However it requires a precise definition of its parameters. The center of rotation can be difficult to determine because the cometary nucleus cannot be resolved in the coma. A possible solution is to consider the brightest pixel as indicating the nucleus position in the image and apply the rotation around it. Decentering is observed to introduce errors in the neighborhood up to a few pixels from the center. Then, one need to adjust the parameters Δr and $\Delta \alpha$ until sure that no artifacts are generated. This problem can be partially avoided by allowing the parameters to vary in a given range and average the final results.

2.2.2.2   Streching-Compression filter

A variant of Larson-Sekanina's technique is the stretching-compression filter. In this approach, the original image is compared with a new version which has been stretched or compressed by a few pixels in radial direction with respect to the coma center. It is somehow similar to a RSD approach with no rotation (shift only) and is very efficient for detecting non radial structures (i.e. spirals or shells). The problem with this technique is that we change the size of the image while trying to keep the information. This implies interpolation of the pixel values from the center to the edges, therefore the quality of the results depends not only on the center position and the scale of the size modification but also on the interpolation algorithm used. Due to the higher number of free parameters, this filter needs more tuning than the RSD for similar results. Thus we did not follow this approach in our study and we mention it only for the reader.

2.2.2.3   Radial normalization

This image processing technique resembles the RSD filter but instead of a rotated/shifted image the comparison is done with a radialy normalized image. This reference image is built form the original one as follows:

$$g(r, \alpha) = \frac{\sum_{\theta=0}^{360} f(r, \theta)}{\text{number of pixels in } C_r} \tag{2.6}$$

where C_r is the cirle of radius r centered on the nucleus position.

Therefore, each pixel in the reference image has an average values of all the pixels located at the same distance from the nucleus in the original image.

The comparison is then done by dividing the original image by the reference or subtracting the latter from the original one. Figure 2.7 shows an example of this filter applied to the same image as in Fig. 2.5. One can notice that the same structures are detected but it is more difficult to really determine their boundaries. Thus this filter should mainly be used as an extra tool in case we have some doubts on features detected by other means. Moreover, as with the Larson-Sekanina filter, we still need a good estimation of the nucleus position to avoid artifacts when creating the average profile. However, this filter provides the possibility to quantify the structure contrast with respect to the general coma background.

2.2.2.4   Unsharp masking

Instead of a geometric change, we can subtract from the original image a slightly processed version of itself. The operator is usually a median or a gaussian filter. The long scale variations in the original image are not affected by the averaging whereas the sharp features are smoothed. The final result (so called *mask*) is defined by

$$g_{mask}(x, y) = f(x, y) - f_{smoothed}(x, y) \tag{2.7}$$

This technique is used traditionally not to detect but to sharpen details in numerical images. The term *mask* refers to a further step:

$$g_{sharpened}(x, y) = f(x, y) + k \times g_{mask}(x, y) \tag{2.8}$$

where the value of k defines the amount of sharpening (how strong the sharpened details should appear in the final image).

Figure 2.6 shows an example of this kind of filtering. The results are similar to what we obtain with Larson-Sekanina's technique for this particular case.

These filters are powerful and widely used to detect structures in cometary comae. However we have seen that they are very sensitive to the initial parameters and a good centering of the image. Moreover, as they perform a comparison by subtraction or division, they depend a lot on the S/N ratio. If the level of noise is too high, it will be very difficult to identify structures in the filtered images.

A better filter should be independent from the user input, and more robust with respect to the noise.
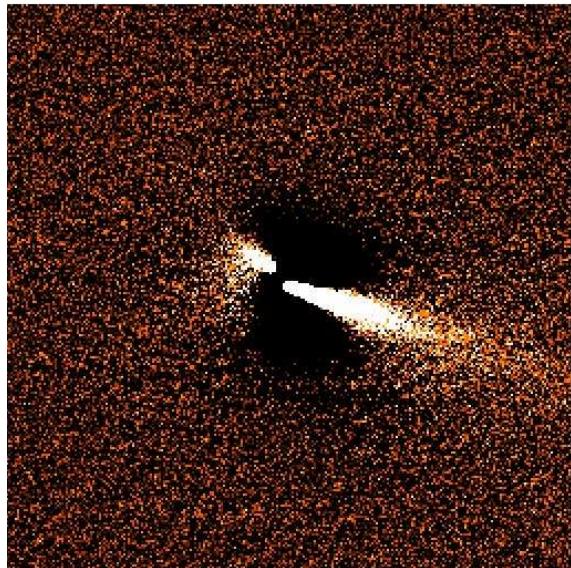
Figure 2.6: Unsharp mask of the same image of comet SW3-C processed with a gaussian filter
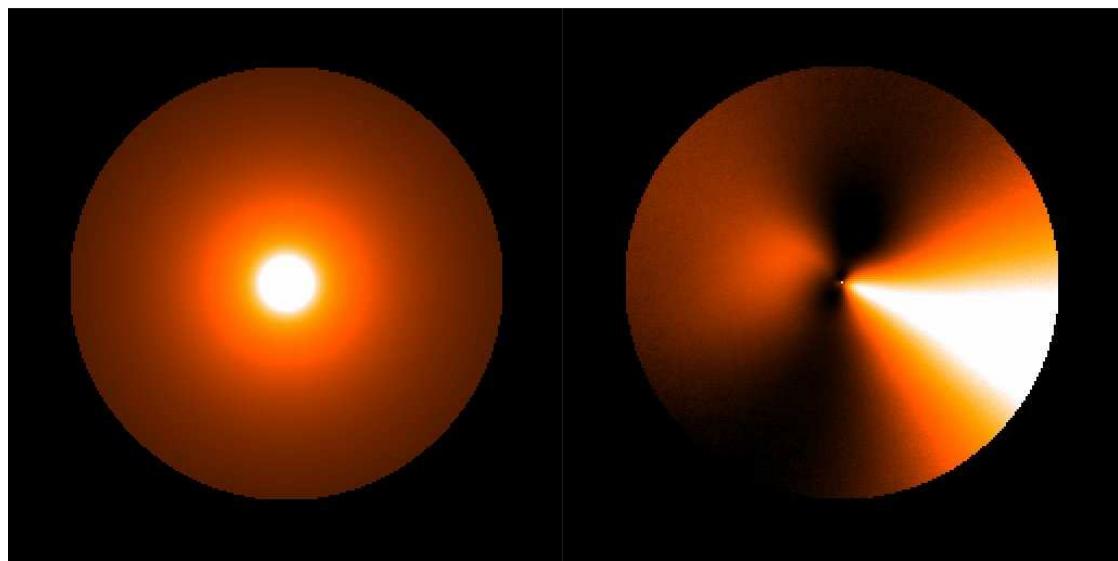
Figure 2.7: Example of the radial normalization filter applied to an image of comet 73P/Schwassmann-Wachmann 3, component C on 12 May 2006 (see Fig. 2.5 for original image). The left panel shows the average profile used as a reference, the right panel displays the original image divided by the reference.

2.2.3   Laplace Filter

The basic idea behind this filter is to calculate the second derivative of the image profile f(x,y) along the two dimensions. By this mean, all the gradual variations (linear and second order gradients) are removed while keeping the fine variations of different scale depending on the width of the numerical filter.

2.2.3.1   Definition of the Laplace operator

If the original image is defined as a bi-dimensional function f(x,y), its second derivative can be calculated with the Laplace operator Δ.

The resulting image is then:

$$g(x, y) = \Delta f(x, y) = \frac{\partial^2 f}{\partial x^2} + \frac{\partial^2 f}{\partial y^2} \tag{2.9}$$

f(x,y) is not analytically defined and exists only as a series of pixel values in the image matrix. Therefore, the derivatives are defined in terms of differences, with the following requirements: The *first derivative* must be zero in areas of constant intensity, and nonzero at the onset and along intensity ramps; the *second derivative* must be zero in constant areas and along intensity ramps of constant slope, and nonzero at the onset and end of intensity ramps.

In one dimension, the derivatives at x are written:

$$\frac{\partial f}{\partial x} \quad = \quad f(x + 1) - f(x) \tag{2.10}$$

$$\frac{\partial^2 f}{\partial x^2} \quad = \quad f(x + 1) + f(x - 1) - 2f(x) \tag{2.11}$$

This can be represented with simple operators:

$$\frac{\partial f}{\partial x} \rightarrow \boxed{0 \mid -1 \mid 1}$$

$$\frac{\partial^2 f}{\partial x^2} \rightarrow \boxed{1 \mid -2 \mid 1}$$

By expanding this definition to two-dimensions and normalizing the filter to the 8 closest neighbors, we get the following mask for the Laplace filter:

$$\frac{1}{8} \times \begin{array}{|c|c|c|} \hline 1 & 1 & 1 \\ \hline 1 & -8 & 1 \\ \hline 1 & 1 & 1 \\ \hline \end{array}$$

After applying the filter, the zero-crossings in the filtered image represent the edges of the fine variations in the original one. This filter works very well to detect structures regardless of their intensity contrast with respect to the background. However the noise in the image might be enhanced as well depending on its scale with respect to the size of the laplacian mask. This problem can be corrected by smoothing the image with an adaptive median filter or a gaussian kernel before applying the Laplace filter.
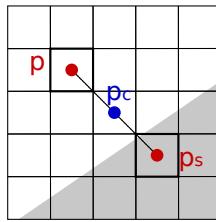
Figure 2.8: Schematic of the adaptive filtering pixel selection, see text for details.

2.2.3.2 Adaptive Laplace filter

As stated before, the quality of the edge detection in the image can be enhanced by a first filtering which can smoothen the noise and help the Laplace filter to detect more easily the structures. However a simple kernel as in eq. 2.4 is not enough. Indeed, the kernel which operates on the image processes each pixel evenly, whatever the local context is. Not only we remove partially the noise, but we also smoothen the edges of the features we want to analyze. A smarter way would be to consider only the relevant pixels in the neighborhood. To define a good criterion of relevance is not easy and several methods exist. We detail here two of them.

Sigma-nearest neighbours: In an image I, if c is the central pixel of the filter mask, we select an other pixel p if and only

$$|I(p) - I(p_c)| < k \cdot \sigma_{\text{noise}}$$

where σ_{noise} is the standard deviation of the noise estimated in non-varying regions of the image, and k a parameter defined by the user (usually k=2 or 3). This method ensures that we average only the pixels within the same intensity levels. However peak noise like the "salt and pepper noise" (pure black or white isolated pixels) are not removed.

Symmetric nearest neighbours: To address this problem, the relevance of the pixels is estimated depending not only on their intensity but also on their position in the image. Considering the same definitions, a pixel p is selected if and only if

$$|I(p) - I(p_c)| < |I(p_s) - I(p_c)|$$

where p, p_s is a pair of central-symmetric pixels. Fig. 2.8 summarize this process. This technique is very useful because it avoids the averaging across edges while smoothing low frequency noise, and removing peak noise.

Figure 2.9 shows an example of this adaptive filtering applied to the same image of comet Schwassmann-Wachmann 3, component C.

2.3 Comparison between the different techniques

Before entering into the details of pros and cons for each filter, one must understand that there is no perfect technique for enhancing dust coma structures. Thus it is necessary to have a good knowledge of the different methods available and select the one which suits the most our needs, depending on the original image.
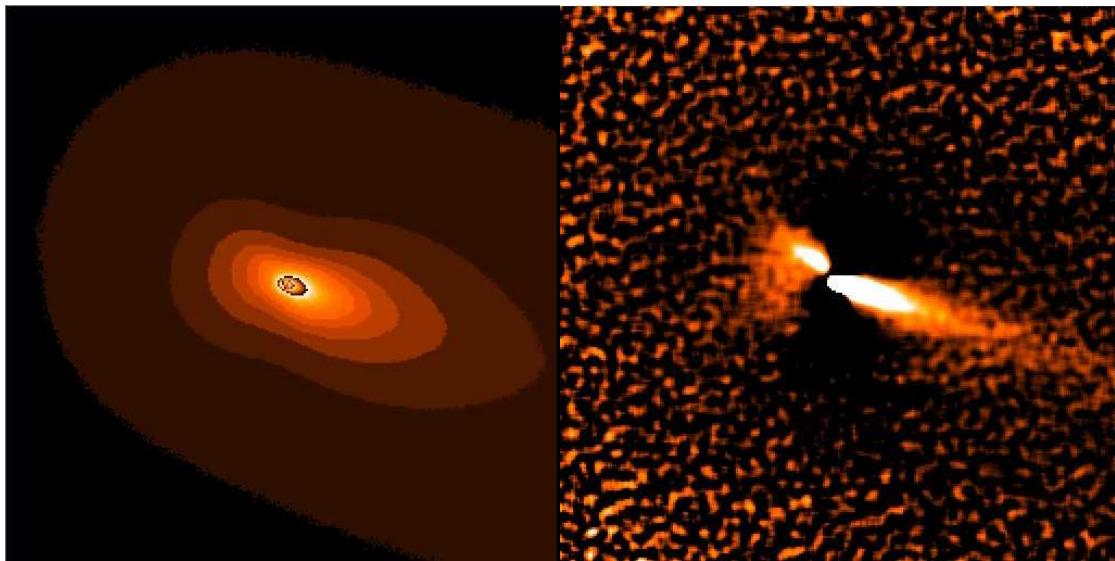
Figure 2.9: The right panel is an example of the adaptive Laplace filter applied to an image of comet 73P/Schwassmann-Wachmann 3, component C on 12 May 2006. The isophotes of the original image in the left panel show clearly a distortion in the direction of the structure.

- Difference filters, as the RSD filter or the radial normalization, are very efficient if the image is not too noisy. Among them Larson-Sekanina's filter gives the best results. Structures are detected very clearly with the finest details with respect to other filters. However it sensitive to the center position in the original image and the parameters for the rotation/shift.

- Derivative filters like the adaptive Laplace technique are more robust and detect features in the coma even with a high level of noise. However the adaptive smoothing is also affecting the finest details of the structures and often makes the measurement of their size difficult.

Figures 2.10 and 2.11 show a comparison between all these filters for two different images, one with a low level of noise, and one with a poorer S/N. One can see that difference filters are more efficient in the first case, with Larson-Sekanina's being clearly the best, while the Laplace filter is better when the level of noise is higher.

In case of doubts about some of the enhanced features, one must always process the images with at least two independent methods, and check whether the same structures are identified with the different techniques. It is generally useful to verify whether we can link structures enhanced by filtering with some deformation of the isophotes in the original images (Fig.2.9).
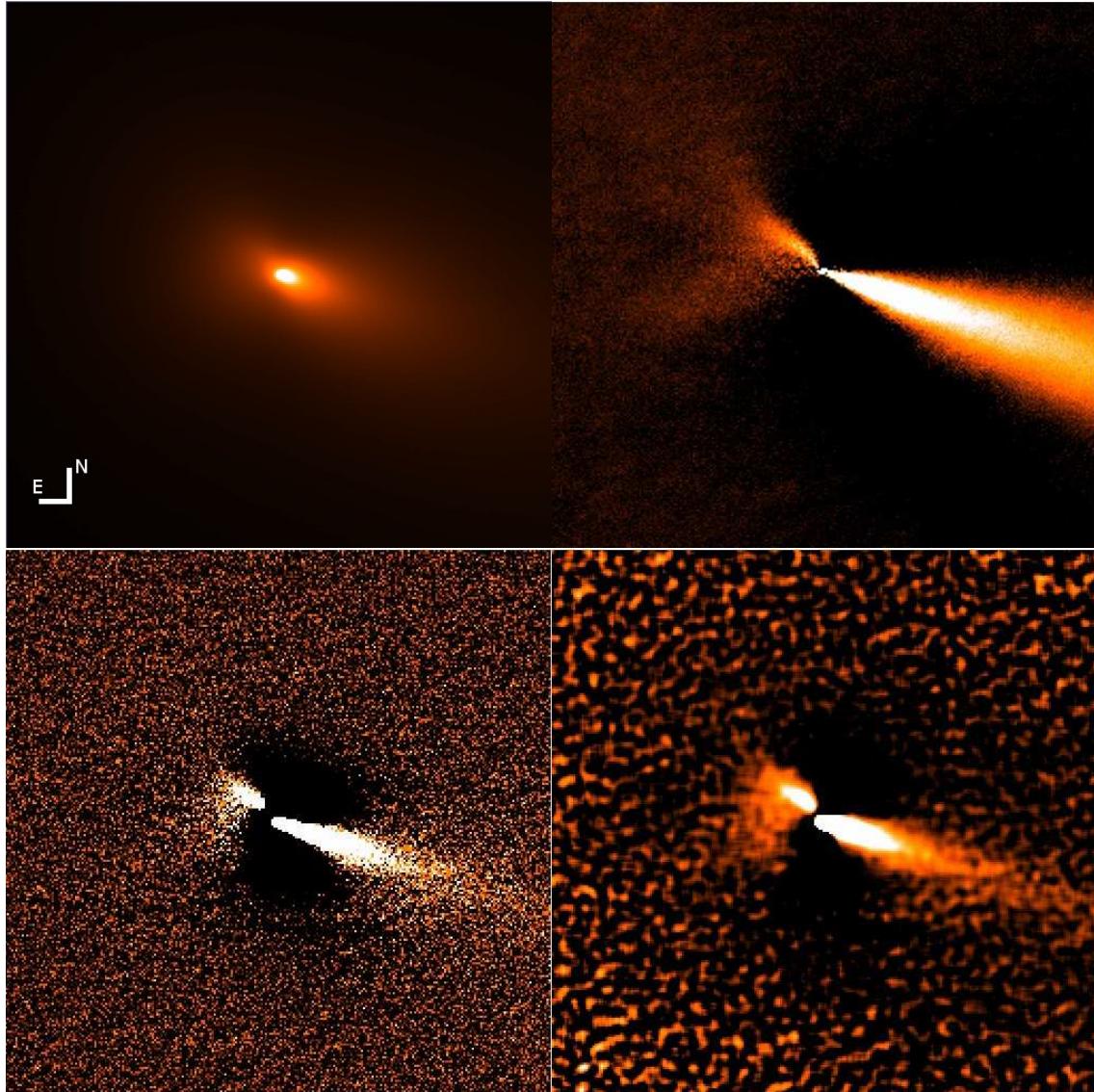
Figure 2.10: Different filters and processing techniques applied to an image of comet Schwassmann-Wachmann 3, component C. The top-left image is unprocessed, the top-right has been filtered with Larson-Sekanina's technique, the bottom-left one with an unsharp masking, and the bottom-right one with an adaptive filter of width 15 pixels. This image has a very good S/N ratio, and the difference filters are the most efficient to enhance the dust structures. Larson-Sekanina's filter is able to detect the finest details of the structure. Field of view 135" × 135", orientation given in the figure.
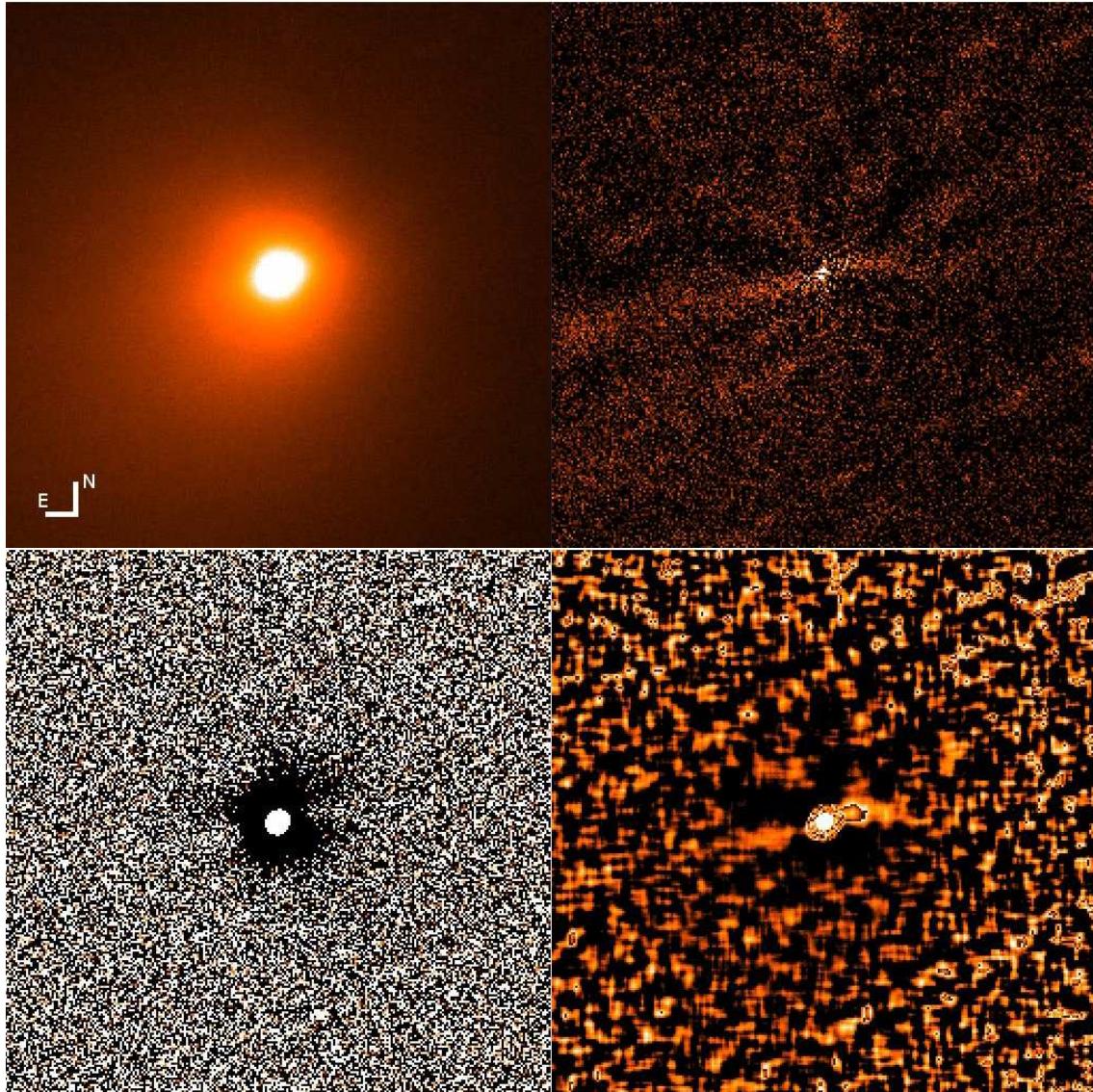
Figure 2.11: Different filters and processing techniques applied to an image of comet Tempel 1. The top-left image is unprocessed, the top-right has been filtered with Larson-Sekanina's technique, the bottom-left one with an unsharp masking, and the bottom-right one with an adaptive filter of width 15 pixels. This image is not as good as the one in Fig. 2.10 and the structures remain hidden in the noise after RSD filtering or unsharp masking whereas they are detected with the Laplace filter. Field of view 2.255" × 135", orientation given in the figure.

3 Numerical model of dust coma structures

This chapter will describe in details the numerical model we developed to simulate dust coma structures. As explained in the introduction chapter of this thesis, several models exist already but were too limited for our needs, especially in the way the nucleus was represented: a simple sphere with active regions defined as source points on the surface. If the main task of the model is to reproduce the observed structures, the idea behind is to retrieve important parameters on the activity and the nucleus itself. Therefore the simulation should not be limited to the ideal spherical case but also allow the nucleus to have an irregular shape. In a similar way, active regions might be source points if the sublimation takes place beneath the surface, with the gas and dust escaping through a vent, but they might as well cover extended parts of the nucleus surface. Thus we developed a new approach considering all these elements, leading to a more realistic simulation.

Before explaining the model, we must take a short digression. As we have seen in Chapter 1.4, the appearance of the structures depends strongly on the geometry of the field of view. The position of the comet in the sky is easy to calculate with basic orbital mechanics (see Appendix A for a reference), but the orientation of the spin axis is often unknown and has to be estimated as accurately as possible before trying to model the structures. The first section of this chapter will present a technique we implemented to extract this information from series of ground-based observations of a comet.

The second section will focus on the model itself and explain the theory behind the numerical simulation, going through all the parameters, along with explanations on the different assumptions or approximations we used and some test cases to illustrate the different kind of output our code produces.

3.1 Determination of the spin axis orientation

To determine the orientation of the spin axis and the rotation period of a comet is not easy. If the active comet extends its tails up to several millions kilometers, the nucleus itself seldom exceeds a few kilometers. When the comet is active, the coma prevents us to see the nucleus surface, and when it is inactive, the nucleus is too small and too far away to allow an identification of surface features which could help in understanding the rotation parameters. One technique generally used consists in reconstructing the rotation phase profile from the light curve of the nucleus (see for example Tubiana et al. (2008)). This approach extracts the rotation period from the light curve by analyzing the frequencies present in the profile and trying to link them to changes in surface shape, color, or spin
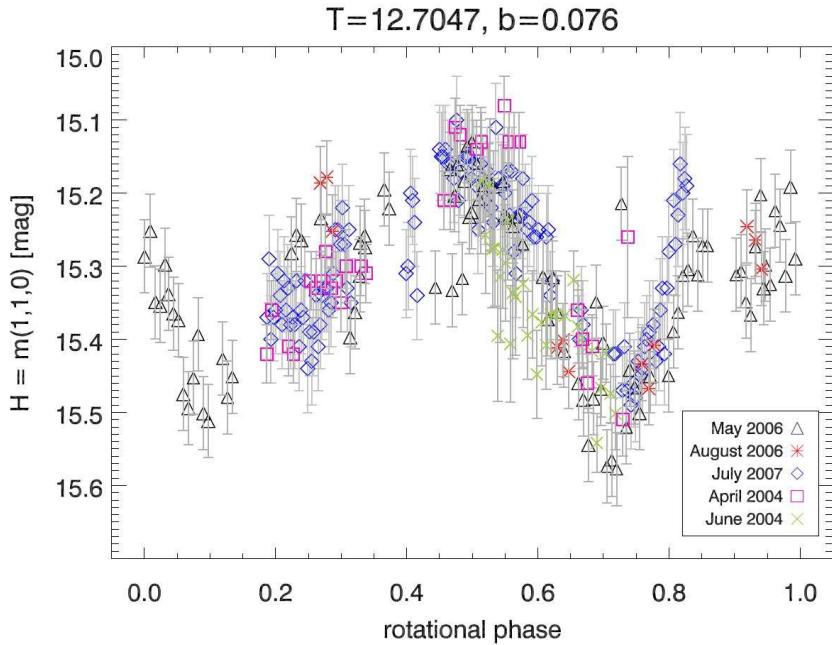
Figure 3.1: Phased light curves of 67P/Churyumov-Gerasimenko measured from ground-based observations. Light curves contain information on the nucleus shape. Credit: C. Tubiana, personal communication

axis orientation. See Fig. 3.1 for an example of a complex light curve.

This method works well for defining the rotation period. However, it is more difficult to use it to constrain accurately the orientation of the spin axis. One can mainly infer whether the axis points towards the observer or makes a large angle with the line of sight, but the value of this angle is often impossible to determine.

Dust coma structures offer a complementary way of analyzing the rotation period. The main advantage of this method is that we are working with active comets, *i.e.* very bright objects. This means that one does not need a long integration time to get an image of the coma structures. Typically a few minutes of observation give enough details to work with. An other argument in favor of this approach is that these structures are usually quite extended (several thousand kilometers) and their appearance depends strongly on the orientation of the spin axis with respect to the line of sight.

Let us consider again the description of dust structures from Sekanina (1987) (See 1.13). An active region at the surface of a rotating nucleus ejects dust grains along an emission cone. We already discussed the appearance of this cone in Chapter 1.4 and we have seen that when viewed from the side, only the borderlines of the cone are visible, appearing as straight or slightly bended lines in the enhanced exposures. Although we do not know the exact orientation of the spin axis, it is totally realistic to assume that its projected position in the plane of sky lies in between the borders of the observed cone. Therefore we can infer the orientation of the spin axis by following this guideline:

- identify structures in the images

- for each image, guess the projected position of the spin axis and measure its position angle.

- using a trial and error approach varying the rotation axis systematically over the 4π sphere of the nucleus, determine the orientation of the spin axis as the one giving a simulated projected position on the plane of sky the closest to the estimated one for all the observation dates.
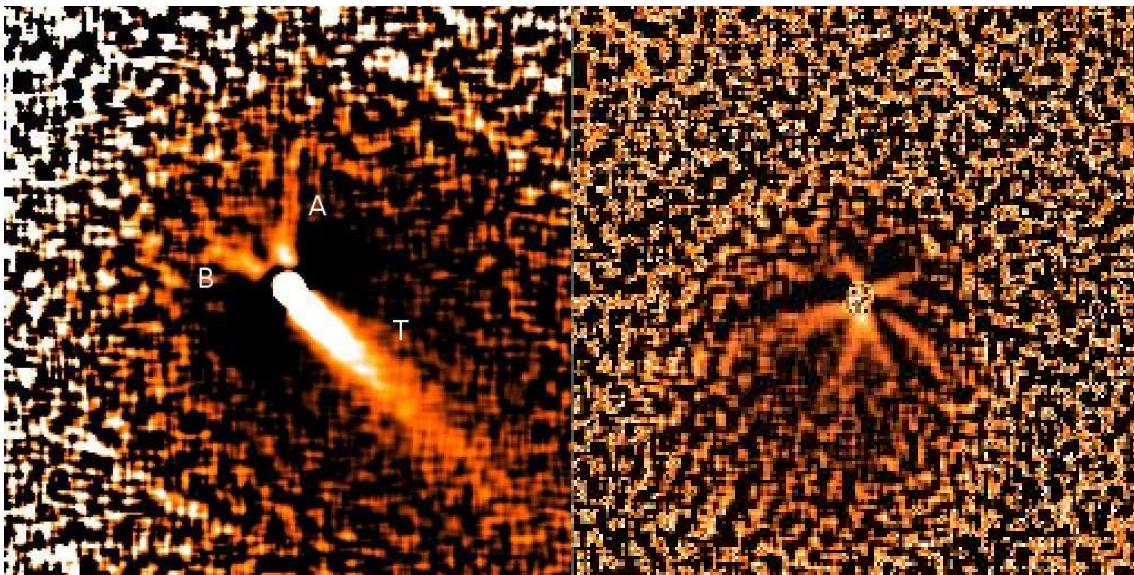
Figure 3.2: These two images are a good example of the difficulties one might encounter when trying to define the orientation of the spin axis, as explained in the text. Left panel is comet 73P/Schwassmann-Wachmann 3, component C, and the right panel is comet 9P/Tempel 1.

This approach is very efficient and provides reliable results as we will see in the next chapter. However one need to be cautious in the first steps. Figure 3.2 shows examples of coma structures for two different comets. The left panel is quite easy to understand. It displays an enhanced image of the dust coma of comet 73P/Schwassmann-Wachmann 3, component C. The large feature labeled T in the image is the dust tail. The two patterns A and B in the opposite direction are a typical example of structures forming straight lines. It is not completely clear if the two structures are independent or borderlines of a single emission cone but in this case we concluded on the latter option by studying the evolution of this pattern over several months (see chapter 4.1.1 for all the details of the study). Therefore it was quite straightforward to assume a projected position of the spin axis in between the two observed structures.

The right panel of figure 3.2 is more difficult to understand. There are at least seven patterns visible, with similar appearance. Hence defining the projected position of the spin axis requires a strong experience of that kind of images, namely being aware of the possible projection effects in order to interpret correctly the patterns. As the position of the Sun with respect to the comet can be calculated easily from the orbital elements, one can first use this information to identify the dust tail. Then the position of the rotation axis

can be guessed from the remaining features. In that case several positions can be assumed but this ambiguity disappears when we use a sequence of images of the same structures over a time period of several months.

Once estimated the position of the spin axis, we run a code which calculates the projected position of the axis in the plane of sky for each possible orientation of the axis in the 4π sphere of the nucleus, and for each observation date. A least squares algorithm is finally applied to estimate the best spin axis, i.e. the one whose projected position is the closest to our initial guesses.

This technique gives good results even in complicated cases as we will see in chapter 4.2. However it uses one assumption that we did not discuss so far. The spin axis orientation is supposed to be constant over the observation period. If this might be true for a couple of days of imaging the comet, can we still make this assumption when we work with series of images covering several months? The spin axis orientation of an active comets can be affected by several processes like asymmetric activity, outbursts, or fragmentation events leading to a precession or more dramatic changes. However we believe that unless a big event affects the comet (for example the giant outburst of comet Holmes in October 2008), the change in orientation of the spin axis will not be larger than our error in measuring the position of the structures. As the filtering process can blur or distort the borders of the structures, it is sometimes not trivial to measure their exact position, at least without an uncertainty of at least a few degrees. Therefore we usually assume an uncertainty of 10°when estimating the projected position of the spin axis in the enhanced images, any orientation change within this limit will be unnoticed in the observations.

Finally, when the spin axis orientation is defined, one can start modeling the dust coma structures.

3.2 The theory behind the numerical model.

"Modeling the properties of the dust particles ejected from comets is one of the most formidable tasks in cometary physics, as we have little or no information about numerous parameters describing these dust grains" Fulle (2004).

The main difficulty one may face when trying to model cometary dust is not only the lack of information on each of the necessary parameters, but also the fact that we do not have yet a complete understanding of how this parameters interact. For instance, should we take into account the particles shape when calculating the effect of the solar radiation pressure ? How do you infer for what happens in the inner coma where several gas flows are likely to interact with the dust ? In the course of this chapter, we will try to examine all the parameters to consider, and see how we can combine them together to build a coherent view of the different processes involved. We will first look at the well known theory about the motion of the grains in the vacuum far from the comet and continue with less understood phenomena happening in the coma, until we reach a description of what happens close to the surface.

3.2.1   Equation of motion for the dust particles

It is commonly accepted that the gas produced by the sublimation of surface or inner ice escapes into the vacuum, dragging along dust grains. The distance where this acceleration occurs depends on the size of the grains and the density of the gas but is typically about a few nucleus radii. Beyond this distance, the density of the gas becomes too low to affect the dust grains and they follow their own trajectories based on the combination of the following forces:

Solar Gravity	1
Radiation Pressure	0.5
Lorentz Force	2.10^{-2}
Pressure in the coma	2.10^{-4}
Poynting - Robertson Effect	5.10^{-5}
Collisions with solar wind particles	2.10^{-5}
Comet Gravity	1.10^{-5}
Coulomb Force	2.10^{-7}

The numbers in the right column of the table above indicate the intensity of each force with respect to the solar gravity. Of course these effects depend on the grain properties and we give here only an average value for the different forces. We can notice nonetheless that most of them can be neglected as their intensity is several orders of magnitudes smaller than the solar gravity. Only two forces remain and must be considered when calculating the motion of the dust particles.

Solar gravity: It is the most important force and affects the dust particles likewise any other body orbiting in the solar system. For spherical grains of constant bulk density the radiation force can be written as:

$$F_{grav} = \frac{\rho_d \pi d^3}{6} \left(\frac{GM_\odot}{r^2} \right) \text{in the direction of the Sun} \tag{3.1}$$

where d is the diameter of the grain, ρ_d its density, and r the distance Sun - comet. G and $M_\odot$ represents the gravitational constant and the mass of the Sun.

Radiation pressure: The second force in our list describes how much the trajectory of the dust grains is affected by the solar radiation pressure. In a non-relativistic approximation, it is expressed as:

$$F_{rad} = \frac{\pi d^2}{4} \frac{Q_{pr}}{c} \left(\frac{E_\odot}{4\pi r^2} \right) \text{in the anti-solar direction} \tag{3.2}$$

with $E_\odot$ the solar luminosity, and c the speed of light. Q_{pr} an efficiency factor for the radiation pressure obtained from the Mie scattering theory.

Light scattering is an important process in cometary science because it is what makes the dust coma and tail visible. The Mie theory (Mie (1908)) tries to predict the light intensity and polarization from the scattering angle. It was developed for well defined particles shapes and it is more difficult to apply it to real grains which are more fluffy and irregular. However it is used as an approximation in most of the cases. Fig. 3.3 describes the interaction between a radiation and a particle. Part of the incoming radiation

is absorbed by the particle while the rest is scattered with a certain angle θ with respect to the original direction. The loss of energy is represented by dimensionless coefficients, so-called efficiency factors, and the interaction can be described by:

$$Q_{ext} = Q_{abs} + Q_{sca} \qquad (3.3)$$

with Q_{ext} the total extinction, Q_{abs} the energy absorbed, and Q_{sca} the energy scattered.

In addition to the energy, the radiation can also be seen as a particle carrying some momentum. The interaction will exert a force, e.g. the radiation pressure, on the dust grain. The efficiency for the radiation pressure is given by the difference between the total extinction and the amount of scattered light.

$$Q_{pr} = Q_{ext} - Q_{sca}.\cos\theta \qquad (3.4)$$

where θ is the angle measuring the deviation the scattered beam from its initial direction.
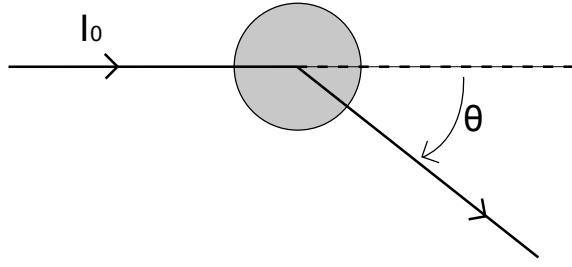
Figure 3.3: Schematic of the interaction between a light beam and a dust particle

The values of the different efficiency factors depend on several parameters a priori unknown, such as the material or shape of the dust particles. A precise calculation of the two forces requires also to know the mass or density of the particles, which is also not available. One way to simplify the problem is to notice that both gravity and radiation pressure are forces varying in $1/r^2$ where r is the heliocentric distance.

Hence, following the idea Finson and Probstein (1968) developed for the dust tail, one can define a new parameter β as the ratio of the two forces.

$$\beta = \frac{F_{rad}}{F_{grav}} = \frac{3Q_{pr}E_\odot}{8\pi cGM_\odot} \frac{1}{\rho d} \qquad (3.5)$$

where ρ and d are the density and diameter of the grain, Q_{pr} the efficiency factor of the radiation pressure, c the speed of light, G the gravitational constant, $E_\odot$ and $M_\odot$ the solar luminosity and the mass of the Sun.

From there we can simply consider the particles affected by a single force and the equation of motion for a dust grain becomes:

$$m_d.a_d = F_{grav}(1 - \beta) \qquad (3.6)$$

where m_d and a_d are the mass and acceleration of the particle.

Equation 3.5 shows that the β parameter depends on the properties of the dust grains (Q_{pr}, ρ, d) which are usually unknown. Experimental measurements have been taken for

different kind of material and examples can be found in Burns et al. (1979). Figure 3.4 summarize some of this values. One can notice that for grains bigger than 0.1 micrometers, β can be approximated with

$$\beta \simeq \frac{k}{d} \tag{3.7}$$

where k is a constant depending on the material. For relevant material, Burns et al. (1979) showed that $k = 4.10^{-7}$ is a good approximation if the composition of the grains is unknown (see Fig. 3.4 for a plot of β as a function of the grain size).
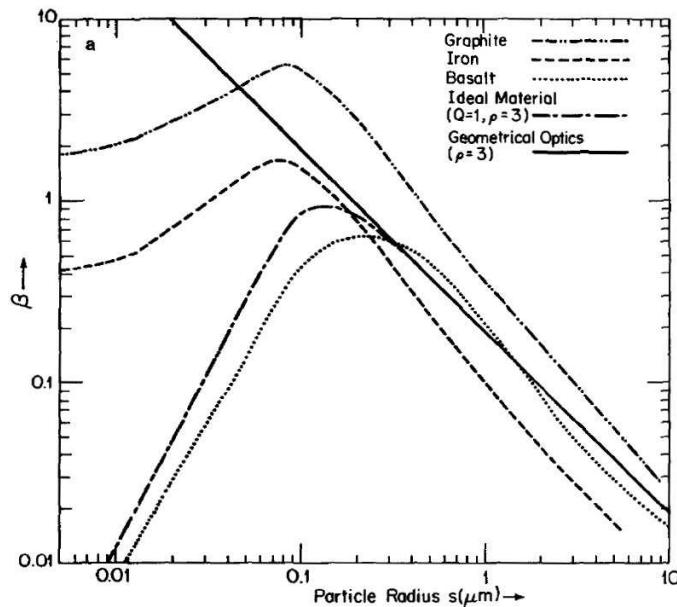
Figure 3.4: A log-log plot of the relative radiation pressure force $\beta = \dfrac{F_{rad}}{F_{grav}}$ as a function of particle size for different material. Adapted from Burns et al. (1979)

Given equation 3.6 and the orbital elements of the comet, it is relatively easy to calculate the position of the dust grains with respect to the nucleus and its projection in the observer's plane of sky (see Appendix A for the equations). However the integration of the equation of motion requires initial parameters on the dust grains such as their size, velocity, β, initial direction...

As we will discuss below, some of these parameters are not necessarily known a priori or well enough. They must be approximated through educated guesses first, and can be refined later depending on the results of the simulations.

3.2.2   Dust parameters

When developing a numerical model, one has to be careful with the number of parameters used in the simulation. The quality of the result does not always increase with the number of parameters, and more variables means also more processing power required to obtain a good simulation. Therefore, we must first decide which parameters play an important role in the model, and which ones can be neglected or approximated in an realistic way. It is

also interesting to look at how the interdependencies between the parameters can improve the efficiency of the code. For example, we have already encountered the β parameter in the previous section and discussed its relation to the grain size and material. Even if the composition of the grains is unknown, we can still approximate β very well as a function of the diameter of the grains. Hence knowing the size distribution of the dust is enough to constrain their sensitivity to the radiation pressure. As we will see later on, we can derive also easily the initial velocity from β and the size. Therefore the diameter of the particles will be our main parameter for the simulation.

3.2.2.1 Size distribution

What is the typical size of particles one can find in the coma structures ? The answer is not trivial as it depends on the formation and evolution of the nucleus surface, but simple orbital consideration and existing observations can help to constrain this parameter. The trajectory of the dust grains after they release depends mainly on their sensitivity to the radiation pressure, hence their size. Small particles (micrometer size) are more likely to have a high value of β and therefore be pushed away from the comet orbit, whereas bigger grains (millimeter size or larger) experience a negligible pressure and follow the same trajectory as the nucleus itself. The grains observed in coma structures can take any value within this range. Some jets are observed to be strongly affected by the radiation pressure while other grain trajectories are undisturbed even though the grains are emitted in solar direction, leading to straight radial structures. In January 2004, the mission Stardust encountered comet 81P/Wild 2 and collected dust grains from the coma. Tuzzolino et al. (2004) reported measurements of the grains sizes in the coma. They observed particles with a diameter ranging between 3 μm and 2000 μm; the number of particles being an inverse power law of the grain size, adding up to the list of similar results obtained for other comets on board different spacecrafts (VeGa 1 and 2 and Giotto at comet 1P/Halley in 1986 Giotto at comet 26P/Grigg-Skjellerup in 1992).

As we write, nobody is able to calculate the exact size distribution of dust grains in a coma. This issue may be solved after the mission ROSETTA will put a lander at the surface of comet 67P/Churyumov-Gerasimenko, allowing us to investigate in-situ the sublimation and constrain better the size, mass, and type of particles released from the surface. Meanwhile we should rely on empirical laws, which might not reflect totally the reality but are nonetheless very good approximations. As said before it is generally observed that the size distribution follows an inverse power law defined as:

$$\text{number of particles of size } d = \begin{cases} d^{-\alpha} & \text{if } d_{min} \leq d \leq d_{max} \\ 0 & \text{elsewhere.} \end{cases} \tag{3.8}$$

α can be measured from astronomical images (see for example Fulle (1999), Markovich and Markovich (2001), or Min et al. (2005)) and its values usually ranges between 2.5 and 3.0 for grains with a size varying from micrometer to millimeter.

When running our simulation code, the user can choose a value for the power α, and indicates a range of size within which the distribution will be defined.

3.2.2.2   Initial velocity

After constraining the size and sensitivity to the radiation pressure, we can now discuss the initial velocity of the dust grains. Our model does not simulate the initial acceleration phase of the dust particles, when they are lifted from the surface and accelerated by the gas. This process is still not fully understood as we don't know whether the particles are ejected directly from the surface or from the inner nucleus through a vent, and how the different gas flows in the coma affect this process. Some models exists but they were not directly fitting our needs. For example Crifo et al. (2005) developed a multifluid modeling of the circumnuclear dust coma which seems promising, but his model is restricted to a nonrotating spherical nucleus. Nevertheless, an empirical formula has been derived from observations and suits very well our purpose. Fulle (1987) obtained an equation for the terminal velocity of the dust (i.e. speed acquired during the acceleration phase) as a function of both the grains size and the β parameter which can be written as:

$$v = v_0 \beta^{1/6} \qquad (m.s^{-1}) \tag{3.9}$$

where v_0 is constant for a given heliocentric distance.

This formula assumes an isotropic distribution of dust velocities in the inner coma, which might be unrealistic due to the complexity of this environment. A better model needs to consider a multi fluid approach for the gas, combined with a Monte Carlo modeling of the dust as in Crifo et al. (2005). However, the simplistic approach has been proven to be sufficient in first order approximation to simulate the dust structures in ground-based observations (e.g. Vasundhara et al. (2007)).

So far we have defined almost all the necessary parameters for calculating the motion of the dust grains. Equations 3.8, 3.7, and 3.9 define the size distribution, the β parameter, and the initial velocity. Figure 3.5 shows an example of this values calculated for a set of 500 particles with a distribution size defined with ($dmin = 1\mu m$, $dmax = 100\mu m$, $\alpha = -2.75$).

3.2.2.3   Ejection geometry

The last parameters needed to fully constrain the motion of the dust grains are the geometrical conditions at the surface. The emission geometry is very important for the simulation of the observed structures but whether we have a collimated jet or an emission cone depends on many parameters like the dynamics of the gas lifting up the dust, the size of the active region, the roughness of the terrain,... which are mainly unknown. However during spacecraft flybys of several comets, it has been observed that most of the dust is emitted in collimated jets (see for example 9P/Borelly (Thomas et al. 2001) or 82P/Wild 2 (Sekanina et al. 2004)). Concerning the initial direction of motion, the first idea when implementing this model was to allow the emission angle to take any value pointing outside of the local surface. However we realized that an emission orthogonal to the surface was enough to constrain very well the location of the active regions. While this definition might not be true for all comets, it is good enough for the simulation of our ground-based images. We will develop this idea more in details in the chapter 4.2 where we will present an application of this model to a real comet and discuss the validity of our hypothesis. For now, we will consider that the initial geometry of emission can be fully derived from the shape model of the nucleus.
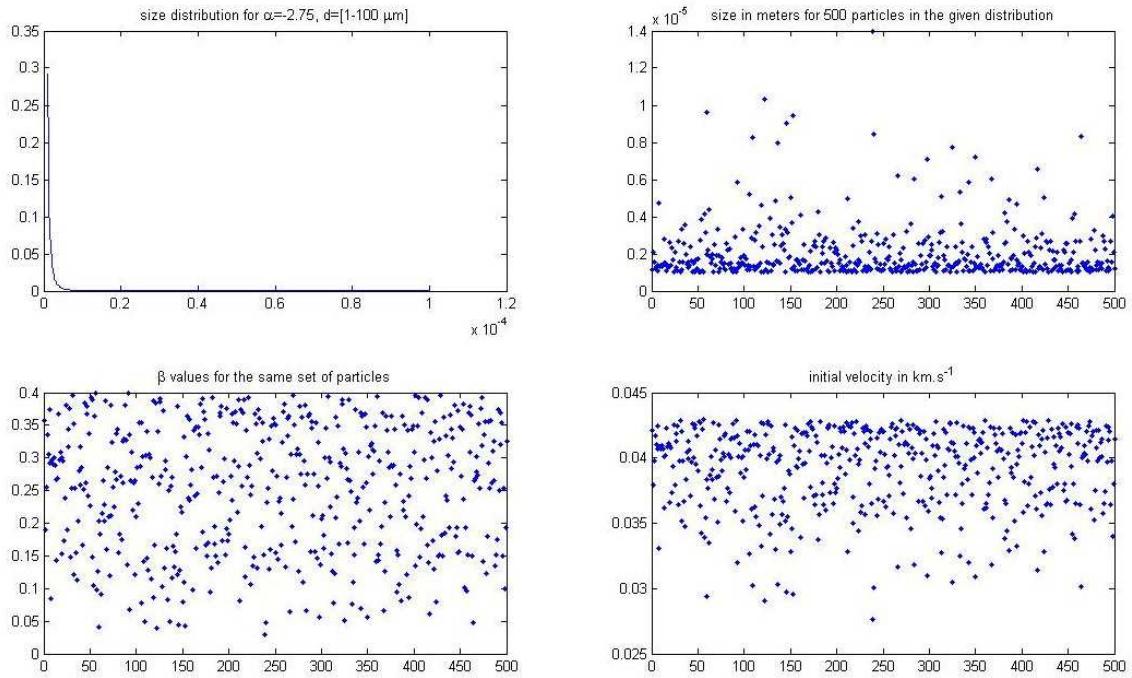
Figure 3.5: Size, initial velocity, and β value of 500 particles defined by the size distribution parameter $\alpha = -2.75$ in Eq. 3.8

3.2.3   Nucleus parameters

3.2.3.1   Position, spin orientation, and rotation period

We intend to reproduce ground-based observations of the dust coma structures. As stated before, the appearance of these patterns projected in the plane of sky depends strongly on the geometry of the field of view and the relative positions of the Sun, the Earth, and the target comet. The orbital configuration of the system is quite easy to calculate and does not require complex models. As for many bodies following a keplerian orbit, the trajectory can be fully constrained from a limited set of orbital elements. They are usually available for all celestial bodies in the JPL/HORIZON website (`http://ssd.jpl.nasa.gov/horizons.cgi`), or can be estimated from different observations if we investigate a newly discovered object. We will not discuss here the details of the orbital calculations, but one can find a summary of the different steps in Appendix (A.)

We already discussed the determination of the spin axis orientation and the rotation period. If these parameters are not available for our target, we estimate them with the technique described above.

3.2.3.2   Shape

So far, only six comets have been visited by spacecraft, with imaging of the nucleus for four of them: 1P/Halley (1986), 19P/Borelly (2001), 81P/Wild 2 (2004), and 9P/Tempel 1 (2005). These images are of incomparable value for understanding cometary nuclei and brought us many information, along with new questions we still have to answer. Regarding the shape of the nuclei, we learnt that they are far from spherical (see Fig.3.6).

Indeed the four nuclei observed presented irregular shapes and complex topography with features like craters, hills, rough surface or smooth regions. A direct consequence of considering a complex shape instead of a sphere is the calculation of the illumination at the surface. Depending on the topography, a region of the nucleus will receive a different amount of light per day than in the spherical case. In certain conditions some regions which would experience a day and night time if the nucleus would be spherical can remain completely unilluminated for the whole period, simply because of the shadows created by the shape of the nucleus itself (see Fig.3.7 for an example). In their study of comet 9P/Tempel 1, Groussin et al. (2007) derived a thermal model of the sunlit hemisphere of the nucleus showing huge variations of the surface temperature (from 272 ± 7 to $336 \pm 7K$) matching the surface topography and incidence angle. This confirms our view the real illumination calculated from the shape model must be considered in order to build a realistic simulation.
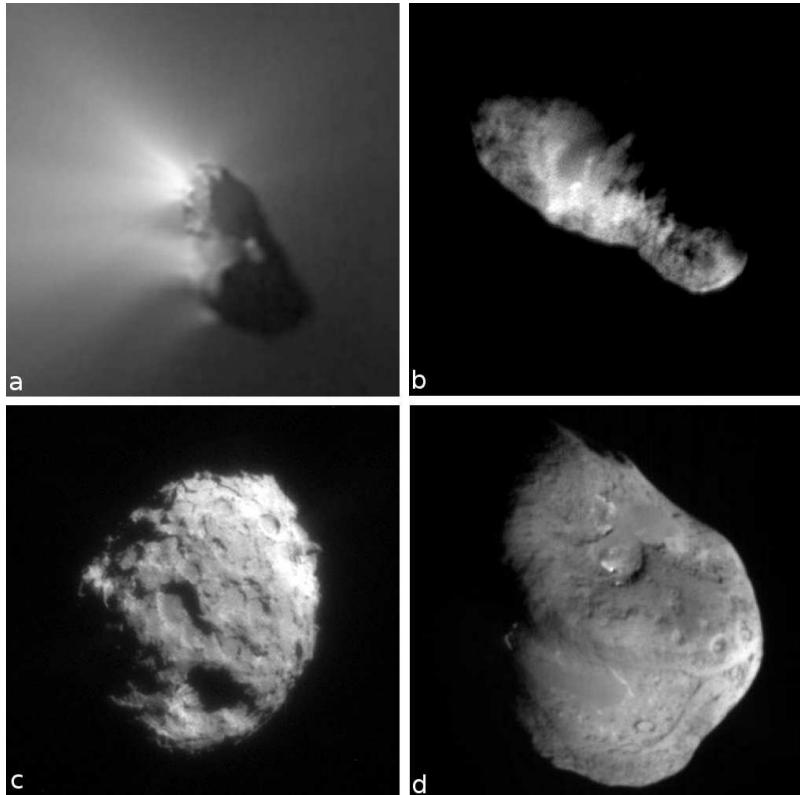

Figure 3.6: Close views of the four cometary nuclei visited by spacecrafts: (a) 1P/Halley, mission Giotto, March 86; (b) 19P/Borelly, mission Deep Space 1, September 2001; (c) 81P/Wild 2, mission Stardust, January 2004; (d) 9P/Tempel 1, mission Deep Impact, July 2005. The different nuclei display a great variety of shapes, far from an ideal sphere.
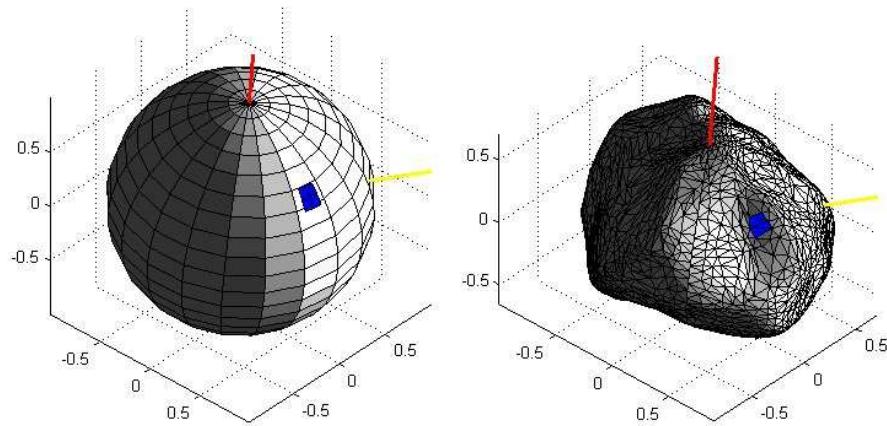
Figure 3.7: Illustration of the effect of the shape on the illumination. These two images represent a cometary nucleus with a spherical shape on the left panel, and with a realistic three-dimensional model on the right (indeed the shape model of comet 9P/Tempel 1). The red line indicates the positive pole of rotation, the yellow line points towards the Sun, and the blue patch represents an active region. This area is illuminated in the spherical case whereas at the same time it is in the shadows if we consider the real topography.

Our model can use any kind of 3-dimensional shape, from a sphere to a complex body with irregular features. There exist many different numerical format to describe such an object. For performance reasons, we defined our own to store the shape model, along with a code to convert from a standard file to our format. It can be seen as a binary version of the OBJ format (ASCII specification defined at `http://local.wasp.uwa.edu.au/~pbourke/dataformats/obj/`) with some simplification as we do not consider any color or texture mapping in our model.

In a nutshell, the surface is represented as a polygonal mesh where each facet is identified by a set of coordinates defining the vertices and the vector normal to the facet. Polygons can be triangles or squares depending on the original file format. From this definition, with the position of the Sun and comet known, we can easily calculate the illumination of each facet with a basic raycasting algorithm. If the facet can "see" the Sun, i.e. there is no topographic obstacle between the sun and the center of the facet, the illumination is defined as the sine of the elevation angle of the Sun with respect to the local horizon. This approach provides a realistic estimation of the amount of light received by each surface element even for a very complex shape. On the opposite case, if the nucleus is a pure sphere, the illumination profile calculated with this technique is equivalent to a cosine function.

3.2.3.3   Definition of active regions

Usually, active regions are identified by their local coordinates (latitude & longitude) on the surface. Our model includes the possibility to consider such areas as point source or extended surfaces. The source point option is useful as a first order approximation but may be unrealistic as we know that active regions can be extended. A large area can still be approximated by a source point with a large emission cone but this approach is
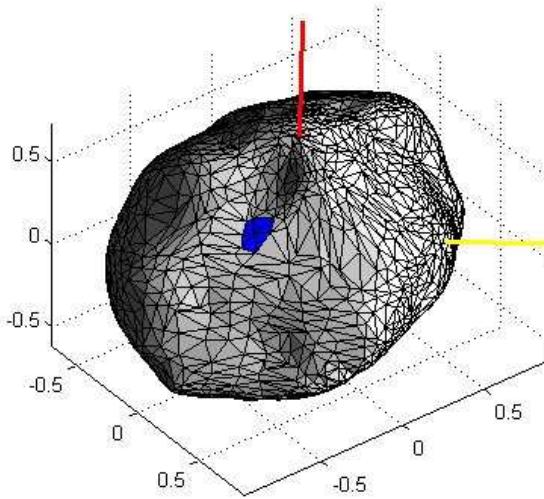
Figure 3.8: 3D shape model of the nucleus of comet 9P/Tempel1, adapted from Thomas et al. (2007) showing the illumination with respect to the geographic features on the surface. The red line represents the spin axis and points towards the positive pole. The yellow line points towards the Sun. The blue pattern is a collection of facets which have been defined as active in the model. Therefore this region will emit dust grains and create a coma structure when we will run the simulation.

inaccurate in case of strong geometric variations of the surface.

Here, we use a different model description. Given the boundaries of the active region (in latitude and longitude) we define whether a facet is active or not. If a facet is labeled as active, it is then filled with point sources according to a density defined by the user of the software. In other words, the active facet is subdivided in a finer grid with dimensions fixed by the user (for instance .5°). The total activity of the region is then distributed among these elementary sources, with the real emission intensity modulated by the illumination. By default the maximum of emission occur at the local solar noon but this value can be changed to account for the thermal lag.

3.2.3.4   Simulation

Given all the parameters defined above, our model calculates the orbital geometry of the system comet-Sun-Earth. It emits particles from the active regions and project their positions into a simulated plane of sky. Particle positions are then converted to intensity through a simple photometric model which considers the luminosity as proportional to the illuminated surface of the grains, seen as perfect spheres. This approach is sufficient as we are mainly interested in the dynamic of the grains, but a more complex one, including Mie theory, needs to be used if we want to simulate the real photometry of the jets. We will discuss in the conclusion chapter of this thesis (Ch.5) how this model can be improved in the next major version of the code.

The simulated image is finally produced according to the observation parameters (size, field of view, resolution) of the ground-based image used as a reference and convolved

with a gaussian ($\sigma = 0.5$") to simulate the point spread function of the imaging optics used for the observations. Figure 3.9 presents some output example of our test simulations which can be compared to the ones from Sekanina (1987) (see Fig.1.13).
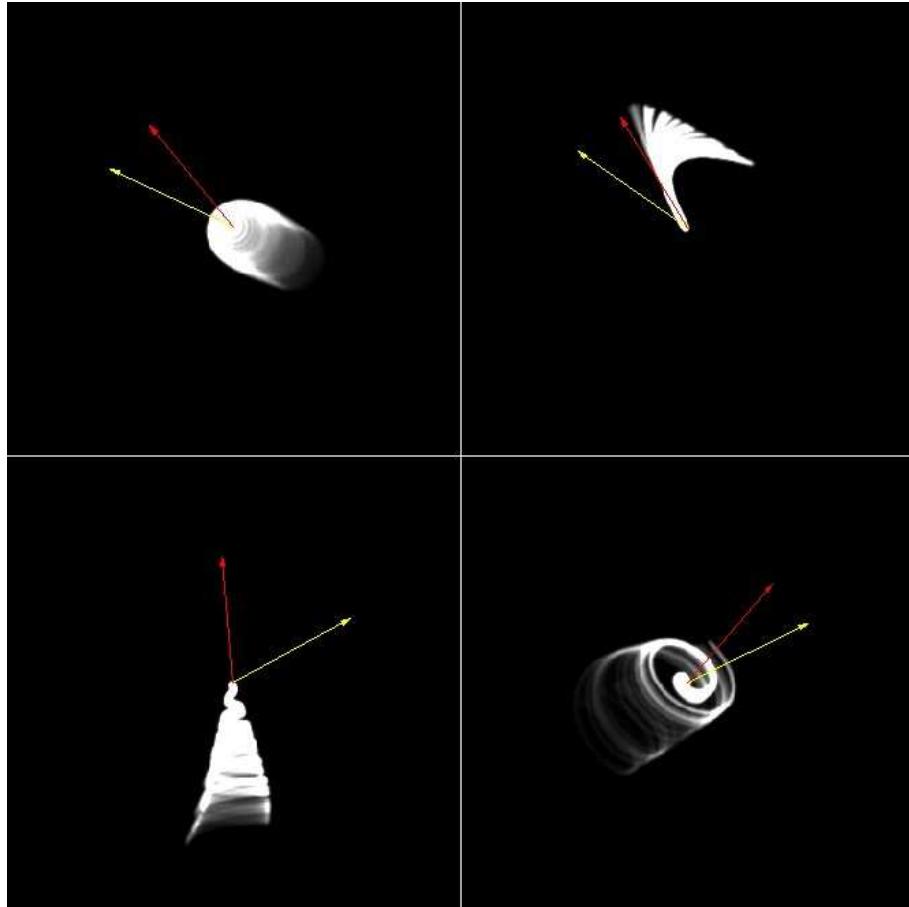
Figure 3.9: Four example of simulations of dust coma structures, showing the variety of patterns one can obtain for different configurations. In all the figures, the yellow line indicates the projected direction of the Sun in the plane of sky, and the red line is the projected position of the spin axis.

3.3   Conclusion and remarks on the numerical model

- This chapter described only the theory of our numerical model. The software itself was implemented in MATLAB, for this programming language provides a good framework when dealing with vectorial data such as orbital positions or 3-dimensional models, without losing too much processing power as it is unfortunately often the case with high-level languages such as MATLAB or IDL. We do plan however to implement some of the routines in a low-level language (likely C or C++) to increase the performances of our code.

  The simulation can be run from a command line but we also implemented a full graphical interface allowing the user to understand better how the simulation works,

and providing a friendlier experience during the trial and error approach. All the details of this GUI and a user manual, are available in Appendix B.

- Although we would like to, our model does not perform a direct inversion from the images to the parameters describing the dust and the active regions. However we achieve this goal by a series of trial and error simulations of the dust jets, given as first input educated guess obtained from or knowledge of the processes involved along with a good understanding of the ground-based observations and the image processing techniques applied.

4 Application to ground-based observations

In the previous chapters, we have discussed the existence and nature of cometary dust coma structures, the methods used to reveal them in the exposures, and a numerical model to simulate them. We will now see how these techniques are combined together and applied to real objects. We will first present a morphological study of the dust coma of comet 73P/Schwassmann-Wachmann along with a determination of its spin axis orientation. In a second part we will show the modeling of dust structures observed in the coma of comet 9P/Tempel 1, and see how well our results compare with in-situ measurements taken by the Deep Impact mission.

4.1 Coma structures in comet 73P/Schwassmann- Wachmann 3, components B and C, between January and May 2006

chapter published as Vincent et al. (2010a)

4.1.1 Introduction

Discovered in 1930, the Jupiter Family comet 73P/Schwassmann-Wachmann 3 (73P) has been widely observed after it broke up in at least five components during its perihelion passage in autumn 1995 (Böhnhardt et al. (1995)). During the 2001 perihelion passage, these components appeared as individual comets and no particular events were found (Böhnhardt et al. (2002), Böhnhardt (2004)). In 2006, the 5.34 years periodic comet came very close to Earth (minimum geocentric distance of 0.079 AU on 12 May for component C, and 0.067 AU on 14 May for component B), just before the perihelion passage in early June 2006. This orbital configuration was a good opportunity to investigate the morphology of the coma of the two main components 73P-B & 73P-C, constrain the rotation axis, and detect new fragmentation events.

We used a sequence of 21 optical broadband images acquired with the CAFOS instrument at the 2.2-m telescope at Calar Alto Observatory (CSIC-MPG) as described in Bertini et al. (2009). These images depict the evolution of the coma between 21 January and 25 May 2006 for component C, and between 8 February and 24 May 2006 for component B. In order to determine whether there were some morphological structures in
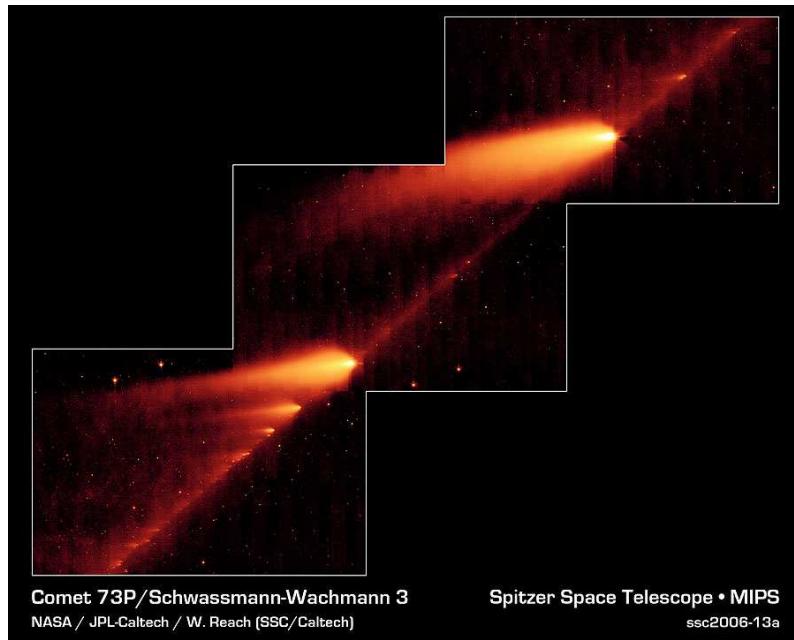
Figure 4.1: Infrared image of some fragments of comet 73P, as seen by NASA's Spitzer Space Telescope, 6 May 2006. Notice that due to the wavelength chosen for the observations, only the dust features (comae, tails, trails) are visible. Credit: NASA/JPL-Caltech/W. Reach (SSC/Caltech)

the comae of the 73P/Schwassmann-Wachmann 3 components, we enhanced calibrated R filter images using two different methods:

1. Adaptive Laplace filtering as described in Boehnhardt and Birkle (1994) and references therein (see Ch.2 for the details of the technique);

2. Radial normalization for verification of the features found through the Laplace filtering. An independent verification of possible coma structures was also done by checking for anisotropies in the isophotes of the calibrated images.

4.1.2   Coma structures of component C

4.1.2.1   Global description

From 21 January to 4 March 2006, component C was active but did not show any specific structure in the coma morphology, except for the dust tail that is always present roughly in antisolar direction. On 4 March (1.57 AU from the Sun), the coma appeared to be elongated in the sunward direction at position angle PA=60° (measured counterclockwise from the North). This structure evolved during the month and on 5 April it turned out to be a fan-like coma pattern (see figure 4.3). Two jet-like features (A and B in figure 4.3) with a typical extension of ~7000 km (projected distance from the nucleus) could be identified at PA=16-53°. In April, the pattern A was continuously present in all our images in PA range 7° to 25°. Contrary to structure A, pattern B showed a variable appearance. On 13 April it appeared to be disconnected from the maximum intensity peak in our image (i.e.

the location of the nucleus) and was not seen in the coma on 16 April, but appeared again with a strong intensity on 26 April. On 8, 9, 10 May, both structures A & B were visible at the same time, with similar characteristics (extension, orientation, curvature). On 10 and 11 May, they faded away; however we could still notice a small elongation of the coma in the direction of the former structures. Pattern A appeared again on 12 May with a very strong intensity, while pattern B showed up only the day after. The two jets remained in the coma until 14 May when they faded away again. On 16 May we could see only a small elongation of the coma in the direction of structure A at PA=45°. Jet A appeared again on 18 May, extending to ~2700 km on 24 May, but it is not present anymore in our last image (25 May). Table 4.1 gives more detailed information about the jets.

In summary, although variable in intensity, feature A is present from the beginning of April 2006 to the end of our observations on late May 2006. The second pattern B cannot be seen on all the exposures; it seems to appear and disappear with a period of about 2-3 days.

4.1.2.2   Interpretation

As the contribution of light from gas and ion emissions is small in the R band, we attribute the observed structures (tail T, patterns A & B) to dust reflected sunlight. Following the approach of Sekanina (1987), we consider patterns A & B as part of a coma fan structure produced by active dust-emitting sources on the rotating nucleus. Considering a single-source on a rotating spherical nucleus, we can interpret the observed pattern as an emission cone viewed side on, with the borderlines forming the straight features A and B in the enhanced images. Therefore, the projected position of the rotation axis falls in between the angle formed by the two patterns and the aperture angle of the fan is directly related to the distance between the source and the pole of the rotating nucleus. Table 4.1 gives the evolution of the mean position angle of the fan formed by the two structure. The rotation axis and the temporal evolution of its projected position on the sky plane as obtained in a simulation of the comet orbit must be compatible with these measurements. Using a trial and error approach, varying the rotation axis systematically over the 4π sphere of the nucleus, we could constrain the orientation of the spin axis. A refined simulation gave the best match between predicted and measured position angle of the projected cone axis for a rotation axis orientation with an inclination of 20-25° to the orbital plane and a longitude of 40-45° at perihelion. Inclination is defined as the angle between the spin axis and the orbital plane (i.e. 90° - obliquity), and zero longitude is along the extended sun-comet vector at perihelion. The best fit of this solution to the measurements (error minimized with a least square method) is presented in figure 4.4. This solution assumes a fixed rotation axis and does not consider precession.

4.1.3   Coma structures of component B

The overall evolution of the coma structure for component B is quite different from the component C one and shows more variability in time and amplitude. There are also clear indications of nucleus fragmentations.

Figure 4.2: Hubble Space Telescope Advanced Camera for Surveys image of Comet 73P/Schwassmann-Wachmann 3 fragment B on 2006 April 18, 19 and 20 showing the motion of small fragments drifting away from the nucleus along the tail direction. Credit: NASA, ESA, H. Weaver (APL/JHU), M. Mutchler and Z. Levay (STScI)

4.1.3.1 Global description

From 8 February to 5 April 2006, the images of component B displayed only an elliptical but featureless coma together with the dust tail. From 11 to 16 April, the coma appeared more and more elongated along the nucleus-tail direction. On 26 April, the isophotes were strongly distorted and the Laplace filtered images showed the presence of several fragments on the tailward side of component B. They remained for several days in the coma and their number increased to at least 6 on 2 May. These fragments were not found anymore in the exposure on 8 May. On 2 May, we also observed the presence of a sunward structure (identified by an A in figure 4.5) which remained visible until 13 May. On 8 May, we noticed the appearance of arclet structures (identified as W1 & W2 in figure 4.5, second row), with orientation roughly perpendicular to the tail direction. The projected extension of these features varied from ~800 km to ~5000 km over a single day (from 8 May morning to 9 May morning). In the next observing night (9 May), the two arclets W1 & W2 appeared to be disconnected from the inner part of the coma (nucleus location). They were not present anymore on 10 May. On 13, 14, and 16 May, we observed again some small fragments in the tail region of component B. We also noticed a very strong increase of activity in the sunward direction. Structure A extends up to 1950 km on 14 May. On 18 May, a second structure (B in figure 4.5, third row) is found in the sunward coma hemisphere at an angle of -45° with respect to pattern A. This feature disappeared (or merged with the other one) in our last image on 24 May. The latter showed also the presence of two fragments, along with the appearance of new arclets (W3 & W4) similar to those observed on 9 May. Tables 4.2, 4.3, & 4.4 give more detailed information about the structures in the coma of 73P-B.

4.1.3.2 Interpretation

In our images of component B we found evidences for several fragmentation events. On 26 April we note a strong deformation of the isophotes along with the presence of a small fragment in the tail direction. As the previous image (taken on 16 April) did not show anything but the dust tail, we believe that a fragmentation event occured in be-

tween these two dates, leading to the creation of the small pieces observed on 26 April and 2 May (see figure 4.5, first row). This interpretation fits with amateur observations reporting a significant outburst on the component B during the early hours of 24 April, which caused a significant increase in the overall brightness until 27 April (see http://kometen.fg-vds.de/koj_2006/73p/73peaus.htm). On 2 May, the brightest of the at least six fragments was only about 300 km (projected distance) from the nucleus and it was almost as bright as the main coma peak of component B. The position of these fragments is given in table 4.4. Evidence of a second fragmentation event comes from the presence of arclets in the images from 8 to 10 May (figure 4.5, second row). As described in Böhnhardt (2004), these arclets are signature of nucleus fragmentation, and should mainly consist of gas. Their occurrence lasted about 2 days and was also recorded by observers at the National Astronomical Observatory (NAO) Rozhen, Bulgaria (Bonev et al. (2008)). Unfortunately, we do not have images close enough in time to the fragmentation event that could illustrate the growth of the arclets. However, as the formation of these wings is mostly driven by gas expansion, with typical velocities of a few hundred meters per second we can assume that the fragmentation event should have occured on 8 May, a few hours before our observation. We note that on our next images (10, 13, 14, 16 May) we did not observe evidence of fragments that might be associated with the event described above: either the pieces were quickly destroyed, or they were too small to be detected.

We also noticed in these images an increase in intensity of the sunward fan, along with a strong distortion of the coma isophotes. On one side it can be due to a more favorable illumination of the active region, but as it happened immediately after the fragmentation event, both phenomena might very well be related. For instance the fragmentation event could have lead to the exposure of fresh material at the surface of the nucleus, thus creating a new active area with increased emission of gas and dust. This scenario is supported by the presence of a second structure on 18 May, seemingly coming from the same region (identified as B in figure 4.5, third row). This pattern could be the signature of a second active source at the surface of the nucleus. In our last exposure of 24 May, only a single structure is visible which might be either feature A or the result of a merging of feature A + feature B in case of two different active regions. As described before, this exposure showed also two arclets that might be signatures of yet an earlier fragmentation event.

As for 73P-C, we tried to constrain the attitude of the rotation axis for component B, using the measured position angles of the sunward coma fan. The results are not as accurate as for component C because this fan is present only in 10 images, covering a time span of 22 days, which implies less geometrical evolution of the projected axis (whereas we could follow the evolution during 3 months for 73P-C). Nevertheless we obtain a best match for the rotation axis with an inclination 5-15° to the orbital plane and a longitude 20-30° at perihelion.

4.1.4   Conclusions

From the analysis of the coma structures in comet 73P before perihelion in 2006, we found that the two main components (C and B) behave differently during most of the time span of our observations:

- As of early April 2006 73P-C shows two jets emanating from the nucleus. Although

variable in intensity, the first one is always present while the second is appearing and disappearing with a period of two to three days. Through Monte Carlo dust coma modeling we inferred that the best possible rotation axis of SW3-C has a low inclination of 20-25° to the orbital plane and a longitude of 40-45° at perihelion (zero in longitude is the Sun-comet extended vector).

- 73P-B displayed a higher variability in terms of activity, showing also several fragmentation events. Its coma is characterized by the continuous presence of a jet roughly in sunward direction, starting from the beginning of May, and by several arclets structures connected to fragmentation events of the nucleus. From the morphological analysis of the coma structures we detect three fragmentation events. The first one happened between April 16 and April 26, leading to the presence of several fragments on May 2. The second can be happened on May 8, the third one before May 24. From the Monte Carlo modeling of the dust we infer a rotation axis of 73P-B with again a low inclination of 5-15° to the orbital plane and a longitude of 20-30° at perihelion.
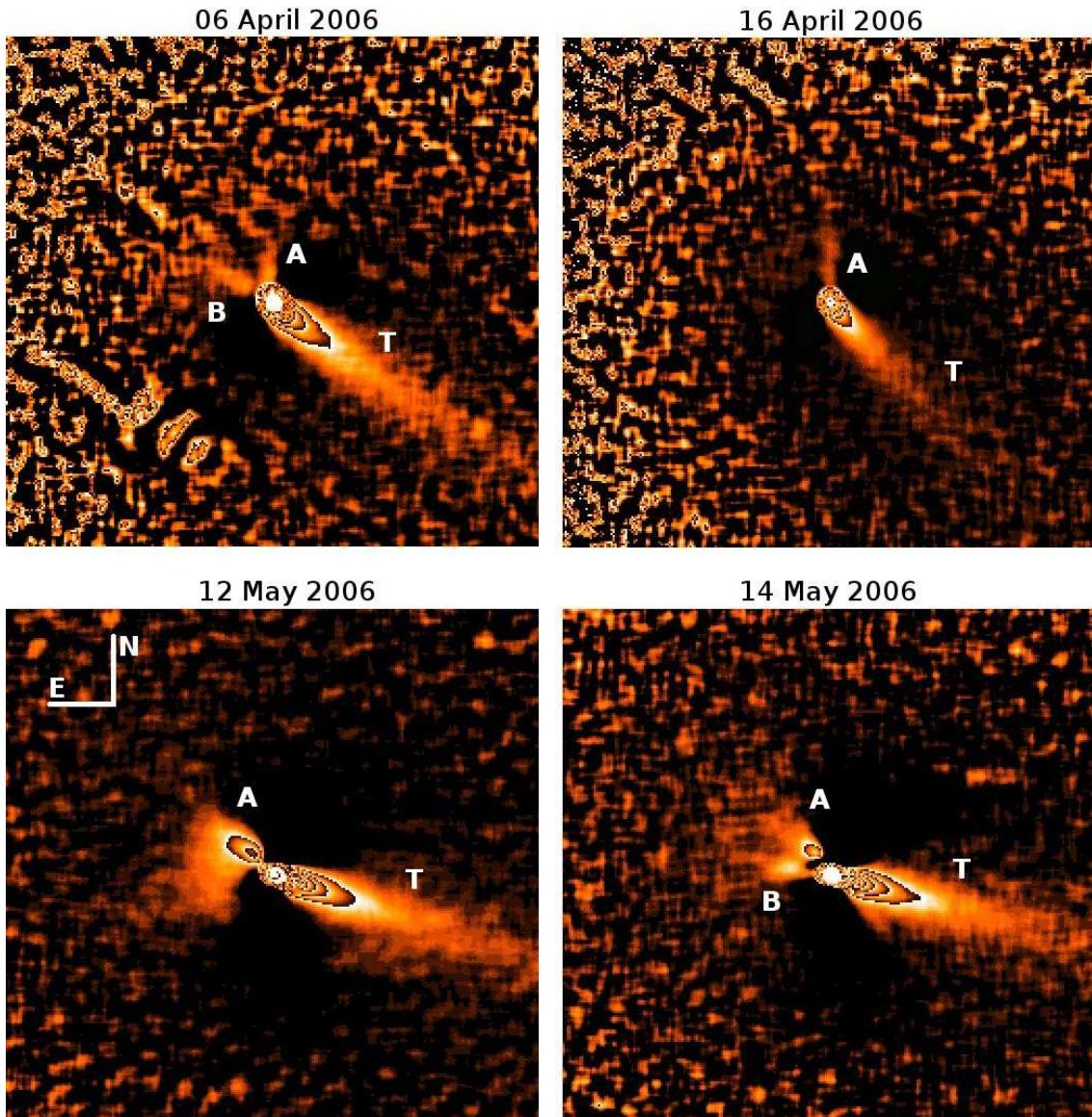
Figure 4.3: Images of comet 73P/Schwassmann-Wachmann 3 component C, enhanced by Laplace filtering, showing the two coma structures (A and B) and the dust tail (T). The observing dates are listed at the top of the four panels. The field of view is 135"×135". The color scale represents the location of a morphological structure and not the brightness intensity as this information is lost during the Laplace filtering.

Table 4.1: Geometry of the Sun and coma structures in 73P-C images.

Date	Sun	Position angle		Extension	
		struct. A	struct. B	struct. A	struct. B
2006-Jan-21.14	107.7	ND	ND	-	-
2006-Feb-07.25	101.6	ND	ND	-	-
2006-Mar-04.07	86.1	60	ND	8700	-
2006-Mar-31.06	55.3	40	ND	4950	-
2006-Apr-05.99	47.7	16	53	6150	5600
2006-Apr-11.12	41.9	22	68	5050	4500
2006-Apr-13.18	39.9	24	66	6950	5350
2006-Apr-16.01	37.5	7	ND	3600	-
2006-Apr-26.06	35.0	25	69	2650	2600
2006-May-02.06	41.2	26	ND	2750	-
2006-May-08.18	57.7	16	65	1350	1350
2006-May-09.17	61.1	35	95	1850	1800
2006-May-10.15	64.3	64	71	500	500
2006-May-11.07	67.2	63	87	1000	1000
2006-May-12.15	70.0	48	ND	1450	-
2006-May-13.17	72.0	33	85	1400	1700
2006-May-14.15	73.3	31	87	1100	950
2006-May-16.15	74.2	45	ND	850	-
2006-May-18.15	73.3	47	ND	1350	-
2006-May-24.17	66.8	65	65	2800	2800
2006-May-25.15	65.8	43	ND	2100	2100

This table gives the near nucleus position angle of the two structures A and B described in the text, together with the position angle of the Sun. Angles are measured counterclockwise from the North in the sky plane of the observer (North=0°, East=90°) and refer to the estimated central lines of the features observed. An uncertainty of about 5° should be considered. The extension of the features projected in the sky is given in kilometers. Abbreviation: ND = Not Detected.
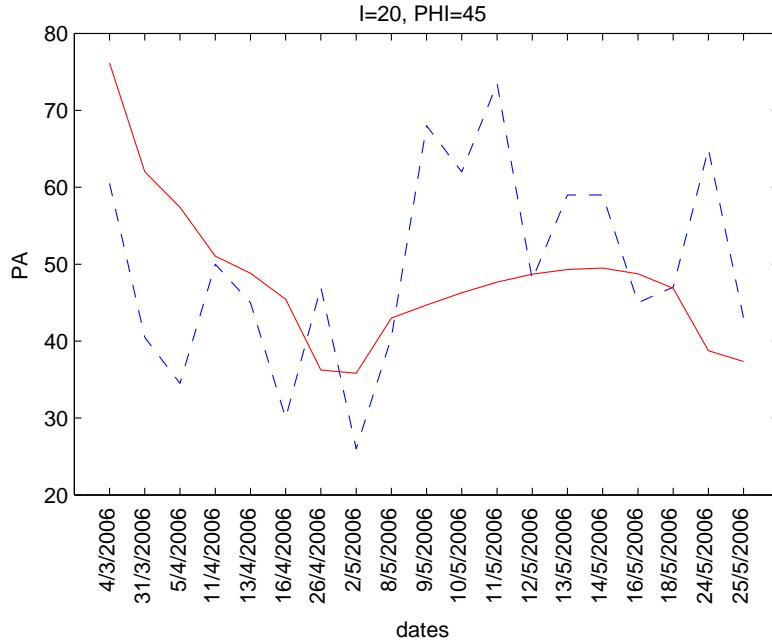
Figure 4.4: Best fit of the position angle of the projected rotation axis position of 73P-C for our observation dates. The dashed line gives the mean position angles of the two structures A & B described in the text. The solid line is the projected position angle of the best fit rotation axis.

Table 4.2: Geometry of the Sun and coma fans in 73P-B images, together with the extension of the structures.

Date	Sun	Position angle		Extension	
		struct. A	struct. B	struct. A	struct. B
2006-May-02.09	29.0	44	-	2000	-
2006-May-08.19	44.4	95	-	2200	-
2006-May-09.18	48.7	65	-	2600	-
2006-May-09.94	52.2	45	-	2500	-
2006-May-10.96	57.2	41	-	1700	-
2006-May-13.01	66.8	48	-	1600	-
2006-May-14.04	70.7	91	-	1950	-
2006-May-16.12	75.4	61	-	2000	-
2006-May-18.14	75.9	92	45	2550	1600
2006-May-24.15	68.2	46	-	1250	-

For an explanation of the table columns, see Table 4.1

Table 4.3: Geometry of the arclets in 73P-B.

Date	Id.	Orientation	Curvature	Extension
2006-May-08.19	W1-E/W1-W	125/315	S/S	500/1000
	W2-E/W2-W	160/270	CC/C	800/800
2006-May-09.19	W1-E/W1-W	125/300	CC/C	2600/4900
	W2-E/W2-W	135/265	CC/C	2300/2600
2006-May-09.94	W1-E/W1-W	161/296	CC/C	3300/3600
	W2-E/W2-W	192/273	CC/C	1550/1950
2006-May-24.15	W3-E/W3-W	180/335	CC/C	1400/1800
	W4-E/W4-W	35/-	CC/-	2450/-

This table gives the near nucleus position angle of coma arclets described in the text. The angles are measured counterclockwise from the North in the sky plane of observer (North=0°, East=90°) An uncertainty of about 5° should be considered. The extension of the features projected in the sky is given in kilometers. Our values differ slightly from the ones measured by Bonev et al. Bonev et al. (2008) which might be due to a better signal to noise ratio in their data set or activity rapidly evolving with time. Arclets identifications are the same as in figure 4.5. The label -E or -W indicates eastern or western wing of the arclet. Abbreviations: S=Straight, C=Clockwise, CC=Counterclockwise.

Table 4.4: Position of the small pieces observed in the tail direction of component B on 26 April and 2 May 2006.

Date	x/y	dist.
2006-April-26.08	-16.2/-23.1	3366
2006-May-02.09	-14.9/-20.9	2271
	-22.4/-22.7	2792
	-24.7/-32.2	3549
	-32.5/-30.1	3880
	-32.9/-59.8	6057

X/Y coordinates (in arcsec) of the small fragments appearing in the tail direction on 26 April and 02 May 2006, as described in the text. Positive X-axis points toward the North and positive Y-axis towards the East. The distance (in km) is the projected distance between each fragment and the central peak of brightness in the coma of 73P-B. Ucertainty on the position is about 0.15" (corresponds to 18 km on 26 April and 13 km on 2 May). It remains unclear if the secondary fragment seen on 26 April is identical to one of the 6 fragments seen on 2 May 2006.
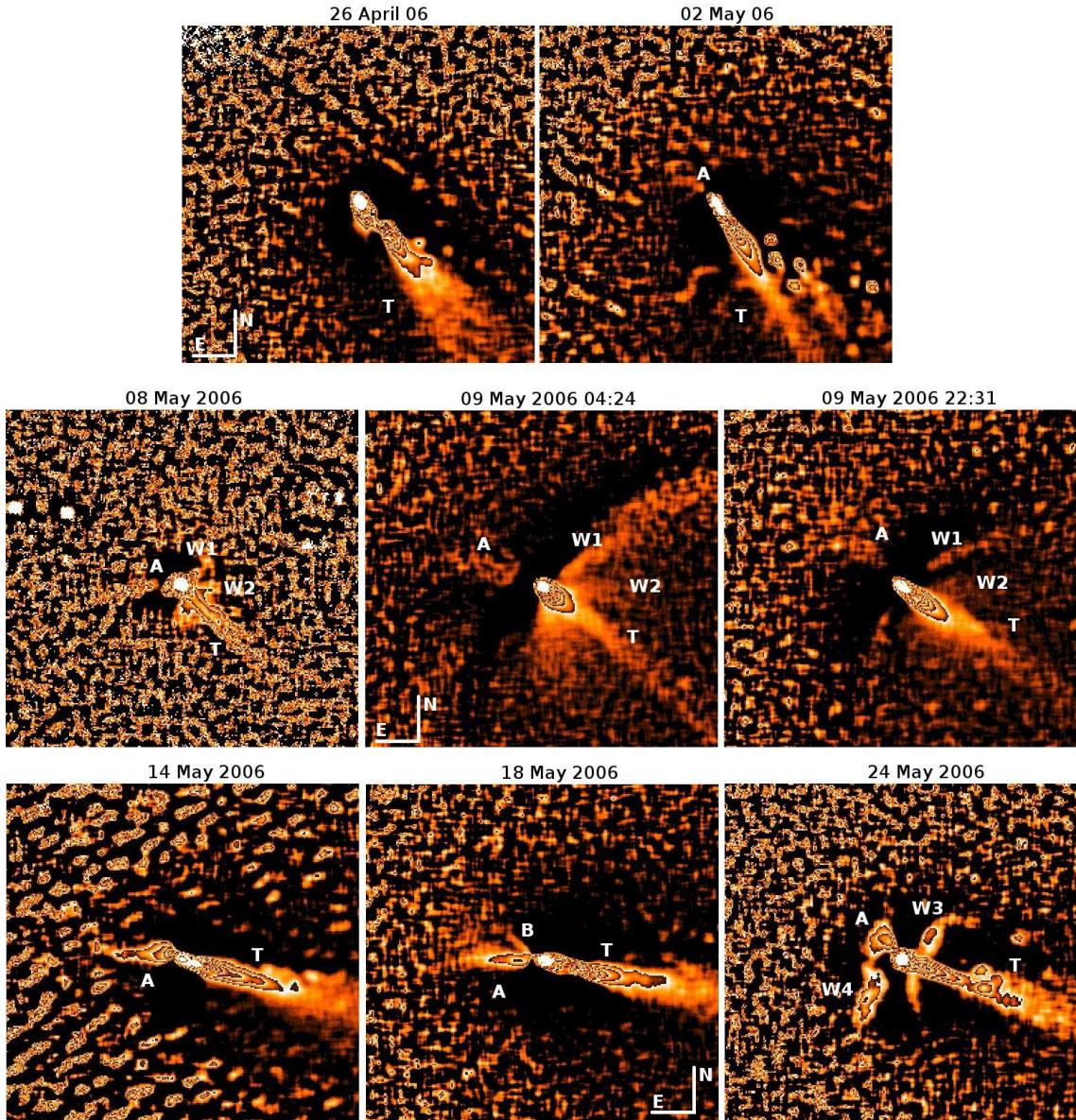
Figure 4.5: Images of comet 73P/Schwassmann-Wachmann 3 component B, enhanced by Laplace filtering, showing various morphological structures. First row displays small fragments in the tail region of the coma. Second row shows arc structures (W1 and W2), a sunward fan (A), and the dust tail (T). Last row shows high variability of the coma structures in the second half of May 2006. Orientation and dates given in the figure, field of view 135"×135".
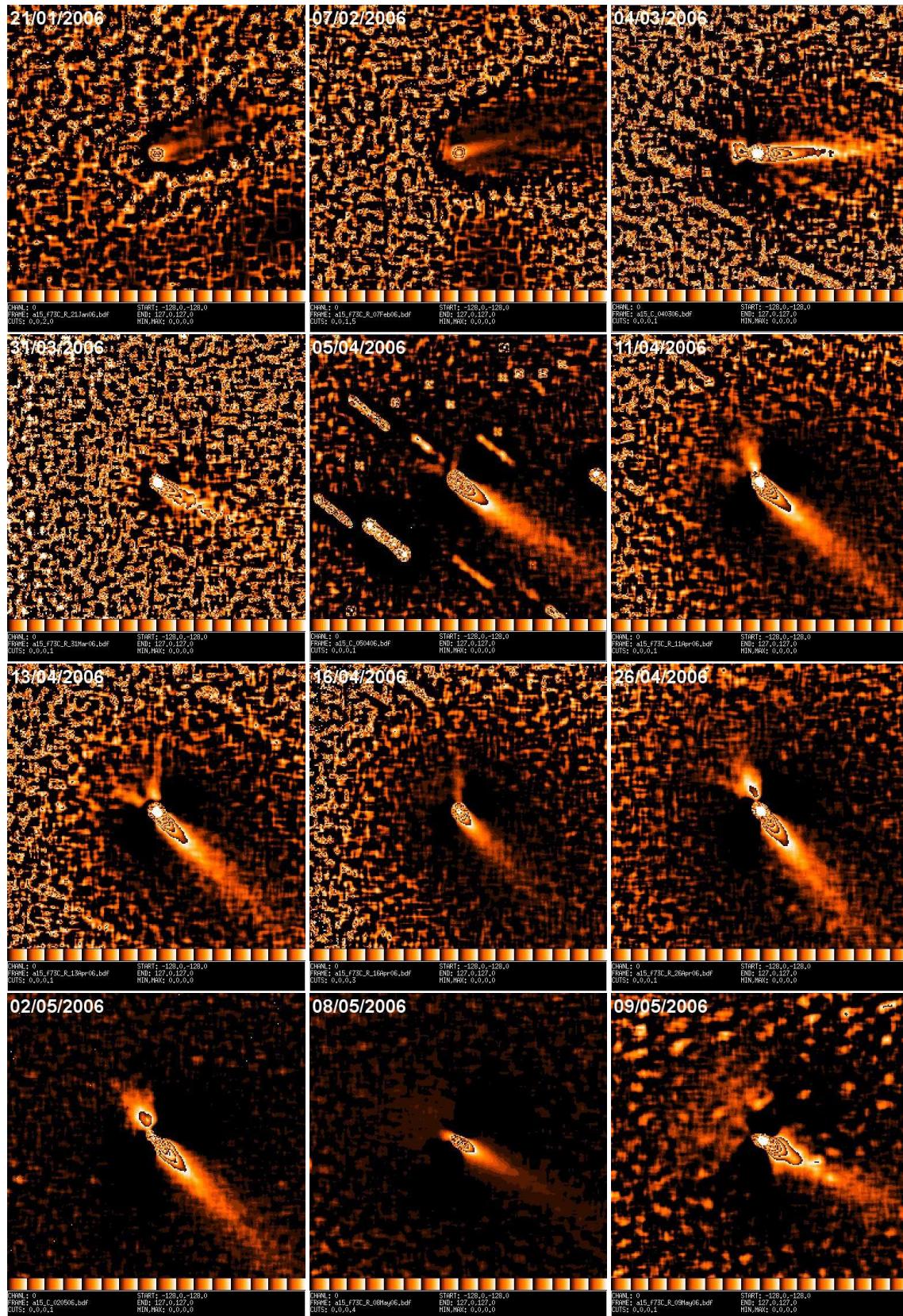
Figure 4.6: Complete series of Laplace filtered images for comet 73P, component C, displaying the morphological evolution of the dust coma from 21/01/2006 to 25/05/06.
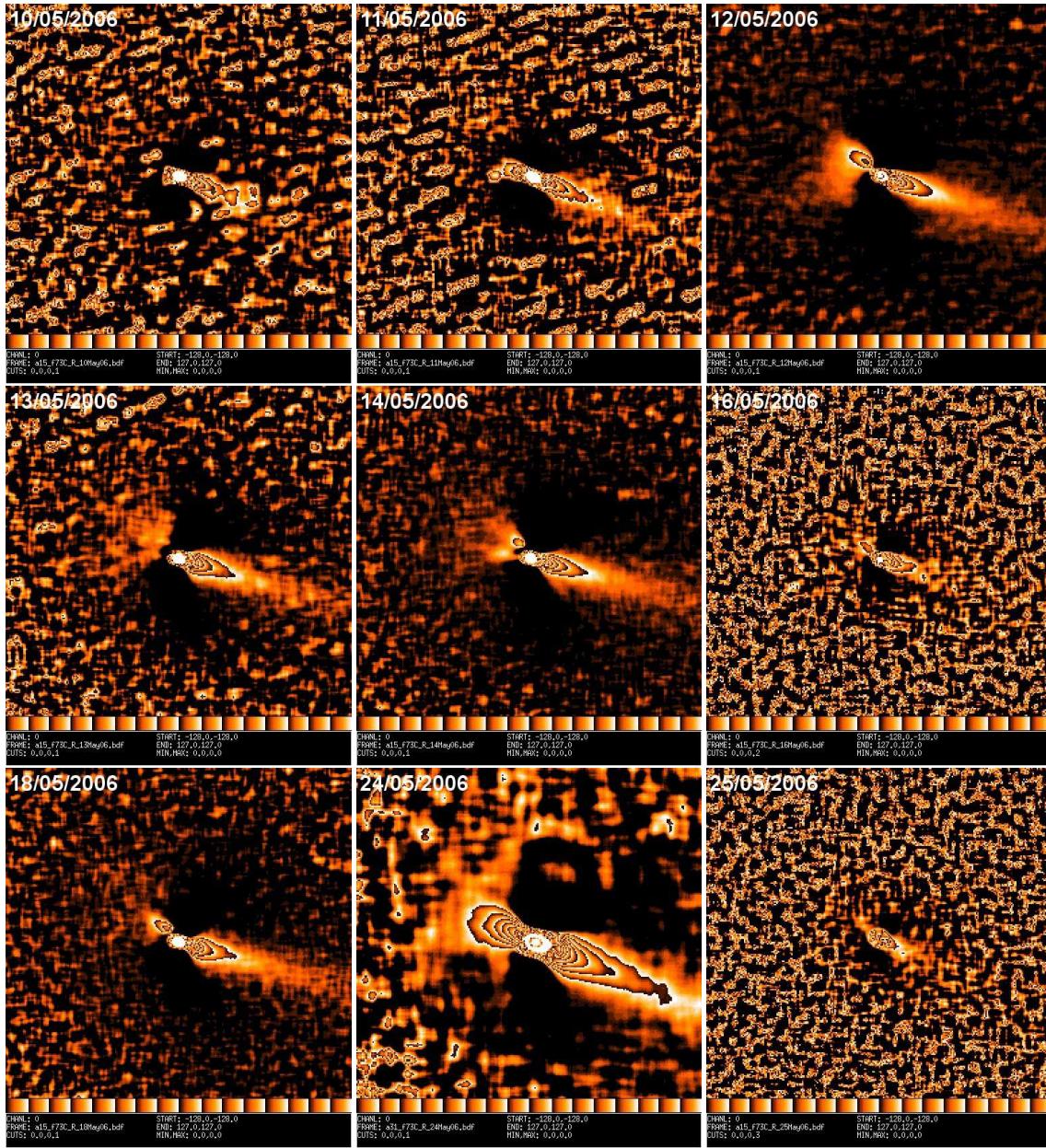
Figure 4.7: Continued from Fig.4.6.
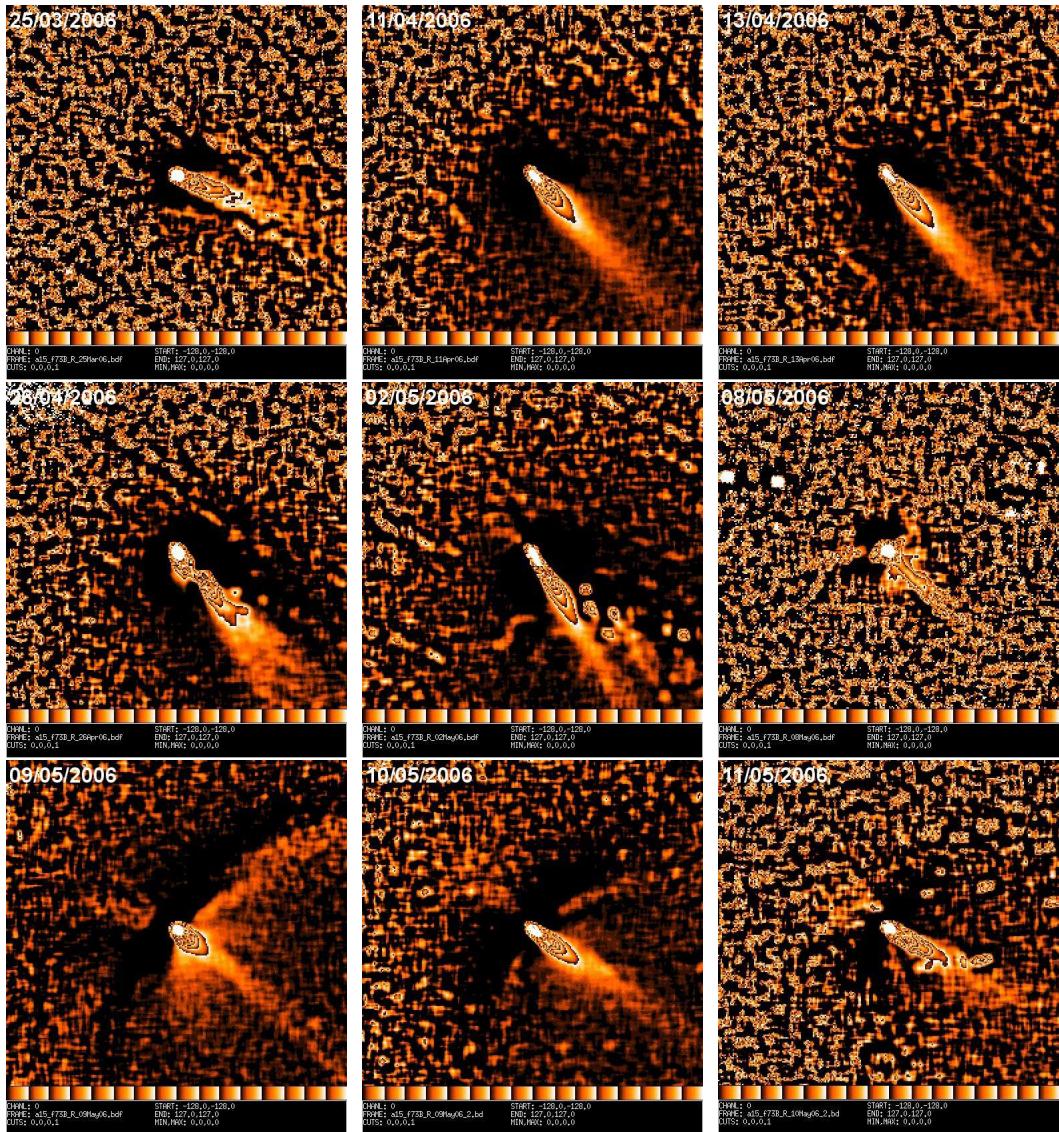
Figure 4.8: Complete series of Laplace filtered images for comet 73P, component B, displaying the morphological evolution of the dust coma from 25/03/2006 to 24/05/2006.
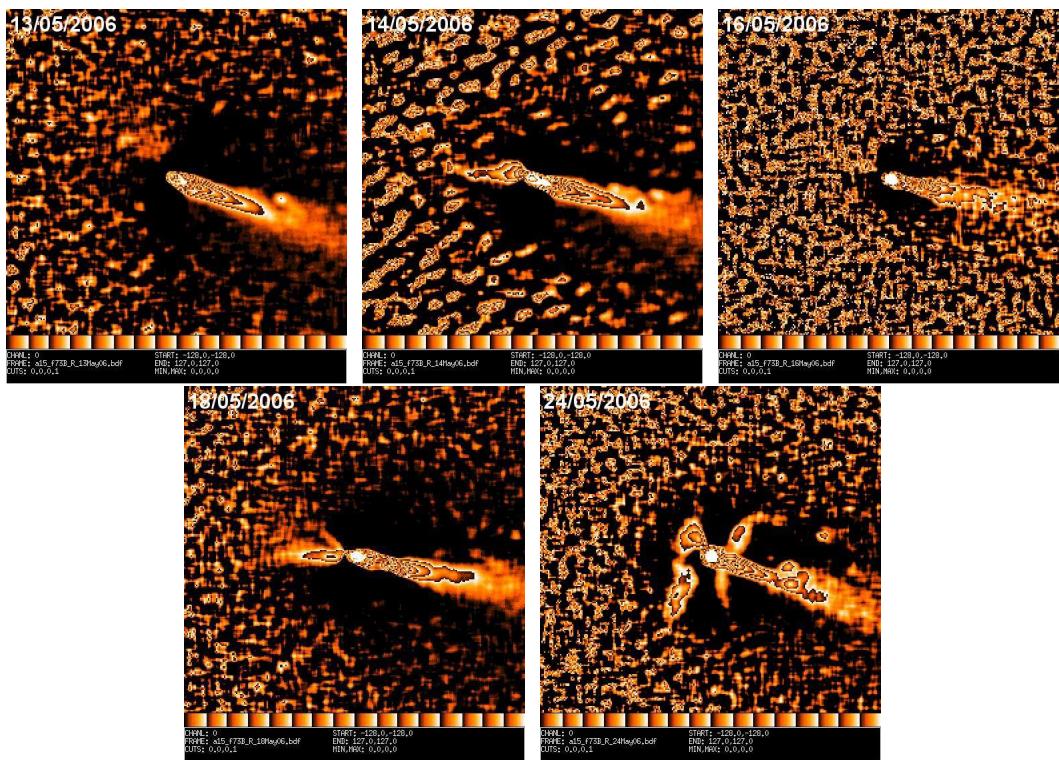
Figure 4.9: Continued from Fig.4.8.

4.2   Testing the numerical model with comet 9P/Tempel 1

chapter published as Vincent et al. (2010b)

4.2.1   Introduction

A natural step after the morphological analysis of the dust coma of 73P-B & 73P-C would have been to attempt a modeling of the structures with the code we had already started to develop. However we decided to focus our efforts on an other comet. The reason is quite simple: even though 73P is a very interesting comet because of its strong activity and the great variety of phenomena going on in the dust coma, nobody has ever tried to model these structures before. Therefore, as our model is also using a new approach, we wanted to test it first on a comet for which we could rely on existing publications to validate our technique.

4.2.2   Application to comet 9P/Tempel 1, pre-impact period

4.2.2.1   Motivation

The motivation behind this work was first to test the model described in chapter 3 and see if our simulation could reproduce and predict ground-based observations of cometary dust comae, and then to compare these results with other techniques, especially information retrieved from in-situ spacecraft measurements. A good test comet for the model required an extended sequence of ground-based observation of dust coma structures, and a shape model of the nucleus as input of the analysis. We also needed to compare the parameters we retrieved for the dust and the active regions with independent published results for the same comet. Six comets had been visited by a space probe in the past, four of them had imaging data returned to Earth. Among them the best choice for our simulation was 9P/Tempel 1 because of the large amount of data available, both ground- and space-based.

This comet had already been heavily studied, mainly because it was the target of the mission Deep Impact. This mission designed by NASA was sent to comet 9P/Tempel 1 in January 2005 with the purpose of crashing a small probe at the surface of the nucleus while a flyby orbiter would observe the impact and analyze the ejecta (see Fig. 4.10 for a summary of the different phases of the approach). The impact occurred on July 4, 2005, producing a very bright cloud of dust and ice observed from the orbiter. During the last phase of the approach, before the contact, the impactor was also imaging the comet and provided very interesting images, revealing a complicated surface with both "old" craterized terrains, and "younger" smooth areas (Fig. 4.11).

Albeit the impact was the main goal of this mission, a lot of science had been done before and after. During the six months preceding the final encounter many teams observed the comet from ground-based stations in order to monitor the activity (for example Lara et al. (2006)), but also directly from the spacecraft as it was getting closer to its target, leading to interesting studies of various topics from the surface temperature (Groussin et al. (2007)) to the shape model of the nucleus (Thomas et al. (2007)). Deep Impact has been so successful from the technological an scientific points of view that the mothership has been retargeted to visit comet 103P/Hartley 2 in October 2010, as part of the EPOXI
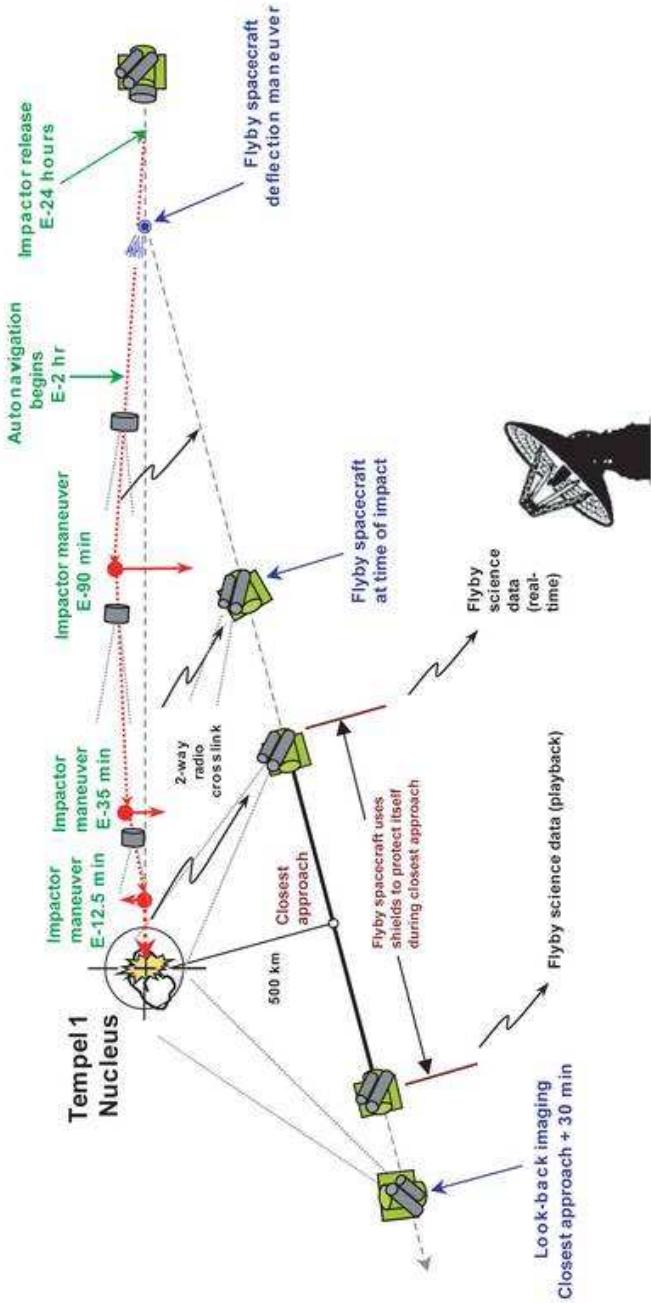
Figure 4.10: Schematic description of the flyby and impact. Source:NASA

mission. As for Deep Impact, this project is also involving an international collaboration of ground-based observers monitoring the comet activity as it approaches its perihelion in order to plan the flyby.

As we wanted to test our model with 9P/Tempel 1, we decided for a "blind" approach, i.e. we did not consider any information published, apart from the required input: ground-based images published and described in detail by Lara et al. (2006), rotation period estimation of 41.85 hours from Belton et al. (2005), and a shape model as published by
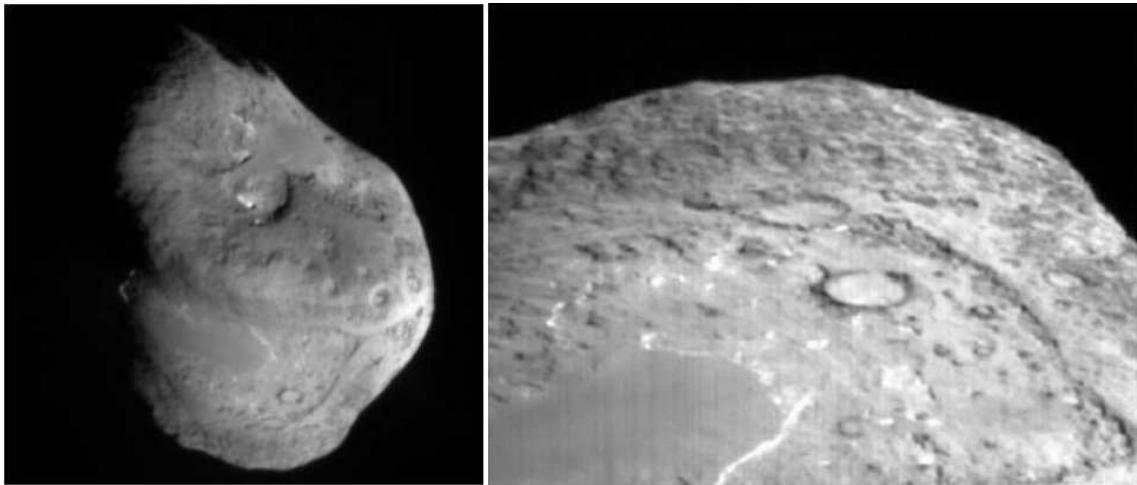
Figure 4.11: Close views of the nucleus surface of 9P/Tempel 1, taken from the impactor during the approach. Notice the variety of terrains, from the rough craterized ones to the smooth regions. Source:NASA
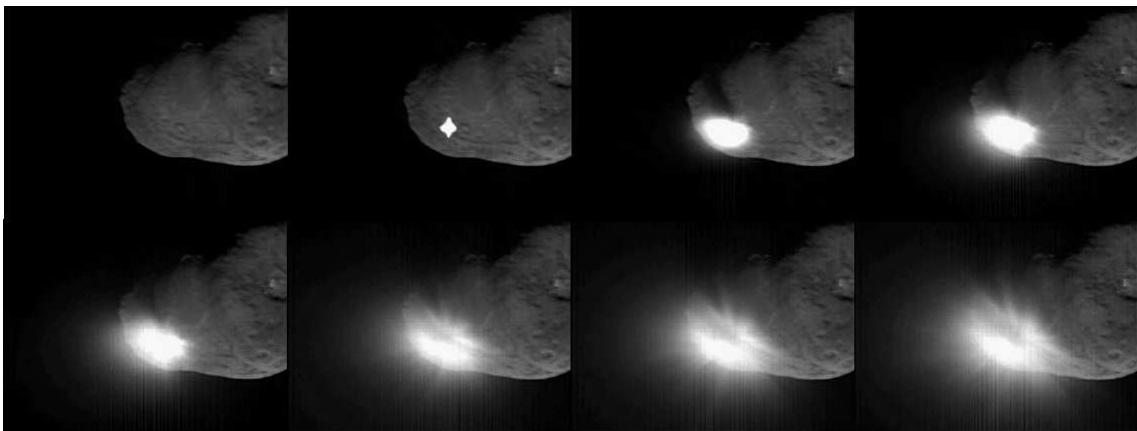
Figure 4.12: Sequence of images showing the impact as seen from the mothership during the flyby. Source:NASA

Thomas et al. (2007).

Information on the rotation axis and on the active regions was not considered, but is used in the discussion of our results.

4.2.2.2   Determination of the spin axis orientation

The first step was to estimate the orientation of the spin axis. We used the technique described by Sekanina (1987) which we had already applied to determine the spin axis of comet 73P/Schwassmann-Wachmann 3, components B & C (chapter 4.1.1 and Vincent et al. (2010a)). To summarize the process: Given images of dust coma structures, we consider the observed patterns as produced by active dust-emitting sources on a rotating nucleus. Single sources create emission cones but when we observe them side-on, we detect only the borderlines of these cones, which form straight features in the enhanced images (see Fig. 4.13 for example). Following this approach, the projected position of

the rotation axis falls in between the borders of the fans. We first estimate this position from our set of observations. Then, using a trial and error approach varying the rotation axis systematically over the 4π sphere of the nucleus, we determine the orientation of the spin axis as the one which provides the best fit to the estimated projected orientation for all observing epochs. Our simulation led us to conclude about a spin model given by a right ascension (RA) of 293° and a declination (DEC) of 73° with ±5° of uncertainty. This value is in very good agreement with the one retrieved by the Deep Impact team (RA=294° and DEC=73°, ±5°) from the flyby images, see Thomas et al. (2007).

4.2.2.3   Modeling of the pre-perihelion activity

With the spin axis orientation determined, we ran our model to find which parameters for the dust grains and the active regions would allow us to reproduce the activity as observed by Lara et al. (2006) between January and June 2005. An example of our results is shown Fig. 4.13. This figure shows two different observations of comet 9P/Tempel1, 14 May 2005 and 5 June 2005, processed with an adaptive Laplace filter, and the result of our simulation. The images display several patterns labeled with capital letters in alphabetical order, starting from North and turning in an anti-clockwise direction. We kept the same labels of the structures as in the paper already published by Lara et al. Notice that the structure labeled B in our images is identified as dust tail signature and was thus not included in our simulations using the dust emission model. Patterns D & E were identified as borderlines of a cone produced by the same active region. Patterns A, F, G, H belong to separate areas on the surface.

In order to reproduce the observed features, the model requires several active regions (labeled AR1,2,... in the text) with well constrained parameters.

The most active area (AR1) is located on the southern hemisphere, at latitude −65° ± 15° and longitude 300° ± 30°. The region should be extended and shows strong activity, emitting millimeter-sized particles with a terminal velocity of 12 to 15 $m.s^{-1}$. The activity is constant over the rotation cycle, with no noticeable variation of intensity between day and night. From the orbital elements and the determination of the spin axis, we can estimate that the subsolar position at that time remained around latitude +15°, which means that the southern hemisphere of the nucleus was spending about 20 hours in the night during each rotation. Hence the activity must be driven by sublimation of a supervolatile ice that does not require instantaneous illumination to evaporate. In that respect CO_2 ice might be a good candidate. This scenario is enforced by the results from Feaga et al. (2007) showing a strong assymetry between H_2O and CO_2 in the coma of 9P/Tempel 1, with the CO_2 pattern matching the dust morphology more than H_2O (the latter being concentrated in the sunward direction). This active region creates structures D & E in Fig. 4.13.

The second area of the nucleus we identified as a possible source for the dust jets is located in the equatorial region. The orientation of the jets suggests that the activity is confined to the day side of the nucleus. The structures produced at this latitude (F, G, & H) are oriented in sunward direction and they are straight or slightly curved towards the tail direction. This indicates a low sensitivity of the dust to the radiation pressure. Our simulation reproduced these jest with particles similar to the ones observed in the southern fan (100 μm to mm size particles with low velocity), thus confirming the initial

conclusion. Using the shape model, we were able to estimate the coordinates of the active regions corresponding to structures F,G. & H. The latitude of -10° ±5° is very well constrained due to the favorable geometry of the observation (nucleus seen almost side-on). Using the 3D shape model, we could also infer the longitude of these sources. Although the uncertainty is much larger than for the latitude, we estimate the following positions:

- region AR2: latitude -10°, longitude 0°, creating jet F.

- region AR3: latitude -10°, longitude 90°, creating jet G.

- region AR4: latitude +5°, longitude 90°, creating jet H.

These regions are active only during the day.

The last area of activity identified (AR5) is close to the north pole of the nucleus and is responsible for structure A in Fig. 4.13. The strong counterclockwise curvature of the jet, with respect to the other ones, implies smaller particles, more sensitive to the β parameter. We estimated grain sizes smaller than $10\mu m$ and emission velocities around $30\ m.s^{-1}$. From the images in Lara et al. (2006) it is not possible to conclude about the diurnal profile of activity for this region.

4.2.2.4 Comparison with existing results

After conducting this simulation, we compared our results with the one already published by the Deep Impact team (Farnham et al. 2007), as obtained from the fly-by images of the spacecraft. We found a very good agreement for all the retrieved parameters, in particular similar values for the dust size and velocity, and for the position of the active regions. Farnham mentioned the existence of a jet originating at +40° of latitude, and observed during the approach phase of the Deep Impact mission. This jet does not appear in the ground-based images of the pre-impact period, probably due to a lower signal-to-noise (S/N) ratio. The same paper infers also a possible night side activity at the north pole; we could not confirm this with our set of images from the pre-perihelion period but it cannot be excluded either.

4.2.3 Application to post impact images

4.2.3.1 Data acquisition and processing

After successfully retrieving in formation on the various active regions of comet 9P/Tempel l, from the pre-impact period, we applied our model to predict the evolution of these structures in the post-perihelion period. The data used for this study consists of broadband images, acquired in the European Southern Observatory of La Silla (Chile). The exposures were taken in service mode from 17 July to 12 August 2005 with the Wild Field Imager (WFI) on the $2.2m$ MPG/ESO telescope. This instrument is a half degree camera for the visible wavelength range (see `http://www.eso.org/sci/facilities/lasilla/instruments/wfi/` for details). In order not to smear image details due to the motion of the comet, and to avoid saturation of the central coma part,
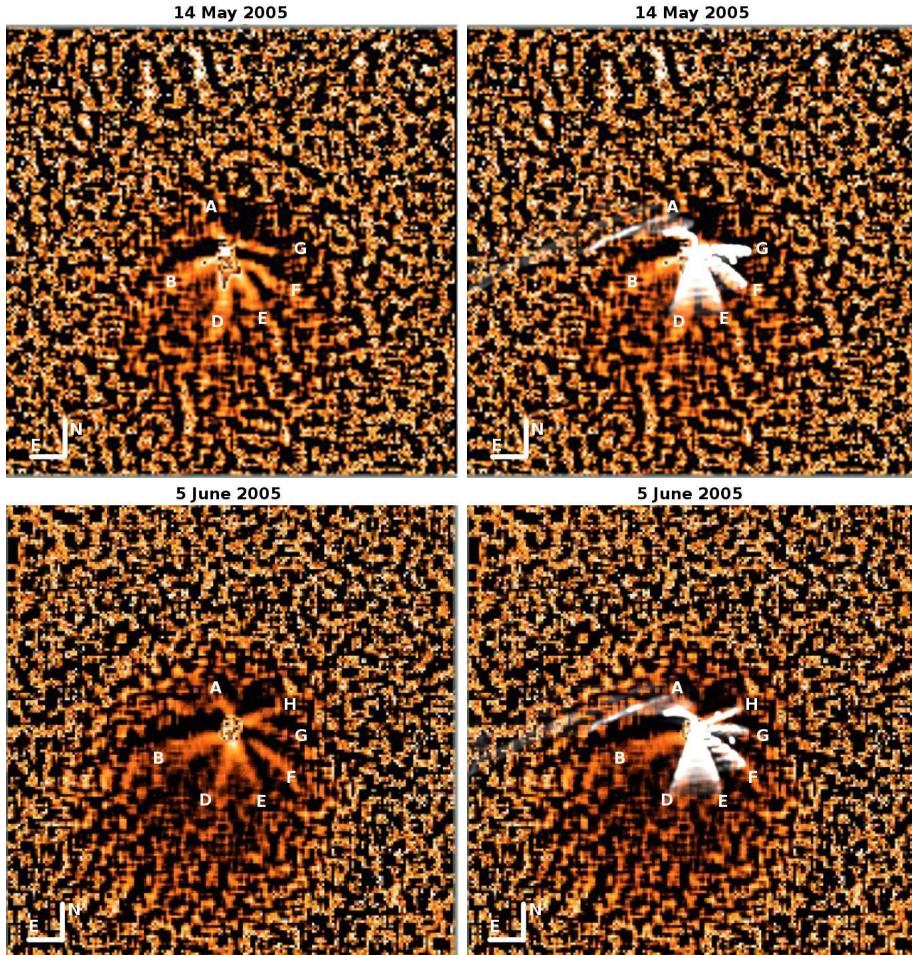
Figure 4.13: Images of the coma structures of comet 9P/Tempel 1 for two different days from Lara et al. (2006). The left panels show Laplace filtered images of the coma, where the filter enhances shortscale brightness features while removing longscales variations. The random irregular pattern seen in the background is due to the noise structure in the original image. The labels identify the coma structures as described in the text. The orientation is given in the lower left of the images. Field of view is 2.25×2.25 arcmin which corresponds to 75000×75000 *km* at the distance of the comet. The right panels show the simulated structures overlayed on top of the images, showing the good agreement between the modeling and the observations. Notice that structure B was identified as the dust tail signature and is therefore not included in our simulation.

Table 4.5: Observations Logs

Date	r (AU)	Δ (AU)	PsAng(°)	A(°)	B(°)	D(°)	E(°)	F(°)	G(°)	I(°)
19/07/05	1.512	0.979	109	40	110	180	225	ND	285	330
26/07/05	1.520	1.024	108	45	108	185	225	250	285	330
02/08/05	1.532	1.073	107	55	108	175	210	ND	285	335
08/08/05	1.544	1.119	106	45	105	185	230	260	285	335

Identification of the coma structures as shown in Fig. 4.14 and Fig. 4.15. The given position angles refer to the center lines of the structures and may have an uncertainty of maximum ±10°. North=0°, East=+90°. PsAng is the position of the extended Sun-Comet vector. ND = not detected.

exposure series of $\simeq$ 200s integration time for the individual images were applied. Exposures were reduced with bias and flat field removal, sky subtraction, and flux calibration in photometric nights. The final images are median combined using the short exposures of an observing night, in order to improve the S/N ratio and to remove the background stars.

In the reduced images, it is usually not possible to distinguish dust structures, apart from the tail, because of their low intensity with respect to the coma background. Different enhancing techniques can be used to display inherent features. We applied two independent methods: (1) adaptive Laplace filtering as described in Boehnhardt and Birkle (1994) and references therein, and (2) Larson-Sekanina filtering (Larson and Sekanina 1984). The first filter applies a Laplacian kernel to a logarithmized image, removing all the gradual variations (linear and second order gradients) while keeping the fine variations of different scale depending on the width of the numerical filter. The second technique is a direct subtraction between the original image and a rotated/shifted version of it.

4.2.3.2   Morphology

Figure 4.14 presents images from the post-impact data set. As the morphology of the dust coma was mainly constant during the whole observation period, we describe only selected images representative for the whole data set (see Fig. 4.14 and table 4.5). From the Laplace filtered images we can clearly recognize features observed during the pre-impact period like the dust tail (B), two equatorial jets (F, G), and the north pole structure (A). The equatorial jet H is not detected in any of our images. The southern fan does not appear with this processing but is observed with the other enhancement technique. For example the comparison with the Larson-Sekanina filter is shown Fig. 4.15. It appears much weaker in August 2005 than before perihelion but we cannot conclude whether this is due to a poor S/N ratio of the original images or a real decrease in intensity. We notice however a strong curvature of this fan (jets D & E) in the anti-sunward direction. We detected a new structure (labeled I in Fig. 4.14) at a position angle of $\simeq$340° that is present in all post impact images and that was not seen in the Lara et al. data set.
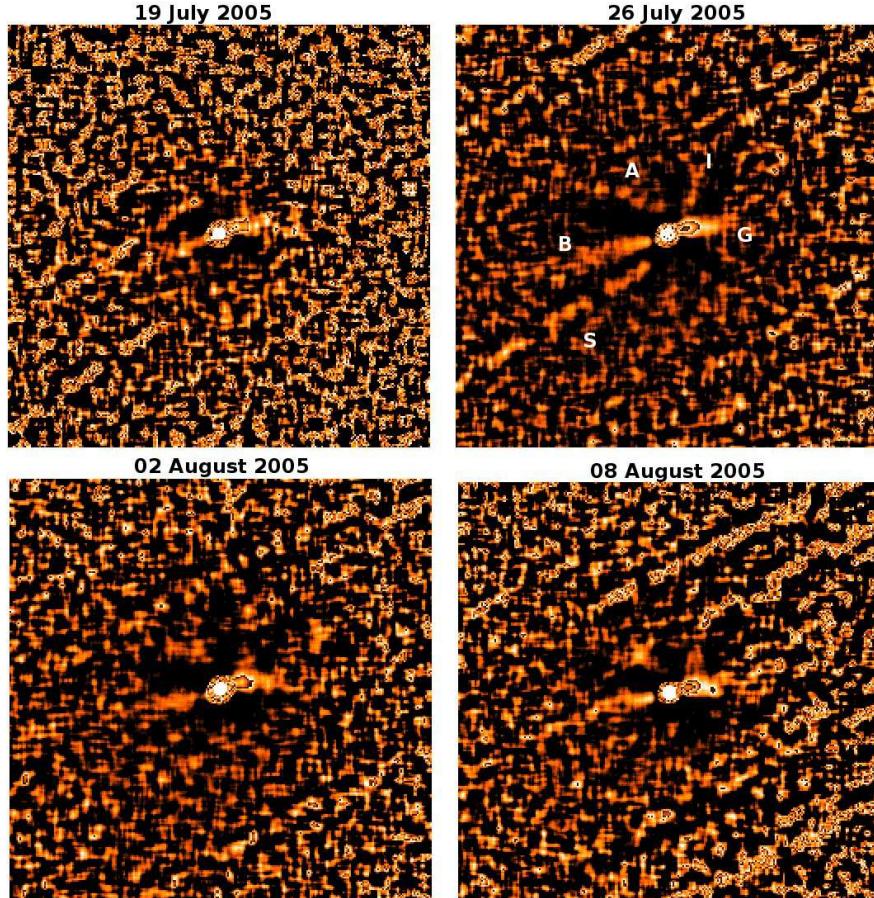
Figure 4.14: Laplace filtered images showing the evolution of the dust coma structures of 9P/Tempel 1 in the post impact period. The morphology is fairly constant, and one can identify some of the structures observed in the pre-impact period as for instance the northern jet (A), the dust tail (B), and the equatorial activity (G). The southern fan does not appear clearly in these images. The feature labeled (S) on 26 July 2005 is a background star passing through the field of view. We observed a new jet (I) which was not detected in the pre-impact observations. Field of view 1×1 arcmin (43000×43000 *km* at the comet), orientation as in Fig. 4.13. Details on the geometry of the structures are given in Table 4.5.
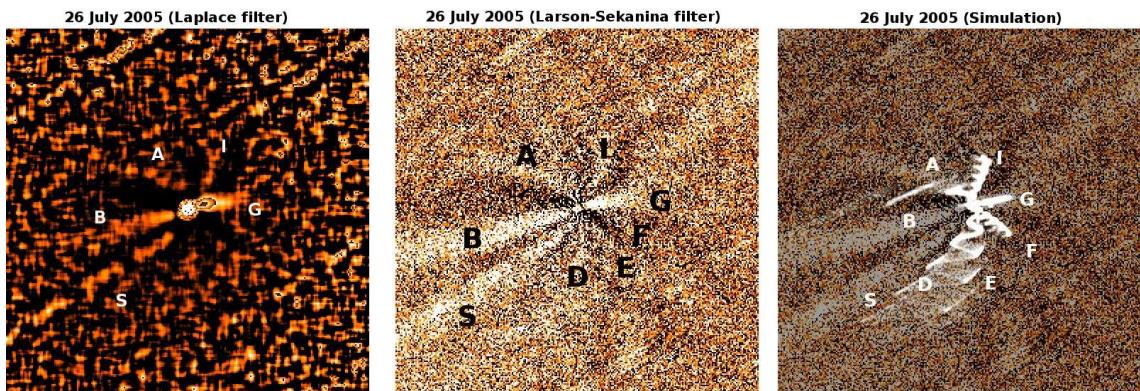
Figure 4.15: Comparison between the Laplace filtered image (left) and the Larson-Sekanina filtered one (middle). More structures are detected in the latter. The right image shows an overlay of our simulation on top of the Larson-Sekanina processed image. Again we find a good agreement between our model and the observation of the geometric patterns of the dust features.

4.2.3.3   Simulation results

We applied our simulation model to this new set of images, keeping the parameters for the description of the active regions as determined from the pre-impact images. The simulated pictures match well the observations for the equatorial part (structures F & G), and our simulation reproduces the respective features created by regions AR2 and AR3 without changing any parameter.

The situation is different for the southern fan (structures D & E). Keeping the same parameters as before we reproduce the orientation of the fan but not the curvature. In order to match the latter in the images, we need to introduce smaller particles in our model (10 to 100 μm). As said before, the southern fan is more difficult to detect in our images, and this was first interpreted as a lower S/N. However, the simulation shows that we have smaller particles, which can also indicate a decrease of activity in region AR1. The geometrical conditions for the illumination of this region are almost the same as during the pre-impact phase, which makes an explanation of this change of activity by a sudden change of illumination of the southern hemisphere unlikely.

The northern jet originating from region AR5 looks also similar to the one observed in June 2005. However, in order to fully reproduce the observed feature, we need to change the diurnal profile of activity and allow the region to emit particles during the night. This is coherent with the results from Farnham et al. (2007) which we were not able to confirm from the pre-impact images alone.

The jet at a position angle of +340° (labeled I) could be reproduced easily by an active region AR6 at +45° of latitude, emitting millimeter size particles with low velocity (12 $m.s^{-1}$) during day time. This structure could relate to the jet observed by the Deep Impact team already during the pre-impact phase, but not seen in the images from Lara et al. (2006). Our model could not constrain the longitude for this region, but images of the surface show a smooth patch in the northern hemisphere around latitude 45° and longitude 270° similar to the one observed in the southern hemisphere. It is not clear if those patches are the source of activity, or a product of it (*i.e.* a redeposit of material lifted

by the sublimation) but the southern fan is clearly connected to the observed activity in this hemisphere (region AR1) and it might be similar for the northern patch.

4.2.4 Conclusions

The model, albeit simple, allows us to retrieve important parameters on active regions of comet 9P/Tempel 1, summarized here.

1. Spin axis orientation determined from the ground-based observation: RA = 293° and a DEC = 73° (±5°), unchanged between January and August 2005 and in good agreement with flyby imaging results.

2. Identification of 6 active regions on the nucleus:

    (a) a southern region AR1 at −65° ± 15° latitude and 300° ± 30° longitude, close to a smooth area on the nucleus. Its activity does not change with day/night time, indicating a different material than H_2O for the sublimation. This region gives rise which gives rise to the fan (D,E) in the observed images.

    (b) 3 strong equatorial regions are identified in the pre-perihelion period emitting millimeter size particles at low velocity ($\simeq 12m.s^{-1}$) during day time. These areas are located at the following coordinates (latitude, longitude): AR2(-10°, 0°), AR3(-10°,90°), AR4(0°,90°). The latitude values have an uncertainty of ±5°, longitudes are only roughly estimated. They are responsible for the jets (F, G, H) in the pre-perihelion exposures.

    (c) a region close to the north pole (AR5), emitting particles smaller than 10 μm, also active during night time. This area produces the jet (A).

    (d) an active region in the northern hemisphere (AR6) located at latitude $\simeq$ +45°, creating the jet (I) in the post-impact images.

    The connection between active regions and jets is summarized in table 4.6.

3. In comparison with the pre-impact observations, we noticed a decrease of activity in the southern hemisphere, which can not be explained by a difference in illumination, the conditions being fairly the same.

Using this model one can retrieve information at different scales: physical properties of the dust (grain size, terminal velocity, β ratio), and localization of the active regions at the surface, along with good constrains on the diurnal activity profile. As stated before, the results obtained here depend strongly on the quality of the shape model, because we assume an ejection of dust mainly normal to the surface. This assumption is realistic for 9P/Tempel 1: it has been observed from the spacecraft, and when included in the modeling of ground based observations, this assumption leads to good results. However it might not be true for other comets and has to be considered carefully. The same simulations done with a spherical nucleus would lead to similar results for the dust properties but would provide wrong initial direction of emission and thus prevent us to localize precisely the active regions. Therefore, this model should always be used with a realistic estimation of the shape of the comet one wants to study.

Table 4.6: Local coordinates of the active regions and associated jets

Active region	Latitude(°)	Longitude(°)	Associated jet(s)
AR1	-65	300	D,E
AR2	-10	0	F
AR3	-10	90	G
AR4	0	90	H
AR5	80	0	A
AR6	45	270	F

Summary of the localization of the active regions at the surface of the nucleus, and associated jets. Coordinates are given with an uncertainty of $\pm 10°$.

Our results obtained from modelization of ground-based observations agree well with those from in-situ measurement and the model is able to make realistic predictions for the evolution of the structures. This can be of interest in the planning of future missions like Rosetta for which any information on the position of active regions must be known long enough in advance in order to adjust the trajectory of the probe and avoid any hazard. An other outlook of this study would be to combine this simulations with a good photometric model of the coma in order to estimate not only the dynamical parameters of the dust but also the flux and photometry of the jets.
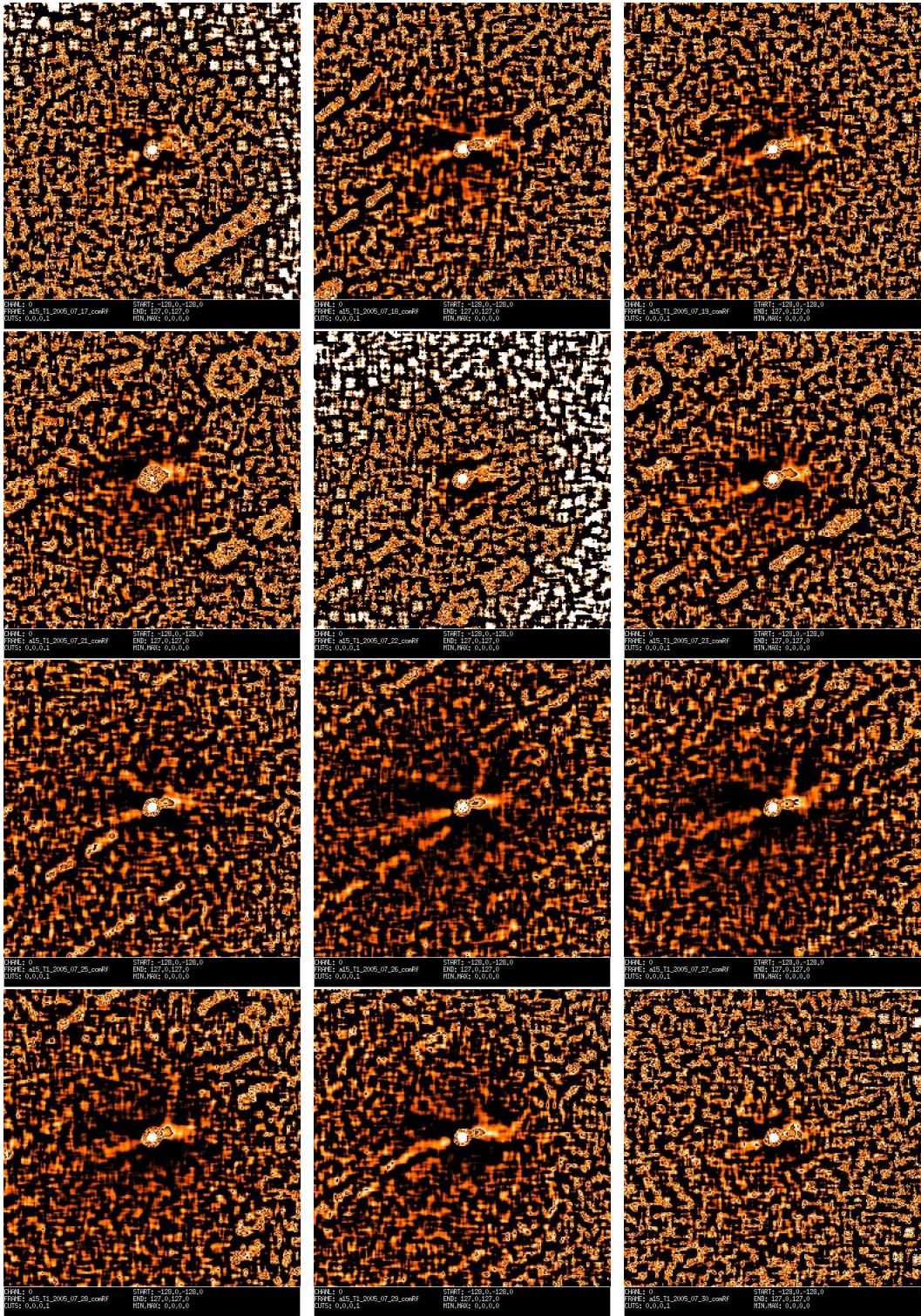
Figure 4.16: Complete series of Laplace filtered images for comet 9P/Tempel1, displaying the morphological evolution of the dust coma in July and August 2006. Images are displayed following a chronological order with one image per day from July 17 to August 11, except July 20 and 24 as no observations were recorded on these two days.
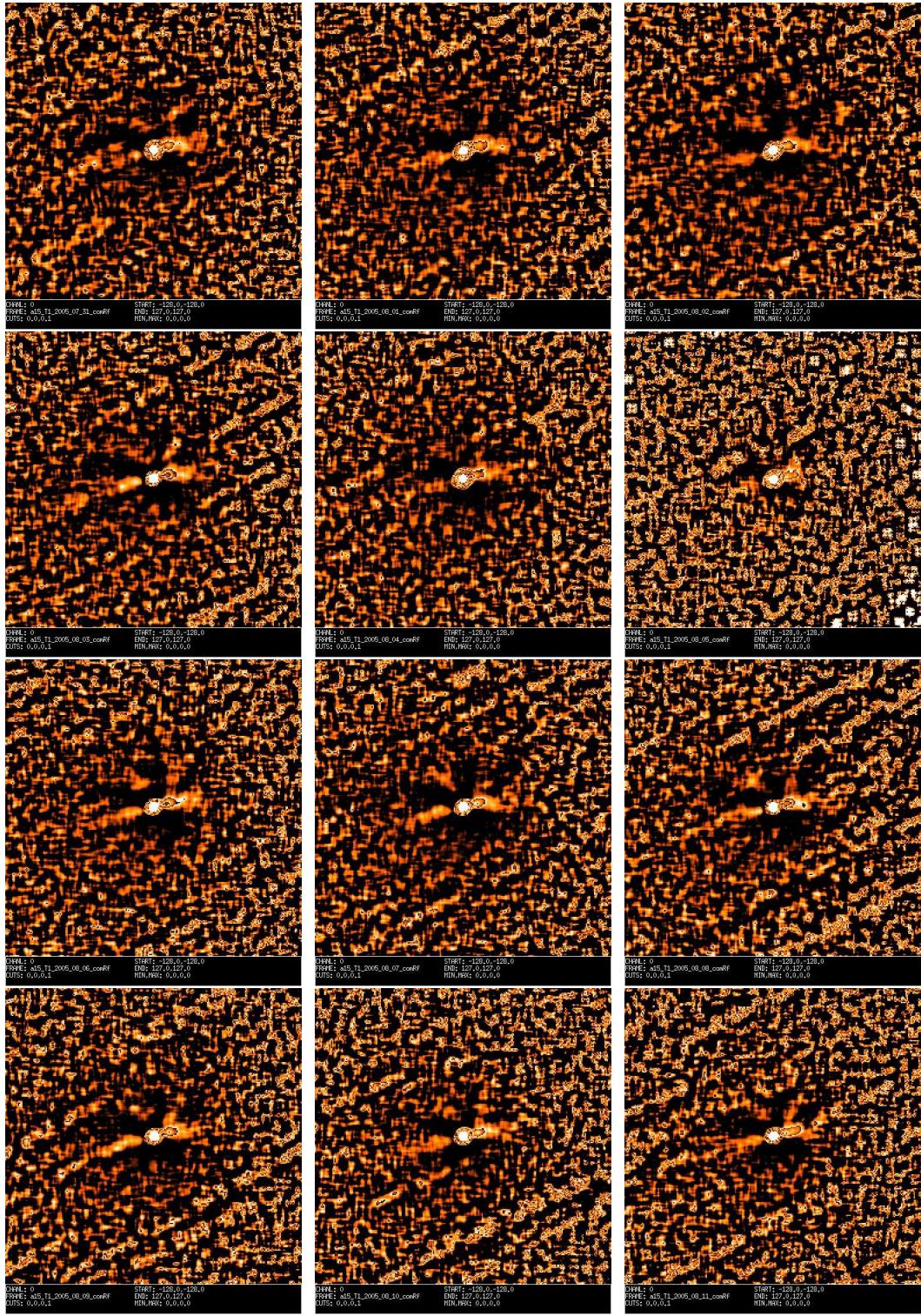
Figure 4.17: Continued from Fig.4.8.

5 Discussion and outlook

5.1 Main results

Now that we reach the end of this thesis, it is time to look at what has been achieved and see how this work can be integrated to the general field of cometary research.

We can summarize this study with the three following contributions:

1. revealing coma structures in ground-based observations through advanced image processing techniques,

2. developing a new model of the structures using realistic assumptions on the shape of the nucleus,

3. apply this generic model to real cases to infer important properties of different nuclei.

We will discuss now these three points, insisting on what has been done, but also on the difficulties we have encountered and how things could be improved.

5.1.1 Image processing

Image processing techniques are widely use in astronomy, and are of particular interest in the frame of coma structure analysis. Besides the usual processing required to correct the images from the noise or instrumental effects, special enhancement of the exposures are needed to reveal the patterns embedded in the coma. A common problem in image filtering is to understand whether everything we see in the final image is real or some artifacts have been introduced during the processing. Part of this work consisted in testing different filters and techniques in order to decide which one suits the best for a given image. Among the techniques implemented we found that the Larson-Sekanina filter, which is one of the most widely used, provides good results if the original image is not too noisy, or if the signal of the structures is not too low with respect to the background. In the latter case, we would rather use a non-linear filter like the adaptive Laplace one, which might display the structures with less details than a difference filter but will detect most of them even in the case of very poor ratio signal/noise. We do not recommend the use of a radial normalization filter; if it detects patterns in the coma, it introduces also artifacts which are sometimes difficult to separate from the real features. In any case, a parallel processing with different filters (linear and non-linear for example) is highly recommended for all images.

5.1.2 Numerical model

Developing a numerical model of dust coma structures has been the most challenging work of this thesis. We wanted to start with a new approach including constraints on the shape of the nucleus and the size of the active regions in the simulation. This method had never been tested extensively before and is therefore a "first" worldwide. During the process of implementing the model as a MATLAB code, we faced some difficulties, especially because of the numbers of parameters to consider in order to perform a true inversion from the ground-based images to the local activity at the surface of the nucleus. We finally opted for an hybrid approach: in a first step we infer the spin axis orientation with a direct inversion from the images of the structures. Providing that we have enough exposures, a unique solution can be constrained easily. In a second step, we simulate the coma structures with a trial-and error approach combined with educated guesses for the starting parameters. Although we would prefer to have a direct inversion (whether it is possible or not is still debated), this technique has proved itself very efficient.

5.1.3 Application to real objects

As stated in Chapter 4 we obtained interesting results for comets 73P/Schwassmann-Wachmann 3-B,C and 9P/Tempel 1, which are in excellent agreement with existing publications from in-situ measurements. The most interesting result being the fact that we could use our model not only to localize the active regions at the surface of Tempel 1, but also to describe precisely the activity in terms of diurnal profile, size of the grains, or velocities involved.

It is clear that ground-based observations cannot compete with spacecraft data in terms of resolution, however this study shows that when combined with a good modeling they can provide significant information, even on the nucleus surface itself, which is not directly observable from Earth when the comet is active.

5.2 Outlook of this work

5.2.1 A new tool for studying comets

When we started this work, we were wondering whether we could develop a new model of coma structures, and if this approach would be positive. At the end of this PhD, we have finally reached a step where we find ourselves confident with the numerical model we have developed, in terms of both implementation choices and results achieved. We have now a new tool for cometary research which allows us to infer important parameters and constrains on the activity of any comets for which observations of coma structures are available. Of course the model is still not perfect and we are already working on some improvements. For instance we want to implement a more realistic photometric model. For now we can only retrieve dynamical parameters of the dust grains. With a better photometric model, we might be able to infer also the flux of particles emitted, therefore bringing new insights on the activity.

An other outlook concerns the determination of the nucleus shape. We have seen that it is an important parameter for the simulation, therefore if not available we have to

find a way to constrain it and the coma structure model cannot be used for this purpose (albeit to some extent we can use it to exclude some shapes). We are now looking in the direction of light curve inversion, from ground-based observations of the same target at large heliocentric distance when the nucleus is inactive. This has been done heavily for asteroids but so far only a few attempts have been taken to infer the shape of a cometary nucleus.

Meanwhile, as we have already a good working model, we plan to apply it to as many comets as we can. Many observations of coma structures are available for many comets, some of them never published or analyzed with more details than a morphological description. Among them one immediate target of interest is the comet 67P/Churyumov-Gerasimenko.

5.2.2   Next target: 67P/Churyumov-Gerasimenko

Discovered on on September 11, 1969 by Klim Ivanovich Churyumov and Svetlana Gerasimenko this comet will probably be the most studied ever as it is the target of ESA's mission ROSETTA. The main purpose of this mission is to conduce an extensive survey of the cometary nucleus by landing a module at the surface for in-situ experiments while an orbiter will orbit around the comet for at least several months. This project is incredibly challenging from both scientific and technical point of views, and the knowledge we will gather can be invaluable for our understanding of comets.

However we still now very little about the nucleus itself, and while we still have time (encounter scheduled for 2014) it is good to start looking more in details at the activity and see if we can provide support to the spacecraft team. So far we have observed many coma structures around this nucleus, indicating the presence of active regions at the surface. We are planning now to start analyzing the images with our model and see if we can constrain the location of these regions at the surface and the properties of the dust grains emitted as they could be an hazard for the spacecraft.
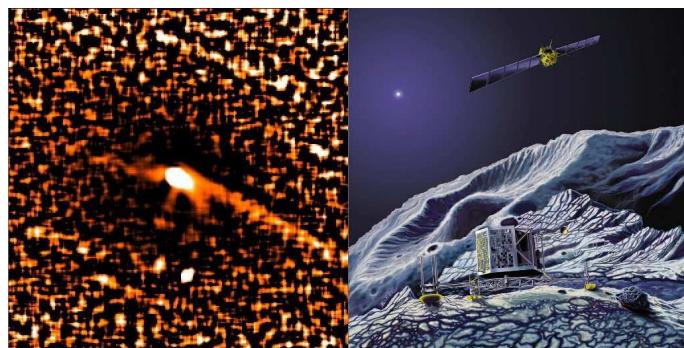

Figure 5.1: Left panel: Dust coma structures in a Laplace filtered image of comet 67P acquired on 19/03/2009 from Calar Alto observatory (Source: Luisa-Maria Lara, personal communication). Right panel: artistic rendering of the nucleus of comet 67P with the lander Philae and the orbiter ROSETTA (Source: ESA).

A Celestial Mechanics: A short reference

This appendix summarizes the orbital calculations we implemented in our model. It is assumed that the reader has already some experience with these concepts. Hence, the text should be considered only as a short reference for the equations and not a complete text book on celestial mechanics.

A.1 Basic mechanics and Kepler's laws

Comets, as any object in the Solar System follow keplerian orbits around the Sun. Kepler defined these orbits with three laws:

1. The orbit of every object orbiting around the Sun is an ellipse with the Sun at a focus.

2. A line joining the object and the Sun sweeps out equal areas during equal intervals of time.

3. The square of the orbital period is proportional to the cube of the semi-major axis of its orbit.

In mathematical terms, and for an elliptic orbit, these laws are represented by:

First law:
$$r = \frac{q \times (1 + e)}{1 + e \cos v} \tag{A.1}$$

Second law:
$$\frac{1}{2} r^2 \dot{v} = \frac{C}{2} \tag{A.2}$$

$$\text{with } \frac{C^2}{\mu} = q \times (1 + e) \tag{A.3}$$

Third law:
$$\frac{T^2}{a^3} = \frac{4\pi^2}{\mu} \tag{A.4}$$

In these equations, r is the distance from the Sun, q the perihelion distance, e the eccentricity, v the true anomaly (i.e. the angular position on the orbit with $v = 0$ at perihelion), $\mu = GM_\odot = 1.32 \times 10^{11} km^3.s^{-2}$, C a constant obtained from the second law,

$\dot{\nu}$ is the angular velocity, T is the orbital period and a the length of the semi-major axis of the orbit.

Note: In the case of elliptic orbits, the perihelion distance is given by $q = a(1 - e)$ where a is the semi-major axis of the ellipse. Using this relation we can replace $q(1 + e)$ with $a(1 - e^2)$ in equations A.1 and A.3. For parabolic and hyperbolic orbits the equations must be slightly modified. In the parabolic case $e = 0$) and $q = a$, while for an hyperbolic orbit we have $e > 1$ and therefore we must define $q = a(e - 1)$.

These orbits are generally defined by a set of parameters called orbital elements, that are in theory sufficient to calculate the position of the comet at any time. In reality, these parameters evolve with time. The Sun is not the only source of gravity in our Solar System and orbits may be perturbed by the gravitational action of the giant planets, mainly Jupiter. Usually orbital elements are defined for a certain epoch and within it they are good enough to calculate the object positions without including any perturbations, unless the orbit passes too close to one of the giant planets. Orbital elements are available in different sources but we found very convenient to use the online tool "HORIZONS" from the NASA Jet Propulsion Laboratory `http://ssd.jpl.nasa.gov/horizons.cgi`. Figure A.1 gives an overview of the main orbital element and their geometrical implications for an orbit. The seven following parameters are the only ones we need to constrain the orbit and the motion of the comet:

- e = eccentricity (0=circle, 0-1=ellipse, 1=parabola, >1=hyperbola)

- a = semi-major axis

- i = inclination to the ecliptic

- Ω = longitude of the ascending node

- ω = argument of perihelion

- n = mean motion (degrees/day)

- M = mean anomaly (0 at perihelion; increases uniformly with time)

- T_0 = reference epoch (Julian Day)

Note to the reader: Unless stated otherwise, distances are always measured in astronomical units and angles in degrees in all the equations of this chapter.

A.2   From orbital elements to Right Ascension and Declination

In the following session, we present the calculations for an elliptic orbit as it is the only one implemented in the code. Indeed they represent the majority of observed comets while hyperbolic orbits account for a minority of bodies leaving our solar system and parabolic orbits can be approximated with very elongated elliptic orbits.
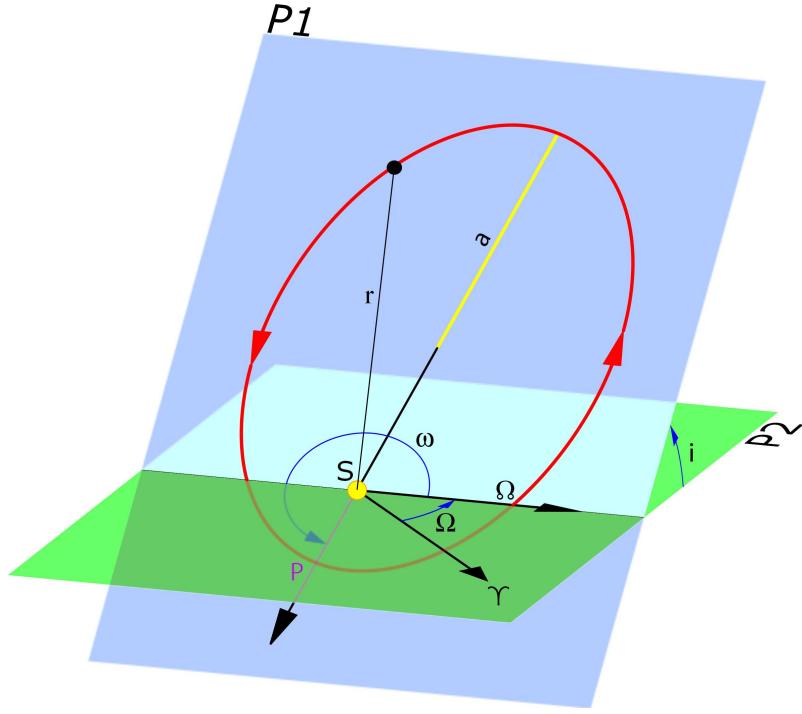
Figure A.1: Schematic of a keplerian orbit and the associated orbital elements. P1 is the orbital plane of the object we want to study, P2 the ecliptic. Orbital elements are defined in the text. Source: http://en.wikibooks.org/wiki/File:Orbital_elements.svg

In order to know the position of the comet in the sky, one needs to calculate the following quantities:

Mean anomaly M_{obs} at time of observation:

$$M_{obs} = M + n \times (T_{obs} - T_0) \tag{A.5}$$

Eccentric anomaly E, calculated by iteratively solving Euler's equation:

$$M_{obs} = E - e \sin(E) \tag{A.6}$$

True anomaly v and distance to the Sun r:

$$v = 2 \times \left[\arctan\left(\sqrt{\frac{1+e}{1-e}} \tan\left(\frac{E}{2}\right) \right) \right] \tag{A.7}$$

$$r = \frac{a \times (1 - e^2)}{1 + e \cos v} \tag{A.8}$$

Heliocentric ecliptical polar coordinates of the comet:

$$NA = \arctan\left(\frac{\tan(\omega)}{\cos(i)} \right) \tag{A.9}$$

$$NL = \arctan\left(\tan(NA + v) \cos i \right) \tag{A.10}$$

$$L = \Omega + NL \tag{A.11}$$

$$B = \arctan\left(\sin(NL) \tan(i) \right) \tag{A.12}$$

where L and B are respectively the ecliptical Longitude and Latitude of the comet.

Finally we can transform L and B to get the cartesian position of the comet in the ecliptical frame:

$$x_h = r\cos(B)\cos(L) \tag{A.13}$$
$$y_h = r\cos(B)\sin(L) \tag{A.14}$$
$$z_h = r\sin(B) \tag{A.15}$$

By now, we know already the position of the comet in the heliocentric ecliptical frame in two different coordinate systems (polar and rectangular). The next step is the calculation of this position in a geocentric frame. This means that we should first calculate where is the Sun in this frame, then transform the coordinates of the comet in the new frame.

The geocentric ecliptical coordinates of the Sun can be obtained using an algorithm proposed by Meeus (1998). This technique uses a series of numerical values determined from observations, and considers the Earth orbit as a pure ellipse (we neglect any perturbations from the Moon or the other planets). The precision obtained with this method $(0.01°)$ is good enough for our needs. A summary of the algorithm follows:

Fraction of time since the beginning of the current epoch:

$$\tau = \frac{T_{obs} - 2451545.0}{36525} \tag{A.16}$$

Geometric mean longitude of the Sun:

$$L_\odot = 280.46645 + 36000.76983\tau + 0.0003032\tau^2 \tag{A.17}$$

Mean anomaly of the Sun:

$$M_\odot = 357.52910 + 35999.05030\tau + 0.0001559\tau^2 - 0.00000048\tau^3 \tag{A.18}$$

Eccentricity of the Earth's orbit (i.e. eccentricity of the Sun's orbit in a geocentric frame):

$$e_\oplus = 0.016708617 - 0.000042037\tau - 0.0000001236\tau^2 \tag{A.19}$$

Sun's equation of center $C_\odot$:

$$C = (1.9146 - 0.004817\tau - 0.000014\tau^2)\sin(M_\odot) \tag{A.20}$$
$$+ (0.019993 - 0.000101\tau)\sin(2M_\odot) \tag{A.21}$$
$$+ 0.00029\sin(3M_\odot) \tag{A.22}$$

Sun's true longitude and anomaly:

$$\Lambda_\odot = L_\odot + C_\odot \tag{A.23}$$
$$\nu_\odot = M_\odot + C_\odot \tag{A.24}$$

From there we can calculate easily the geocentric ecliptical coordinates of the Sun:

$$R_\odot = 1.000001018 \times \frac{1 - e_\oplus^2}{1 + e\cos(\nu_\odot)} \tag{A.25}$$
$$\Omega_\odot = 125.04 - 1934.136\tau \tag{A.26}$$
$$L_\odot = \Lambda_\odot - 0.00569 - 0.00478\sin(\Omega_\odot) \tag{A.27}$$

And its geocentric cartesian coordinates:

$$x_\odot = R_\odot \cos(L_\odot) \tag{A.28}$$

$$y_\odot = R_\odot \sin(L_\odot) \tag{A.29}$$

$$z_\odot = 0 \tag{A.30}$$

Note: The geocentric frame we use share the same main plane with the heliocentric frame (ecliptic plane). Therefore the latitude of the Sun in this frame is always zero.

So far we have defined the position of the Sun with respect to the Earth, and the position of the comet with respect to the Sun *in the same ecliptic frame*. Therefore the position of the comet with respect to the Earth is easily calculated by taking the sum of the two vectors:

$$x = r\cos(B)\cos(L) + R_\odot\cos(L_\odot) \tag{A.31}$$

$$y = r\cos(B)\sin(L) + R_\odot\sin(L_\odot) \tag{A.32}$$

$$z = r\sin(B) \tag{A.33}$$

And the distance between the Earth and the comet is the norm of this new vector:

$$\Delta = \sqrt{x^2 + y^2 + z^2} \tag{A.34}$$

We have now obtained all what we need to project the position of the comet in the sky. However we did not take into account the fact that the comet can be several astronomical units from us and its real position is not exactly the one we see because of the time the light need to travel from the comet to our observatory, and because of the Earth's motion during the observation. This phenomenon is called *planetary aberration* and can be corrected by defining a new observation time:

$$T_{obs,new} = T_{obs} - \Delta/c \quad (c \text{ the speed of light}) \tag{A.35}$$

$$= T_{obs} - 0.0057755183 \times \Delta \quad (\text{for } c \text{ in } AU.s^{-1}) \tag{A.36}$$

We can then inject this new observing time in equation A.5 and run again the same algorithm to calculate a better value for the coordinates of our target.

The geocentric ecliptical cartesian coordinates can be converted in angular coordinates easily:

$$\lambda = \arctan\left(\frac{y}{x}\right) \tag{A.37}$$

$$\beta = \arctan\left(\frac{z}{x^2 + y^2}\right) \tag{A.38}$$

We can convert these angular coordinates to Right Ascension and Declination, using the fact that the Earth equator is tilted with respect to the ecliptic, with an angle $\epsilon = 23.4392911111111°$.

$$RA = \arctan\left(\frac{\sin(\lambda)\cos(\epsilon) - \tan(\beta)\sin(\epsilon)}{\cos(\lambda)}\right) \tag{A.39}$$

$$DEC = \arcsin\left(\sin(\lambda)\cos(\beta)\sin(\epsilon) + \sin(\beta)\cos(\epsilon)\right) \tag{A.40}$$

This values are given in degrees. To be consistent with the official notation, we finally convert RA to [hours, minutes, seconds] and DEC to [degrees, arcminutes, arcseconds]

A.3   From the nucleus to our plane of sky

When dust particles are emitted from the nucleus surface, they follow also a keplerian which differs from the nucleus one as explained in chapter 3. Instead of calculating their orbit directly in the geocentric frame, it is easier to compute first the positions in a cometary-centered frame, and convert them later to geocentric coordinates and sky positions.

For the sake of clarity initial positions are defined in latitude and longitude in the local cometocentric frame:

- center $\equiv$ nucleus center

- main plane (X, Y) is the equatorial plane

- z completes the frame (X, Y, Z) and points to the positive pole of the nucleus.

We transform them into a new coordinates system: the cometocentric frame, which is an orthogonal frame defined as follows:

- center $\equiv$ nucleus center

- main plane (Z, Y) is the orbital plane, with X pointing to the Sun

- z completes the frame (X, Y, Z) and points to the positive pole of the orbit.

This transformation is done by rotating the frame around the axis Y with an angle $(90° - I)$ and around the axis Z with an angle $-(\Phi + v)$. These rotations can be understood easily if one considers how the spin axis orientation is defined: - I is the angle between the rotation axis of the nucleus and the orbital plane, - Φ is the angle of the projected direction of the spin axis on the orbital plane at perihelion, $\Phi = 0°$ being the direction of the Sun at perihelion.

The transformation is implemented in the code with an algebraic formula where each rotation is represented by its matrix:

$$
\begin{pmatrix} x \\ y \\ z \end{pmatrix}_{\text{comet. orbit.}} = \begin{pmatrix} \cos(\Phi + v) & -\sin(\Phi + v) & 0 \\ \sin(\Phi + v) & \cos(\Phi + v) & 0 \\ 0 & 0 & 1 \end{pmatrix} \times \begin{pmatrix} \sin(I) & 0 & \cos(I) \\ 0 & 1 & 0 \\ -\cos(I) & 0 & \sin(I) \end{pmatrix} \times \begin{pmatrix} x \\ y \\ z \end{pmatrix}_{\text{comet. equ.}}
$$
(A.41)

In the orbital frame, the acceleration acts only along the X axis. Therefore after a time t, the new position of a dust particle can be expressed as:

$$
x = x_0 + v_{0,x}t - \frac{1}{2}a_0 t^2
$$
(A.42)

$$
y = y_0 + v_{0,y}t
$$
(A.43)

$$
z = z_0 + v_{0,z}t
$$
(A.44)

Where v_0 is the initial velocity and a_0 the combination of solar gravity and radiation pressure as defined in Ch.3.

The conversion between this frame and the geocentric one is done through several rotations:

- we define first some angles for the rotations:

  - θ is the angle between the orbital north pole and the vector orthogonal to the plane Sun-Comet-Earth

  - $\widehat{STO}$ is the angle Sun-Target-Observer

  - $\widehat{PsAng}$ is the angle the extended Sun-comet radius vector makes with the Earth North direction in the exposures.

- rotating the cometocentric frame $(X, Y, Z)_{comet}$ around its axis X with an angle θ aligns the axis Z with the normal of the plan Sun-Comet-Earth.

- rotating the frame around this axis Z with an angle $\widehat{STO}$ points the axis X to the Earth.

- The final frame has now its X axis parallel to the line of sight, the plane Y, Z identical to the plane of sky, with the axis Z normal to the plane Sun-Comet-Earth.

- the last step consist in orienting the plane (Y, Z) in order to have the Earth north pole direction to the top and the East direction to the left in the final image. This is done by rotating the frame around the axis X with the angle $90 + \widehat{PsAng}$.

The whole transformation is implemented in the code with an algebric formula where each rotation is represented by its matrix:

$$
\begin{pmatrix} x \\ y \\ z \end{pmatrix}_{\text{geo. equ.}} = \begin{pmatrix} 1 & 0 & 0 \\ 0 & -\sin(\widehat{PsAng}) & -\cos(\widehat{PsAng}) \\ 0 & \cos(\widehat{PsAng}) & -\sin(\widehat{PsAng}) \end{pmatrix}
$$

$$
\times \begin{pmatrix} \cos(\widehat{STO}) & -\sin(\widehat{STO}) & 0 \\ \sin(\widehat{STO}) & \cos(\widehat{STO}) & 0 \\ 0 & 0 & 1 \end{pmatrix} \times \begin{pmatrix} 1 & 0 & 0 \\ 0 & \cos(\theta) & -\sin(\theta) \\ 0 & \sin(\theta) & \cos(\theta) \end{pmatrix} \times \begin{pmatrix} x \\ y \\ z \end{pmatrix}_{\text{comet. orbit.}} \tag{A.45}
$$

And we finally obtain the projected position of the particle in our plane of sky.

$$
\begin{pmatrix} RA \\ DECL \end{pmatrix}_{\text{dust grain}} = \begin{pmatrix} RA \\ DECL \end{pmatrix}_{\text{nucleus}} + \begin{pmatrix} y \\ z \end{pmatrix}_{\text{geo. equ.}} \tag{A.46}
$$

B   COSSIM User Manual

B.1   Introduction and programming choices

This appendix describes the program COSSIM (COma Structures SIMulator) we developed in the framework of this PhD thesis. The original version is developed as a MATLAB package but can also be distributed as a standalone compiled version. Both versions are independent from the computer operating system.

One of the choices we had to face during the development was to decide how to organize the interaction between the user and the code. In a perfect world one has a set of images displaying coma structures and wants the program to reproduce these structures and return the parameters ensuring the best simulation. Therefore the software would act as a black box fed with images and giving back information on the nucleus activity.

In reality this perfect inversion is difficult to achieve. A typical inversion routine works by trial and errors, the code refining all the parameters by itself in order to achieve the best result. The problem here is how to define what is a "good" result for the computer. We usually simulate the motion of particles and produce an image of the structures which we compare to the original images. Our simulation has usually a clean look, whereas the original images are noisy, with the structures partly hidden in the coma background. If the comparison is easy for the human eye, it is much more difficult for the computer. Therefore, as explained is Chapter 3 we do not perform a direct inversion but a trial and error approach, where the user changes himself the main parameters of the simulation and compares the results with the real observations directly or with any other image processing software.

However, in order to make this approach more user friendly, we developed a graphical interface (GUI) which makes the whole process easier and helps the user to understand better the geometry of the nucleus and the behavior of the dust particles.

B.2   User Manual

B.2.1   Configuration files

Once launched, the GUI is self sufficient for defining the parameters and running the simulation. However in order not to clutter too much the display, we decided that some parameters had to be defined externally in a configuration file. These parameters are the ones very unlikely to be changed for a given simulation, namely the orbital elements of the comet (necessary file) and the shape model of the nucleus (optional, required only if the option is activated in the GUI).

B.2.1.1   Orbital elements

The orbital elements file will be interpreted as a MATLAB script and should be written with the following syntax:

```
% WARNING : The order for writing these orbital elements
% does not matter but the syntax MUST be preserved.
%
%     e = eccentricity
%     a = semi-major axis (AU)
%     QR = perihelion distance (AU)
%     inc = inclination to the ecliptic (degrees)
%     OM = longitude of the ascending node (degrees)
%     w = argument of perihelion (degrees)
%     T0 = reference epoch (JD)
%     n = mean motion (degrees/day)
%     M = mean anomaly (degrees)
%     Tp = time of perihelion passage (JD)

% orbital elements for 9P/Tempel 1
e = 0.5171007800527672;
a = 3.123820882622393;
QR = 1.50849066747323;
inc = 10.52698377735023;
OM = 68.93306928065827;
w = 178.926168693708;
T0 = 2454771.5;
n = 0.178515071;
M = 216.81533185837;
Tp= 2455573.587280078; % = 12/01/2011
```

B.2.1.2   Shape model

We explained in Chapter 3 that we used our own format to define the shape model of the nucleus. To get it is rather easy. If the shape is already defined in the standard OBJ format, it can be converted directly to our internal format by the routine `loadModel.m`. Otherwise, the original format needs to be converted first to OBJ. As it is a standard, all softwares dealing with 3D creation are able to write a file in this format.

B.2.2   Graphical interface

From the MATLAB command line, the program is launched by typing the command "cossim". COSSIM displays two slightly different interfaces according to the mode selected by the user.

1. the "Regions" mode displays a 3-dimensional view of the nucleus and helps to define the position of the active regions, but also to understand the relative position

of the Sun and the observer with respect to the nucleus, and the illumination of the surface.

2. the "Image" mode displays the simulation results as it would be seen from the observer and can export the final image as a *.fits file.

All parameters concerning the simulation can be changed interactively in both interfaces. By default, the program starts in "regions" mode as in Fig. B.1.
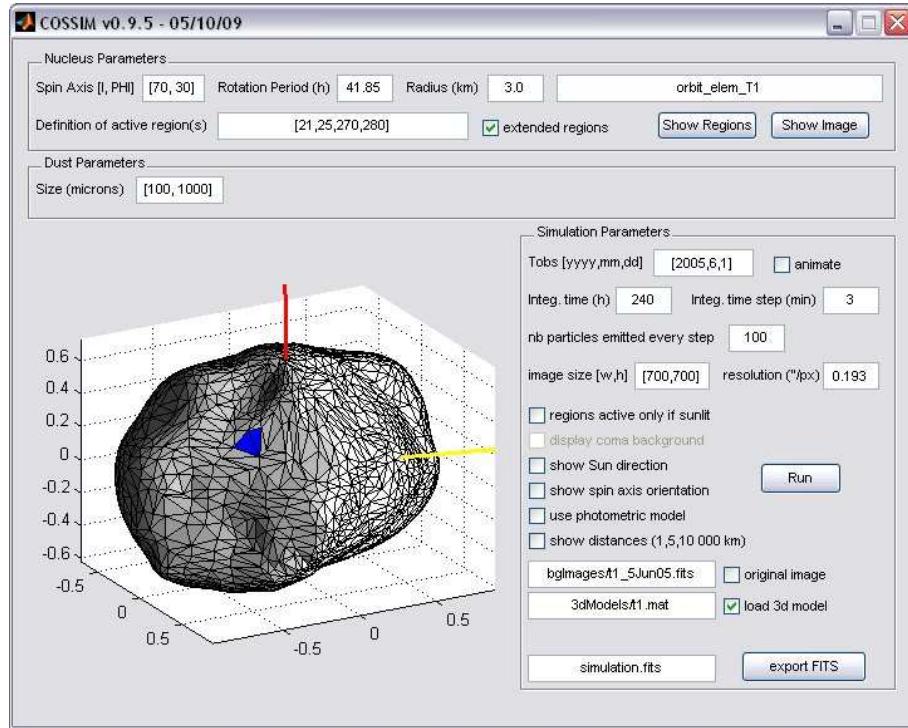

Figure B.1: COSSIM GUI, "Regions" mode

The GUI is divided in four elements:

B.2.2.1 Nucleus parameters

The first box in the interface defines the main parameters describing the nucleus: name of the file containing the list of orbital elements, radius of the nucleus, rotational period, orientation of the spin axis, and position of the active regions. Included in this box are also the buttons "Show Regions" and "Show Image" for switching between the two interfaces.

Note 1: The spin axis is given with its coordinates I & Φ as defined in Vincent et al. (2010a), i.e. I is the angle between the spin axis and the orbital plane and Φ is the longitude of the spin axis at perihelion, with zero longitude along the extended sun-comet vector at perihelion.

Note 2: Active regions are defined with their local coordinates at the surface in the form:

[latitude 1, longitude 1, ..., latitude n, longitude n].

If the option "extended regions" is selected, regions should be defined by their limits in latitude and longitude:

[latitude min 1, latitude max 1, longitude min 1, longitude max 1, ...].

There is no limit in the number of active regions defined at the same time, however it is not possible to have in the same simulation point source regions and extended ones.

B.2.2.2   Dust Parameters

We have seen in Chapter 3 that the dust motion depends on many parameters but all of them can be estimated realistically from the grain size distribution. Hence the user defines the dust by simply indicating a range of size in micrometers for the distribution of particles. The calculation of all the other parameters (velocity, β, ...) is done internally and cannot be modified from the interface. However one can simply edit the code and modify the equations as needed. The routines are well commented so it is quite easy to change any parameter in order to achieve a better simulation.

B.2.2.3   Simulation Parameters

. The first two set of parameters were describing general properties of the comet. The last one contains specific parameters for the simulation itself. In order to translate the activity into an image, the program needs to know:

- the observation date,

- the integration time in hours (i.e. when the "oldest" particles in the image were emitted. Typically a few days),

- integration step in minutes. Indicates to the program when to emit particles in the time frame defined above.

- number of particles emitted at each step,

- size (in pixels) and resolution (in arc second/pixel) of the final image,

- a button "Run" to start the simulation,

- several options that will be discussed later on.

B.2.2.4   Display

The final element of the GUI is the display. It displays a close view of the nucleus or the final simulation of the coma structures, both views oriented as we would see them at the time of observation. The program switches automatically to the "Image" mode when the "Run" button is clicked (see Fig. B.2).

B.2.2.5 Options

Several options are available to enhance the simulation or understand better the display:

- "Regions active only when sunlit". By default active regions are always emitting dust. If this option is selected, the activity will be moderated by the illumination at the surface.

- "Use photometric model". Unless this option is activated, particles are all considered to emit light with the same intensity, which means the final image in this case is simply a count of particles per pixel. It helps to understand the dynamics of the dust but it is better to activate the photometric mode when we want to compare with a real image.

- "Show spin axis orientation" and "Show Sun direction". In the "Regions" mode, the spin axis and the direction of the Sun are always displayed. These options make this information available also in the "Image" mode if needed. It can be useful sometimes to understand the effects of the projection from a 3D situation to a 2D image.

- "Load original image". This option allows to compare directly the simulation with the reality by displaying the results on top of the original image of the coma structures. See Fig. B.3 for an example.

- "Load 3D model". If this option is selected, the user must enter the name of file containing the shape of the nucleus.

- "Export FITS" saves the simulated image.

B.2.2.6 Outputs

Beyond the simulation of coma structures we want to retrieve as much information as we can on the activity. For this purpose, the program does not only displays the simulated structures but prints also several information and parameters calculated throughout the simulation process:

- summary of all options selected, and parameters defined by the user.

- total number of particles in the image,

- size, velocity, and β distribution.

These informations are added to the header of the FITS image when exported.
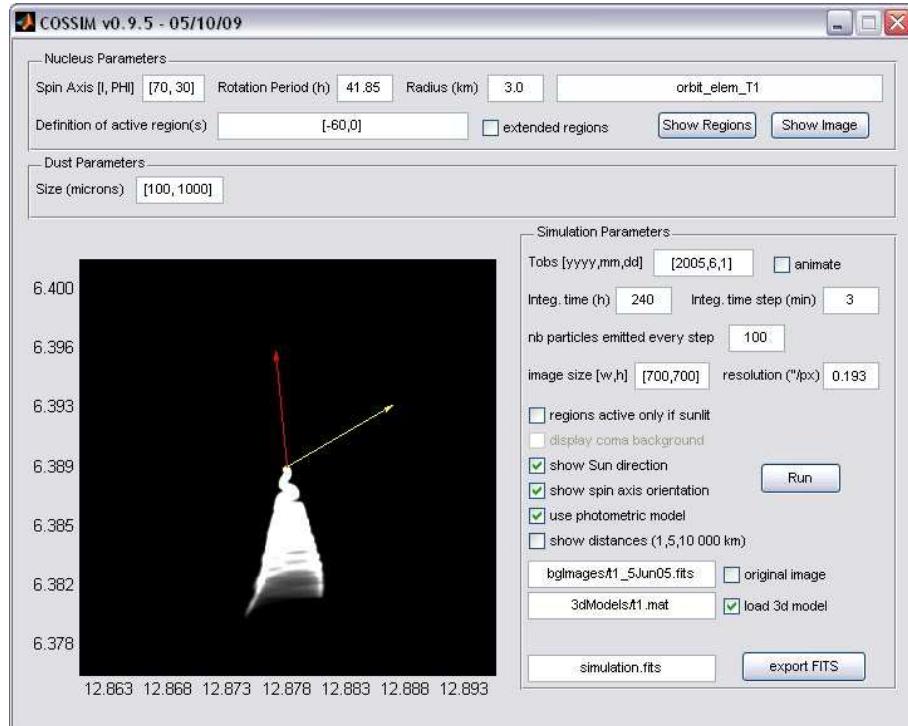
Figure B.2: COSSIM GUI, "Image" mode
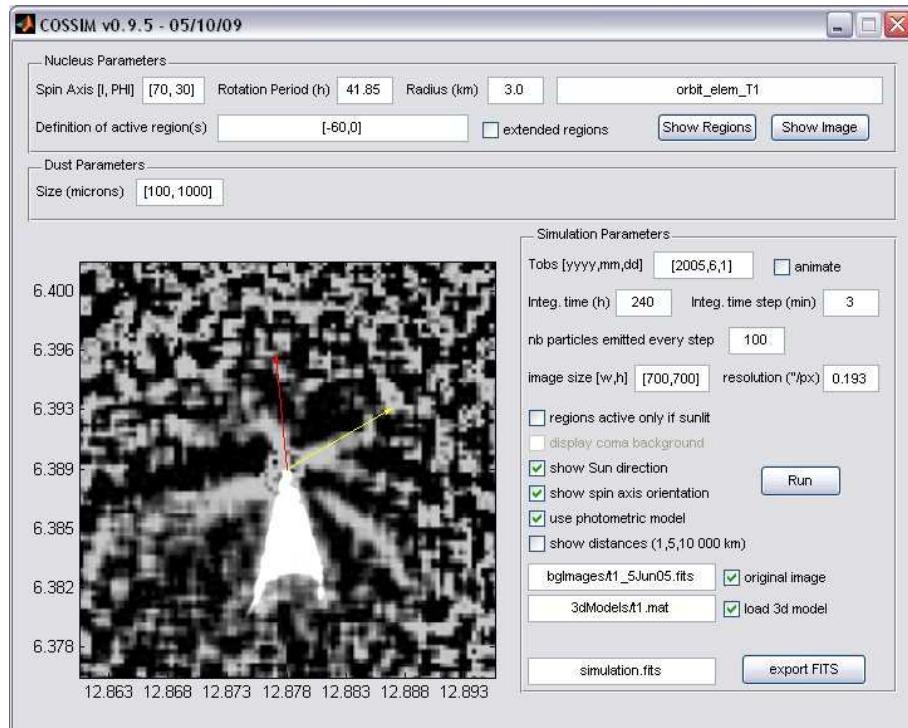
Figure B.3: COSSIM GUI, "Image" mode with original image displayed under the simulation.

Bibliography

Alfvèn, H., 1957, On the theory of comet tails., Tellus, 9, 92

Belton, M. J. S., Meech, K. J., A'Hearn, M. F., Groussin, O., McFadden, L., Lisse, C., Fernández, Y. R., Pittichová, J., Hsieh, H., Kissel, J., Klaasen, K., Lamy, P., Prialnik, D., Sunshine, J., Thomas, P., Toth, I., 2005, Deep Impact: Working Properties for the Target Nucleus Comet 9P/Tempel 1, Space Science Reviews, 117, 137–160

Bertini, I., Lara, L. M., Vincent, J.-B., Boehnhardt, H., Küppers, M., Rodrigo, R., 2009, Activity evolution, outbursts, and splitting events of comet 73P/Schwassmann-Wachmann 3, A&A, 496, 235–247

Biermann, L., 1951, Kometenschweife und solare Korpuskularstrahlung, Zeitschrift fur Astrophysik, 29, 274–286

Boehnhardt, H., Birkle, K., 1994, Time variable coma structures in comet P/Swift-Tuttle., A&A, 107, 101–120

Boehnhardt, H., Birkle, K., Fiedler, A., Jorda, L., Thomas, N., Peschke, S., Rauer, H., Schulz, R., Schwehm, G., Tozzi, G., West, R., 1997, Dust Morphology Of Comet Hale-Bopp (C/1995 O1): I. Pre-Perihelion Coma Structures In, Earth Moon and Planets, 78, 179–187

Böhnhardt, H., 2004, Split comets, In: Comets II, Edited by Festou, M. C., Keller, H. U., & Weaver, H. A., University of Arizona Press, pp. 301–316

Böhnhardt, H., Kaufl, H. U., Keen, R., Camilleri, P., Carvajal, J., Hale, A., 1995, Comet 73P/Schwassmann-Wachmann 3, IAUC, 6274

Böhnhardt, H., Holdstock, S., Hainaut, O., Tozzi, G. P., Benetti, S., Licandro, J., 2002, 73p/Schwassmann-Wachmann 3 - One Orbit after Break-Up: Search for Fragments, Earth Moon and Planets, 90, 131–139

Bonev, T., Boehnhardt, H., Borisov, G., 2008, Broadband imaging and narrowband polarimetry of comet 73P/Schwassmann-Wachmann 3, components B and C, on 3, 4, 8, and 9 May 2006, A&A, 480, 277–287

Burns, J. A., Lamy, P. L., Soter, S., 1979, Radiation forces on small particles in the solar system, Icarus, 40, 1–48

Cremonese, G., Boehnhardt, H., Crovisier, J., Rauer, H., Fitzsimmons, A., Fulle, M., Licandro, J., Pollacco, D., Tozzi, G. P., West, R. M., 1997, Neutral Sodium from Comet Hale-Bopp: A Third Type of Tail, ApJ, 490, 199–202, arXiv:astro-ph/9710022

Cremonese, G., Huebner, W. F., Rauer, H., Boice, D. C., 2002, Neutral sodium tails in comets, Advances in Space Research, 29, 1187–1197

Crifo, J.-F., Loukianov, G. A., Rodionov, A. V., Zakharov, V. V., 2005, Direct Monte Carlo and multifluid modeling of the circumnuclear dust coma. Spherical grain dynamics revisited, Icarus, 176, 192–219

Delsemme, A. H., 1982, Chemical composition of cometary nuclei., In: Comets, Edited by L. Wilkening, University of Arizona Press, pp. 85–130

Farnham, T. L., Wellnitz, D. D., Hampton, D. L., Li, J.-Y., Sunshine, J. M., Groussin, O., McFadden, L. A., Crockett, C. J., A'Hearn, M. F., Belton, M. J. S., Schultz, P., Lisse, C. M., 2007, Dust coma morphology in the Deep Impact images of Comet 9P/Tempel 1, Icarus, 187, 26–40

Feaga, L. M., A'Hearn, M. F., Sunshine, J. M., Groussin, O., Farnham, T. L., 2007, Asymmetries in the distribution of H_2O and CO_2 in the inner coma of Comet 9P/Tempel 1 as observed by Deep Impact, Icarus, 190, 345–356

Finson, M. L., Probstein, R. F., 1968, A theory of dust comets. I. Model and equations, AJ, 154, 353–380

Fulle, M., 1987, A new approach to the Finson-Probstein method of interpreting cometary dust tails, A&A, 171, 327–335

Fulle, M., 1999, Constraints on the Dust Size Distribution of 46P/Wirtanen from In-Situ and Ground-Based Observations, Advances in Space Research, 24, 1087–1093

Fulle, M., 2004, Motion of cometary dust, In: Comets II, Edited by Festou, M. C., Keller, H. U., & Weaver, H. A., University of Arizona Press, pp. 565–575

Fulle, M., Sedmak, G., 1988, Photometrical analysis of the Neck-Line structure of Comet Bennet 1970II, Icarus, 74, 383–398

Gomes, R., Levison, H. F., Tsiganis, K., Morbidelli, A., 2005, Origin of the cataclysmic Late Heavy Bombardment period of the terrestrial planets, Nature, 435, 466–469

Groussin, O., A'Hearn, M. F., Li, J.-Y., Thomas, P. C., Sunshine, J. M., Lisse, C. M., Meech, K. J., Farnham, T. L., Feaga, L. M., Delamere, W. A., 2007, Surface temperature of the nucleus of Comet 9P/Tempel 1, Icarus, 187, 16–25

Keller, H. U., Britt, D., Buratti, B. J., Thomas, N., 2004, In situ observations of cometary nuclei, In: Comets II, Edited by Festou, M. C., Keller, H. U., & Weaver, H. A., University of Arizona Press, pp. 211–222

Kimura, H., Liu, C., 1977, On the structure of cometary dust tails., Chin. Astron., 1, 235–264

Kuiper, G. P., 1951, On the Origin of the Solar System, Proceedings of the National Academy of Science, 37, 1–14

Lara, L. M., Böhnhardt, H., Gredel, R., Gutiérrez, P. J., Ortiz, J. L., Rodrigo, R., Vidal-Nuñez, M. J., 2006, Pre-impact monitoring of Comet 9P/Tempel 1, the Deep Impact target, A&A, 465, 1151–1157

Larson, S. M., Sekanina, Z., 1984, Coma morphology and dust-emission pattern of periodic Comet Halley. I - High-resolution images taken at Mount Wilson in 1910, AJ, 89, 571–578

Laufer, D., Notesco, G., Bar-Nun, A., Owen, T., 1999, From the Interstellar Medium to Earth's Oceans via Comets-An Isotopic Study of HDO/H_2O, Icarus, 140, 446–450

Levison, H. F., Dones, L., 2007, Encyclopedia of the Solar System Second Edition, Chapter 31, Academic Press

Li, J.-Y., A'Hearn, M. F., Belton, M. J. S., Crockett, C. J., Farnham, T. L., Lisse, C. M., McFadden, L. A., Meech, K. J., Sunshine, J. M., Thomas, P. C., Veverka, J., 2007, Deep Impact photometry of Comet 9P/Tempel 1, Icarus, 187, 41–55

Markovich, M. Z., Markovich, N. M., 2001, Size Distribution of Cometary Dust Particles, Solar System Research, 35, 320–326

Marsden, B. G., Sekanina, Z., Everhart, E., 1978, New osculating orbits for 110 comets and analysis of original orbits for 200 comets, AJ, 83, 64–71

Meeus, J., 1998, Astronomical algorithms (2nd ed.), Willmann-Bell

Mendillo, M., Wilson, J. K., Baumgardner, J., Cremonese, G., Barbieri, C., 1998, Imaging Studies of Sodium Tails in Comets, in Bulletin of the American Astronomical Society, vol. 30 of Bulletin of the American Astronomical Society, p. 1062

Mie, G., 1908, Beiträge zur Optik trüber Medien speziell kolloidaler Goldlösungen, Ann. Phys., 25, 377–445

Min, M., Hovenier, J. W., de Koter, A., Waters, L. B. F. M., Dominik, C., 2005, The composition and size distribution of the dust in the coma of Comet Hale Bopp, Icarus, 179, 158–173

Morbidelli, A., 2005, Origin and Dynamical Evolution of Comets and their Reservoirs, ArXiv Astrophysics e-prints, arXiv:astro-ph/0512256

Oort, J. H., 1950, The structure of the cloud of comets surrounding the Solar System and a hypothesis concerning its origin, Bull. Astron. Inst. Netherlands, 11, 91–110

Richardson, J. E., Melosh, H. J., Lisse, C. M., Carcich, B., 2007, A ballistics analysis of the Deep Impact ejecta plume: Determining Comet Tempel 1's gravity, mass, and density, Icarus, 190, 357–390

Sekanina, Z., 1987, Anisotropic emission from comets: Fans versus jets. i. concept and modelling, ESA SP-278, pp. 315–322

Sekanina, Z., Brownlee, D. E., Economou, T. E., Tuzzolino, A. J., Green, S. F., 2004, Modeling the Nucleus and Jets of Comet 81P/Wild 2 Based on the Stardust Encounter Data, Science, 304, 1769–1774

Thomas, N., A'Hearn, M. F., Boice, D. C., Britt, D. T., Meech, K. J., Sandel, B. R., Soderblom, L. A., Yelle, R. V., 2001, Jet morphology in the inner coma of Comet 19P/Borrelly observed by the Deep Space One MICAS imaging system, in Bulletin of the American Astronomical Society, vol. 33 of Bulletin of the American Astronomical Society, p. 1074

Thomas, P. C., Veverka, J., Belton, M. J. S., Hidy, A., A'Hearn, M. F., Farnham, T. L., Groussin, O., Li, J.-Y., McFadden, L. A., Sunshine, J., Wellnitz, D., Lisse, C., Schultz, P., Meech, K. J., Delamere, W. A., 2007, The shape, topography, and geology of Tempel 1 from Deep Impact observations, Icarus, 187, 4–15

Tubiana, C., Barrera, L., Drahus, M., Boehnhardt, H., 2008, Comet 67P/Churyumov-Gerasimenko at a large heliocentric distance, A&A, 490, 377–386

Tuzzolino, A. J., Economou, T. E., Clark, B. C., Tsou, P., Brownlee, D. E., Green, S. F., McDonnell, J. A. M., McBride, N., Colwell, M. T. S. H., 2004, Dust Measurements in the Coma of Comet 81P/Wild 2 by the Dust Flux Monitor Instrument, Science, 304, 1776–1780

Vasundhara, R., 2002, A photometric-dynamic model to simulate coma and jets from a comet. Application to comet Hale-Bopp (C/1995 O1), A&A, 382, 342–358

Vasundhara, R., Chakraborty, P., Muneer, S., Masi, G., Rondi, S., 2007, Investigations of the Morphology of Dust Shells of Comet C/2001 Q4 (NEAT), AJ, 133, 612–621

Vincent, J., Böhnhardt, H., Bertini, I., Lara, L., Küppers, M., Rodrigo, R., 2010a, Coma Structures in Comet 73P/Schwassmann-Wachmann 3, Components B and C, Between January and May 2006, Earth Moon and Planets, 106, 27

Vincent, J., Böhnhardt, H., Lara, L.-M., 2010b, A numerical model of cometary dust coma structures: application to comet 9P/Tempel 1, A&A, 512, A60

Wilson, J. K., Baumgardner, J., Mendillo, M., 1998, Three tails of comet Hale-Bopp, Geophys. Res. Lett., 25, 225–228

Publications related to this work

Papers

- Bertini, I., Lara, L-M., **Vincent, J-B.**, Böhnhardt, H., Küppers, M., Rodrigo, R., Activity evolution, outbursts and splitting events of comet 73P/ Schwassmann-Wachmann 3, Astronomy & Astrophysics, march 2009, volume 496, pp 235-247.

- **Vincent, J-B.**, Böhnhardt H., Bertini, I., Lara, L-M., Küppers, M., Rodrigo, R., Coma structures in comet 73P/Schwassmann-Wachmann 3, components B and C, between January and May 2006, Earth Moon & Planets, October 2009, pp. 66-74.

- **Vincent, J-B.**, Böhnhardt, H., Lara, L-M., A numerical model of cometary dust coma structures: application to comet 9P/Tempel 1, Astronomy & Astrophysics, vol. 512, A60.

- Bagnulo S., Tozzi G.P., Boehnhardt H., **Vincent J-B.**, Muinonen K., Polarimetry and photometry of the peculiar main belt object 7968 133P/Elst-Pizarro, Astronomy & Astrophysics, in Press.

Talks and posters

- **Vincent, J-B.** An introduction to comets, Solar System Seminar, 12/12/07, MPS, Katlenburg-Lindau

- **Vincent, J-B.** Coma structure analysis of comet 73P/ Schwassman-Wachmann 3: dust jets and fragmentation events, 24/04/08 Oberseminar at TU Braunschweig.

- **Vincent, J-B.**; Böhnhardt, H.; Lara, L. M.; Bertini, I. Coma Structures Analysis for Comet Schwassmann-Wachmann 3, Components B and C, Asteroids, Comets, Meteors 2008 .

- **Vincent J-B.**, Böhnhardt H., Lara LM., Bertini I., Imaging and analysis of coma structures for comet Schwassmann-Wachmann 3, fragment C (poster),
Future Ground based Solar System Research: Synergies with Space Probes and Space TelescopeăPortoferraio, Isola d'Elba, Livorno (Italy), September 8-12, 2008.

- **Vincent, J-B.** A numerical model of dust coma structures in active comets, Solar System Seminar, 14/01/09, MPS, Katlenburg-Lindau.

- **Vincent, J-B.**, Böhnhardt, H., Lara, L-M., Constraining the activity of cometary nuclei with a numerical model of dust coma structures EPSC, 2009, Potsdam.

Acknowledgements

So many things have changed for me both personally and professionally since I arrived in Lindau that it is almost impossible to count them all. However I can list those who deserve a big thank you !

First of all Dieter Schmitt and the IMPRS framework for giving me the opportunity to pursue my dream of becoming a scientist.

I would like to thank also my supervisors Hermann Böhnhardt and Jürgen Blum for all their help and support especially at the beginning of my PhD when I had to move to another topic. I definitely recommend both of you as advisors for any other student.

Several persons contributed to this thesis by providing me with good data and interesting discussions. Among them I would like to thank Luisa Lara and Ivano Bertini from el Instituto de Astrofísica de Andalucía. I am sure we will keep collaborating in the future. A special thank you also for Tanyu Bonev and his Bulgarian colleagues for the memorable introduction to the world of ground-based observations in November 2007.

Thanks also to my colleagues and friends at the institute, not only for the useful discussions but also for the nice times we shared apart from the work.

I have a very special acknowledgement for my family and friends who supported me when everybody else wanted me to give up science, and who always respected my choices.

And last but not least, thanks to Nilda for her constant care and support.

Curriculum Vitae

Education

2003	**Licence of Physics**, Université Paul Sabatier (UPS), Toulouse, France
2005	**Master Degree of Astrophysics and Planetology**, UPS, Toulouse, France
2006	**Master Degree of Space Engineering and Instrumentation**, UPS, Toulouse, France
2007-2009	**PhD student**, International Max Planck research school for solar system and beyond, Katlenburg-Lindau, Germany

Scientific Experience

2004	Undergraduate Thesis, CESR, Toulouse, France *Mars atmosphere and surface compositions measurement with gamma spectrometry: study of Mars continuum and influence of solar flares.*
2005	Undergraduate Thesis, CESR, Toulouse, France *X-ray spectrometry of the Moon surface: preparatory study for D-CIXS data processing (SMART-1 mission).*
2006	Undergraduate Thesis, LDTP, Toulouse, France *Application of radar interferometry to the study of a local subsidence.*
2007-2009	PhD Thesis, Max Planck Institut für Sonnensystemforschung, Katlenburg-Lindau, Germany *From observations and measurements to realistic modeling of cometary nuclei.*

Teaching Experience

2002-2005	**Teaching assistant in mathematics and physics** (middle school students), Toulouse, France
2008	**Lecture on comets** (Master students), TU Braunschweig, Germany
	Introduction to remote sensing in planetology (Master students), TU Braunschweig, Germany
2009	**Lecture on comets** (Master students), TU Braunschweig, Germany

Additional information

Date of birth	May, 30th, 1983
Languages	French (native), English (fluent), Spanish (High-school Level), basic notions of German and Italian
Computer skills	Daily usage of Windows and Unix, large experience in programming (Matlab, MIDAS, IDL, C/C++, Visual Basic, Java, HTML, PHP/MySQL, Javascript), and with various software (Latex, Word, Excel, Powerpoint, Gimp).
Hobbies	Programming, music, origami, reading, sport.